ANL-77-62

Lb. 1644

ANL-77-62

276
12-7-77

MATERIALS TECHNOLOGY FOR COAL-CONVERSION PROCESSES

Eleventh Quarterly Report, April–June 1977

ARGONNE NATIONAL LABORATORY, ARGONNE, ILLINOIS

Prepared for the U. S. ENERGY RESEARCH AND DEVELOPMENT ADMINISTRATION under Contract W-31-109-Eng-38

Distribution Category:
Coal Conversion and Utilization--
Coal Gasification (UC-90c)

ANL-77-62

ARGONNE NATIONAL LABORATORY
9700 South Cass Avenue
Argonne, Illinois 60439

MATERIALS TECHNOLOGY FOR COAL-CONVERSION PROCESSES

Eleventh Quarterly Report,
April—June 1977

W. A. Ellingson
Project Leader

Materials Science Division

Previous reports in this series

ANL-76-7	July—September 1975
ANL-76-22	October—December 1975
ANL-76-60	January—March 1976
ANL-76-111	April—June 1976
ANL-76-125	July—September 1976
ANL-77-5	October—December 1976
ANL-77-41	January—March 1977

TABLE OF CONTENTS

	Page
HIGHLIGHTS	ix
ABSTRACT	1
INTRODUCTION	1
Task A -- Evaluation of Ceramic Refractories for Slagging Gasifiers	1
Task B -- Evaluation of Ceramic Coatings for Coal-conversion Plants	20
Task C -- Application and Development of Nondestructive Evaluation Methods for Coal-conversion Processes	22
1. Erosive-wear Detection and Monitoring	22
a. Metallic Transfer Lines	22
(1) Field Studies	22
b. Refractory-lined Transfer Lines	23
(1) Infrared	23
2. Refractory-installation Practices	24
a. Acoustic Emission	24
3. Component Inspection	25
a. Acoustic Monitoring of Valves	25
Task D -- Corrosion Behavior of Materials in Coal-conversion Processes	46
1. Uniaxial Tensile Properties	46
2. Thermodynamics of Multicomponent Gas Mixtures	47
3. Chemical Potentials of Carbon and Oxygen	47
4. Chemical Potential of Sulfur	48
5. Effect of Variation in Gas Composition	49
6. Effect of Pressure	49
7. Effect of N_2 Additions	50
Task E -- Erosion Behavior of Materials in Coal-conversion Processes	64

TABLE OF CONTENTS (Contd.)

	Page
Task F -- Component Performance and Failure Analysis	70
1. Ballooned Pipe from the Synthane Pilot Plant	70
2. Synthane Impeller-shaft Failure	70
3. Battelle Char-Burner Thermowells	71
4. Pit Formation on the Synthane Thermowells	72
5. BB-1 Purge Piping from the Synthane Gasifier	72
6. Synthane Gasifier Nozzle Failures	72
REFERENCES	79

LIST OF FIGURES

No.	Title	Page
1	Furnace Plenum Temperature and Brick Temperatures 12.7 mm (0.5 in.) from the Hot Face of Each Composition during Test Run 4	9
2	Temperatures in Bricks during Test Run 4 at Four Locations in Full-length Bricks and at Three Locations in 3/4- and 1/2-length Bricks	10
3	Posttest Photographs of the 3/4-length Bricks Subjected to Slag Attack in Run 4	11
4	Maximum Depth of Removal as a Function of Brick Length for Silicon-oxynitride Refractory Bricks Exposed in Run 4	12
5	Polished Section of Oxynitride-bonded SiC Brick (Number 37) Exposed to Coal Slag	12
6	Higher Magnification View of Fig. 5 Showing Slag Penetration along Bond Phase of Oxynitride-bonded SiC Brick (Number 37)	13
7	Polished Section of the Silicate-bonded SiC Brick (Number 93) -- Coal-slag Interface	13
8	Scanning-electron Micrograph Showing Slag Remaining on Surface of Silicate-bonded SiC Brick (Number 93)	14
9	Polished Section of Nitride-bonded SiC Brick (Number 91) Exposed to Coal Slag Showing the Degree of Slag Penetration	14
10	Polished Section of Silicon-oxynitride Brick (Number 36) Exposed to Coal Slag Showing Refractory on the Right and Slag with Entrained Metallic Particles on the Left	15
11	Scanning-electron Micrograph Showing the Interactions between Slag (Left) and Silicon-oxynitride Brick (Number 36)	16
12	Furnace Plenum Temperature and Temperature 38.1 mm (1.5 in.) from the Hot Face of Magnesia-chromia 3/4-length Refractory Bricks during Run 5	17
13	Temperatures in Magnesia-chromia Bricks during Test Run 5 at Four Locations in Full-length Bricks and at Three Locations in 3/4- and 1/2-length Bricks	18
14	Schematic of Bi-Gas Erosive-wear Detection Locations on Blocked Tee and Initial Erosive-wear Pattern Detected after 200-h of Exposure	30

LIST OF FIGURES (Contd.)

No.	Title	Page
15	Erosive Wear of Stellite 6B Hard Facing on HYGAS Cyclone Separator as Measured by Ultrasonic Techniques	30
16	A Three-dimensional Model in Cylindrical Coordinates	31
17	A Sample Presentation of Cavity Configuration and Temperature Data	32
18	Effect of Cavity Depth on Temperature Data	33
19	Effect of Cavity Width on Temperature Data	34
20	Feature Curves for Gases Given in Fig. 18	35
21	Feature Curves for Gases Given in Fig. 19	36
22	Characteristic Acoustic Emission Obtained from Monolithic, Isothermally Heated, Refractory Specimens of 95% Alumina with Controlled Cooling	37
23	Characteristic Acoustic Emission Obtained from Monolithic, Isothermally Heated, Refractory Specimens of 95% Alumina with Exponential (Furnace) Cooling	37
24	Characteristic Acoustic Emission Obtained from Monolithic, Isothermally Heated Refractory Specimens of 60% Alumina with Controlled Cooling	38
25	Characteristic Acoustic Emission Obtained from Monolithic, Isothermally Heated Refractory Specimens of 60% Alumina with Exponential (Furnace) Cooling	38
26	Detected Acoustic Activity for Various Refractory Densities when Fractured under Load	39
27	Jamesbury 4-in. Ball Test Valve as Installed in MERC Static Valve Facility	39
28	Transducer Locations for Acoustic Monitoring	40
29	Tensile Specimens of Different Alloys before Testing (a) and after Testing at 750°C (b), 871°C (c), and 982°C (d)	54
30	True Stress-True Strain Curves for Incoloy 800 in the As-received Condition at 750, 871, and 982°C	55
31	True Stress-True Strain Curves for Type 310 Stainless Steel in the As-received Condition at 750, 871, and 982°C	55

LIST OF FIGURES (Contd.)

No.	Title	Page
32	True Stress-True Strain Curves for U. S. Steel Alloy 18-18-2 in the As-received Condition at 750, 871, and 982°C	56
33	True Stress-True Strain Curves for Inconel 671 in the As-received Condition at 750, 871, and 982°C	56
34	The Variation in Chemical Potentials of (a) Carbon and (b) Oxygen at 1148 K and 1-atm Total Pressure as a Function of the Volume Ratio of CH_4/H_2 for Different CO/CO_2 Ratios and Volume Fractions of H_2O in the Room-temperature Gas Composition	57
35	The Variation in Chemical Potentials of (a) Carbon and (b) Oxygen at 1148 K and 1-atm Total Pressure as a Function of the Atomic Ratio C/H for Different C/O Ratios in the Room-temperature Gas Composition	58
36	Plots of the Isopotential Lines for a_c and p_{O_2} as a Function of C/H and C/O Ratios at 1148 K	59
37	Plots of the Isopotential Lines for p_{S_2} as a Function of C/H, C/S, and C/O Ratios at 1148 K	59
38	Isopotential Diagrams at 1273 K Showing the Effect of Variations in the Contents of Different Constituents of the Gas Mixture on the Chemical Potentials of C, O, and S	60
39	The Variation in a_c with Total Pressure P at 1148 K	61
40	The Variation in p_{O_2} with Total Pressure P at 1148 K	61
41	The Variation in p_{S_2} with Total Pressure P	62
42	Erosion-Corrosion Test Chamber for Coal-gas Environment	68
43	Schematic of the Pump Shaft and Capscrew for the Venturi Scrubber Recycle Water Pump GA-207 from the Synthane Plant	74
44	Cross Section of Synthane Pump Impeller Shaft Showing the Keyway Fillet Radius, Crack, and Fractured Capscrew	75
45	Battelle Char-Burner Thermocouple Protection Tubes Showing Corrosion Scale and Fracture	75
46	Pits at the OD of the Synthane Thermowell	76
47	Schematic of Three Sections of BB-1 Purge Piping from the Synthane Gasifier, with Exposure Times Indicated	77
48	Optical Macrograph of Pits at the OD of the BB-1 Purge Line from the Synthane Gasifier	77

LIST OF TABLES

No.	Title	Page
I	Composition of Slag (wt %) during Corrosion Test Run 4	5
II	Relative Corrosion Resistance of Refractories Exposed to Slag Attack in Run 4	6
III	Composition of Slag (wt %) during Corrosion Test Run 5	7
IV	Relative Resistance of Refractories Exposed to Slag Attack in Run 5 (Preliminary Results)	8
V	Test Conditions	27
VI	Rms Acoustic Emission (V) and Leakage Rate (175 kHz Resonant Transducer)	28
VII	Rms Acoustic Emission (V) and Leakage Rate (375 kHz Resonant Transducer)	29
VIII	Rms Acoustic Emission (V) and Leakage Rate (750 kHz Resonant Transducer)	29
IX	Tensile Properties of Four Selected Alloys in the As-received Condition	52
X	Compositions (Vol %) of the Gas Mixtures Shown in Fig. 38 . .	53
XI	Test Matrix	66
XII	Projected Schedule for Test Program	67

MATERIALS TECHNOLOGY FOR COAL-CONVERSION PROCESSES: ELEVENTH QUARTERLY REPORT, APRIL-JUNE 1977

HIGHLIGHTS

Task A -- Evaluation of Ceramic Refractories for Slagging Gasifiers *(C. R. Kennedy, T. D. Claar, R. J. Fousek, D. J. Jones, and R. B. Poeppel)*

Silicon-carbide refractories with various bond systems exposed to molten slag at 1500°C for 500 h in Run 4 showed virtually no attack. The resistance of the silicon carbide to slag attack is attributed to large thermal fluxes induced by water-cooled chills applied to the cold faces.

Magnesia-chromia refractories exposed to molten slag at 1500°C for 500 h in Run 5 were somewhat less resistant to slag attack than the silicon-carbide refractories.

Task B -- Evaluation of Ceramic Coatings for Coal-conversion Plants *(S. Danyluk, R. B. Poeppel, and G. M. Dragel)*

Metallic specimens with total or partial coatings have been shipped to Argonne National Laboratory by Solar.

Task C -- Application and Development of Nondestructive Evaluation Methods for Coal-conversion Processes *(W. A. Ellingson, W. J. Shack, C. L. Johnson, and C. K. Hsieh)*

In-situ erosive-wear measurements on the Bi-Gas A106B low-carbon steel main coal feed line were obtained during the present quarter, with initial indications of a nominal 5% wall-thickness reduction after approximately 200 h of exposure. The high-temperature acoustic-waveguide detection system is performing well after almost 12 months of service. Seven refractory tests were conducted in the present quarter using different heat-up and cool-down schedules on high- and low-alumina refractories to study characteristic acoustic-emission signatures during heating and cooling. Initial results show that high-alumina refractories from two commercial producers yield similar acoustic signatures. Low-alumina refractory materials yield lower total counts and lower count rates. A three-dimensional heat-transfer model for single-component refractory linings has been completed, and initial theoretical outside-shell temperature distributions have been calculated for various synthesized rectangular cavities. Acoustic leak-detection tests were carried out on the Morgantown Energy Research Center Valve Test Facility (MERC-VTF). The valve tested was a commercially produced 100-mm (4-in.) ball valve; the differential pressure used during the test was 623 Pa (130 psig). Three resonant transducers were used, and again the 750-kHz transducer was able to detect leaks far lower than those considered acceptable; 19-m^3/s/mm (1-cfm/in.) diameter. Initial field results also indicate that, for a known leak, some correlation exists between acoustic output and differential pressure.

Task D -- Corrosion Behavior of Materials in Coal-conversion Processes *(K. Natesan and O. K. Chopra)*

Uniaxial tensile data were generated on Incoloy 800, Type 310 stainless steel, U. S. Steel Alloy 18-18-2, and Inconel 671 in an as-received condition at temperatures of 750, 871, and 982°C. Test temperature had a negligible effect on the fracture strain of Incoloy 800 and U. S. Steel Alloy 18-18-2; however, the true strain for Type 310 stainless steel and Inconel 671 increased as the test temperature increased from 750 to 982°C. The load-elongation data also showed that the uniform strain for different alloys was considerably less than the total elongation at failure, i.e., 2 to 10% versus 32 to 234%.

A generalized approach, based on thermodynamic equilibria of gas mixtures, has been developed to evaluate the chemical potentials of the reactive elements, i.e., O, S, C, H, and N in multicomponent gas streams. The analysis has been used to examine the effect of temperature, total pressure, gas composition, and nitrogen dilution on the chemical potentials of the reactive elements. The results showed that the chemical potentials can be uniquely established by the total atomic ratios C/H, C/O, and C/S in the initial gas mixture.

Task E -- Erosion Behavior of Materials in Coal-conversion Processes *(W. J. Shack and J. Y. Park)*

A work plan for the experimental phase of the program has been developed. It will include initial short-term testing to characterize the erosive behavior of various candidate materials for coal-conversion plants and also longer-term tests to characterize combined erosion/corrosion.

Task F -- Component Performance and Failure Analysis *(S. Danyluk and G. M. Dragel)*

Failed components from the Synthane Plant (ballooned pipe, pump impeller shaft (GA-207), thermowell, purge piping (BB-1), and the Battelle Char-Burner (Thermowells) were examined. In addition, a field trip was made to Synthane to consult with plant personnel on cracks discovered in the nozzles from the gasifier vessel.

MATERIALS TECHNOLOGY FOR COAL-CONVERSION PROCESSES: ELEVENTH QUARTERLY REPORT, APRIL-JUNE 1977

ABSTRACT

This broad-base materials engineering program, begun in 1974, includes studies on ceramic (refractory) and metallic materials presently being used or intended for use in coal-conversion processes. The program entails studies of erosive wear, nondestructive testing, corrosion, chemical degradation, and failure analysis. Appropriate laboratory and field experiments are integrated such that the results have impact on present pilot-plant and proposed demonstration-plant designs. This quarterly report, for the period April-June 1977, presents the technical accomplishments of the program.

INTRODUCTION

The economical conversion of coal into clean and usable fuels will be advanced through the use of durable materials systems. The technical information base required for materials selection in plant design for the operating environments of various coal-conversion processes is extremely limited. Hence, reliable selection and life-time prediction methods of materials under these conditions are not available. This project is designed to provide part of the materials information necessary for successful operation of coal-conversion systems. The present report is the eleventh quarterly progress report submitted by ANL to the Division of Materials and Exploratory Research*/ERDA Fossil Energy under project Number 7106, "Materials Technology for Coal Conversion Processes."

The project includes six tasks: (A) evaluation of commercial refractories exposed to coal slag under conditions typical of those encountered in slagging gasification processes; (B) evaluation of erosion/corrosion-resistant coatings when exposed to prototypic operating environments; (C) development, evaluation, and application of nondestructive evaluation methods applicable to coal-conversion systems; (D) evaluation of the corrosion behavior of commercial alloys; (E) development of analytical models to predict the erosive-wear behavior of materials used in coal-conversion plants; and (F) analysis of failed coal-conversion plant components.

Task A -- Evaluation of Ceramic Refractories for Slagging Gasifiers

C. R. Kennedy, T. D. Claar, R. J. Fousek, D. J. Jones, and R. B. Poeppel)

The purpose of task A is to evaluate the resistance of various refractory bricks to attack by molten coal slag. Three tests in the

*Formerly Division of Advanced Research and Supporting Technology.

slag-corrosion rig have been conducted with atypical temperature gradient conditions within the bricks, the results of which have been reported previously.[1-5] A new furnace bottom for the rig has been built[6] that will produce prototypic gradients by means of water-cooled chills. During the present quarter, the fourth[6] and fifth 500-h tests and posttest analysis of the bricks from the fourth test were completed.

The fourth test included silicon oxynitride (number 36) and silicon carbide with three bond systems: nitride bonded (number 91), silicate bonded (number 93), and oxynitride bonded (number 37). Standard 9-in. bricks were cut to three lengths (full length, 3/4 length, and 1/2 length) so that three temperature gradients could be studied. Each chill cooled three bricks of one length and composition.

The slag composition utilized was a simulated Montana Rosebud (Table I). Slag was introduced three times during the test (at 0, 50, and 160 h). The initially high iron-oxide content resulted from a batching error that was rectified at 160 h. The ferritic content at 500 h was ∿15%, which indicated a reducing atmosphere. Posttest examination of the slag bath revealed two layers that were quite different in appearance. A dark greenish-black glassy slag, with a composition essentially identical to that of the sample taken from the hot furnace just prior to shutdown, rested upon a grayish slag with a crystalline, rocky-like appearance. Posttest chemical analysis of the frozen slag showed that the rocky slag was somewhat lower in SiO_2 and somewhat higher in Fe_2O_3 than the glassy slag. Indications from probing during slag sampling are that the rocky slag crystallized slowly during the test and, therefore, did not contribute to the attack of the brick.

The furnace plenum temperature and the temperatures in the 3/4-length bricks at a location 12.7 mm (0.5 in.) from the hot faces are shown in Fig. 1. The slag-refractory interface was ∿1450°C, as determined with an optical pyrometer. The thermal profile that existed within the bricks after the slag was added on April 21 is shown in Fig. 2. Oxygen partial pressure was maintained at $\sim 10^{-3}$ Pa.

The bricks were removed from the furnace after 500 h. They were sectioned lengthwise in the vertical plane so that slag attack (material removal and slag penetration) could be viewed in cross section. The vertical sections cut from the 3/4-length bricks of each type are shown (right side up) in Fig. 3. The vertical face of each brick opposite the ruler was exposed to slag. Three lines of attack are visible that correspond to the three levels of slag during the test. Although these three lines are apparent on all bricks, in the photographs they are most evident on the silicon oxynitride, the material that was attacked the most.

The relative resistance of the four refractory compositions to slag attack is summarized in Table II. The first attack line (designated bottom in Table II) corresponds to an ∿50-h exposure to slag with a B/A ratio of 1.0. The second attack line corresponds to an ∿110-h exposure to slag of similar composition. The third attack line resulted from a 340-h exposure to slag with a B/A ratio of ∿0.6. Since the vertical temperature gradient in the slag is large, little attack below the slag line occurs. For each position, the maximum depth to which the refractory was actually removed is indicated in the table.

All of the SiC bricks exhibited little attack, contrary to the results obtained in previous experiments in which water cooling was not employed.[4] The capability of the SiC to resist attack may be attributed to the high thermal flux within the bricks. Typical values of heat flux for the silicon-carbide bricks with chills were 40-50 kW/m^2 for full-length bricks; 50-70 kW/m^2 for 3/4-length bricks; and 60-90 kW/m^2 for 1/2-length bricks. The heat flux was obtained by multiplying the measured thermal gradient by the published value of thermal conductivity.

Only slight differences in resistance to slag attack among the three types of SiC bricks were detected. The oxynitride bonded (number 37) SiC was somewhat less resistant; the silicon-oxynitride (number 36) brick was much less resistant, with the maximum depth of removal an order of magnitude higher than in any of the carbide bricks. The effect of the length of the brick on the depth of removal is shown in Fig. 4, and, as can be seen, even the 1/2-size silicon-oxynitride brick exhibited substantial attack.

Metallographic sections were taken from each of the 3/4-length bricks near the refractory-slag line interface. After polishing through 1-μ diamond paste, they were examined by optical and scanning-electron microscopy to determine the nature and extent of slag-refractory interactions.

The microstructures of the three SiC refractories exhibited similar features. A layer of glassy slag or slag-refractory chemical reaction product remained on some refractory surfaces after removal from the corrosion-testing apparatus. In general, the glassy layer was in intimate contact with the refractory surface, contained large pores, and had a dendritic solidification structure. Only slight penetration of slag along the bond phase of the SiC bricks was observed. Penetration depths were ∿0.2 to 0.3 mm. These features of the slag interaction are evident in the optical and SEM micrographs of Figs. 5-9.

As expected from a comparison of material-loss measurements, slag interaction with the silicon-oxynitride (number 36) refractory was significantly different from that observed in the SiC refractories. Slag was observed to have penetrated into the silicon-oxynitride brick to a depth of ∿25 mm as a result of the porosity present in the as-received material. Figure 10 is an optical photomicrograph showing slag penetration into and reaction with the silicon-oxynitride refractory. The gray phase on the left side of the micrograph is the bulk slag that solidified on the brick surface. The white metallic particles present in the slag phase were examined by energy-dispersive x-ray analysis and only iron was detected. Iron particles, similar in appearance to the smaller ones distributed in the slag-refractory interface layer, were observed in an unexposed section of the brick. As the refractory matrix was attacked by the slag, the metallic particles became entrained in the rather stagnant layer near the surface of the brick where they appeared to have coalesced.

The reaction between the slag and the silicon-oxynitride refractory was apparent in the SEM (Fig. 11). The large bubbles and light metal particles are evident in the slag phase on the left. The refractory on the

right exhibited a significant degree of porosity through which the slag has penetrated. A large island of slag can be seen in the lower right corner. Slag could be easily distinguished from the refractory matrix by means of the calcium x-ray peak, which was observed only in the slag spectrum.

The fifth run included four magnesia-chromia-spinel bricks. The furnace temperatures and temperatures in the 3/4-length bricks at a location 38.1 mm from the hot face are shown in Fig. 12. Shown for comparison are the temperatures within a 3/4-length SiC brick (number 93) from Run 4 also at a location 38.1 mm from the hot face. Typical thermal profiles within the bricks are shown in Fig. 13. Since the thermal conductivity of SiC refractories is almost an order of magnitude higher than that of the magnesia-chromia refractories, some differences in the thermal profiles were observed (compare Fig. 13 with Fig. 2). Typical heat fluxes in the magnesia-chromia bricks were 8 kW/m^2 for full-length bricks, 11 kW/m^2 for 3/4-length bricks, and 13 kW/ft for 1/2-length bricks. These values are 1/5 to 1/7 the heat flux in the silicon carbide bricks.

The composition of the slag during corrosion test Run 5 is summarized in Table III. The B/A ratio was $\sim$0.7 and the ferritic content was negligible. The weight percent of Fe_2O_3 is obtained by subtracting the weight percent of Fe^{++} from the total Fe content. A dash (-) in the table indicates the difference was less than the reported uncertainty (0.2 wt %). The partial pressure of oxygen was $\sim 10^{-3}$ to 10^{-4} Pa. Two charges of synthetic slag were made. A glassy-rocky slag separation similar to that which occurred in Run 4 was observed during posttest examination. Two slag attack lines, corresponding to the two slag bath levels but not to the slag separation level, were noted.

Preliminary measurements of slag attack were made on uncut brick specimens, and the results are reported in Table IV. Little difference between the magnesia-chromia bricks in resistance to slag attack is evident from these rough values. The bottom line of attack occurred during $\sim$70 h of exposure to the slag, whereas the top line of attack was the result of $\sim$430 h of exposure. In comparison with the SiC refractories tested in Run 4, the magnesia-chromia refractories exhibited somewhat inferior slag resistance. Macroscopic and metallographic examination of the attacked regions in the magnesia-chromia bricks is in progress. The results of this examination as well as more accurate measurements of the depth of removals (from cut section) will be reported in the next quarterly.

The slag-corrosion furnace has been relined with new refractories, and the sixth test is scheduled to begin in the first week of August. Bricks to be tested are fused-cast alumina (number 2), fused-cast magnesia-chromia (number 40), direct bonded magnesia-chromia (number 41), and fused-cast alumina-chromia (number 42).

TABLE I. Composition of Slag (wt %) during Corrosion Test Run 4

Components	Exposure Time, h				
	3	184	500	Glassy Slag	Rocky Slag
SiO_2 (S)	35	41	41.6	42	35
Al_2O_3 (A)	14	20	21	21.1	20.9
Fe_2O_3 (F)	4.7	0.4	1.3	1.4	6.5
FeO (F)	16	5.9	6.4	6.9	8.6
CaO (C)	21.1	24.2	22	20.2	21
MgO (M)	6.2	4.5	5.5	6.2	5.2
Na_2O (N)	1.2	1.8	0.6	0.6	1.2
K_2O (K)	1.1	1.1	0.6	0.6	0.7
TiO_2 (T)	0.7	1.1	1.0	1.0	0.9
B/A Ratio[a]	1.0	0.62	0.59	0.57	0.78
Ferritic Content,[b] %	21	6	15	15	40

[a]Base-to-acid ratio $B/A = (F + C + M + N + K)/(S + A + T)$.

[b]$$\text{Ferritic content} = \frac{\text{wt \% } (Fe_2O_3)}{\text{wt \% } (Fe_2O_3) + 1.11 \text{ wt \% } (FeO) + 1.43 \text{ wt \% } (Fe)}$$

TABLE II. Relative Corrosion Resistance of Refractories Exposed to Slag Attack in Run 4

Composition	Bond	Number	Attack Line	Maximum Depth of Removal, mm		
				Full Length	3/4 Length	1/2 Length
SiC	Oxynitride	37	Top	2-3	3	2
			Middle	2-3	2-3	3
			Bottom	3-4	1-3	3
SiC	Silicate	93	Top	2-5	4	1-2
			Middle	4-7	1	1-2
			Bottom	3-4	1-2	0
SiC	Nitride	91	Top	4-5	1	1-2
			Middle	1-2	1	1
			Bottom	2-3	0	1
Si_2ON_2(70)-Si_3N_4(20)-SiC(10)	Oxynitride	36	Top	47-52	32-34	18-25
			Middle	32	28-29	15-18
			Bottom	32-33	25-27	14

TABLE III. Composition of Slag (wt %) during Corrosion Test Run 5

Component	Exposure Time, h				
	68	163 (Near Brick Face)	163 (Near Center)	331	499
SiO_2 (S)	38	39.4	39.1	40.5	40.7
Al_2O_3 (A)	22	19	18.6	20.4	20.1
Fe_2O_3 (F)	0.4	-	-	-	-
FeO (F/1.11)	6.2	6.9	7.0	6.4	6.4
CaO (C)	22	24	25	24	24.9
MgO (M)	7.6	6.6	6.2	5.8	5.9
Na_2O (N)	1.6	1.7	1.8	1.2	0.7
K_2O (K)	0.7	1.0	1.1	0.7	0.3
TiO_2 (T)	0.9	0.9	1.0	0.8	0.9
Cr_2O_3	0.6	0.5	0.2	0.2	0.1
B/A Ratio[a]	0.6	0.7	0.7	0.6	0.6
Ferritic Content,[b] %	<1	-	-	-	-

[a]Base-to-acid ratio B/A = (F + C + M + N + K)/(S + A + T).

[b]Ferritic content = $\frac{\text{wt \% } (Fe_2O_3)}{\text{wt \% } (Fe_2O_3) + 1.11 \text{ wt \% } (FeO) + 1.43 \text{ wt \% } (Fe)}$.

TABLE IV. Relative Resistance of Refractories Exposed to Slag Attack in Run 5 (Preliminary Results)

Compositions	Number	Attack Line	Maximum Depth of Removal, mm		
			Full Length	3/4 Length	1/2 Length
$MgO(53)-Cr_2O_3(20)-Al_2O_3(17)-Fe_2O_3(8)-SiO_2(2)-CaO(1)$	19	Top	6	8	7
		Bottom	8	10	6
$MgO(59)-Cr_2O_3(19)-Al_2O_3(13)-Fe_2O_3(7)-SiO_2(1.5)-CaO(0.5)$	20	Top	8	6	9
		Middle	7	4	5
$MgO(63)-Cr_2O_3(18)-Al_2O_3(5)-Fe_2O_3(12)-SiO_2(1)-CaO(1)$	29	Top	8	6	4
		Middle	6	1	2
$MgO(60)-Cr_2O_3(15.5)-Al_2O_3(15)-Fe_2O_3(7)-SiO_2(1.5)-CaO(1)$	35	Top	6	7	5
		Middle	4	4	4

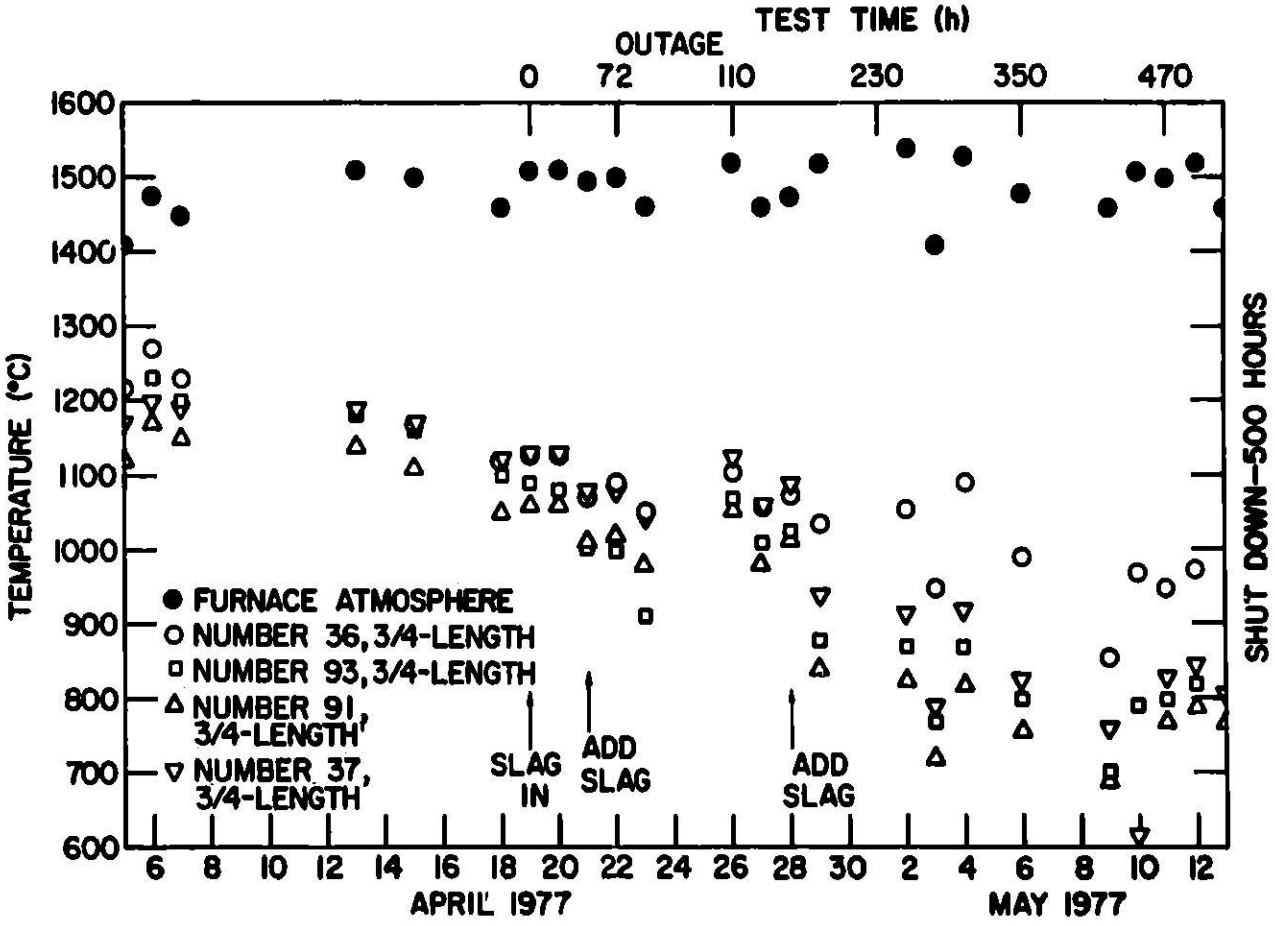

Fig. 1. Furnace Plenum Temperature and Brick Temperatures 12.7 mm (0.5 in.) from the Hot Face of Each Composition during Test Run 4. ANL Neg. No. 306-77-382.

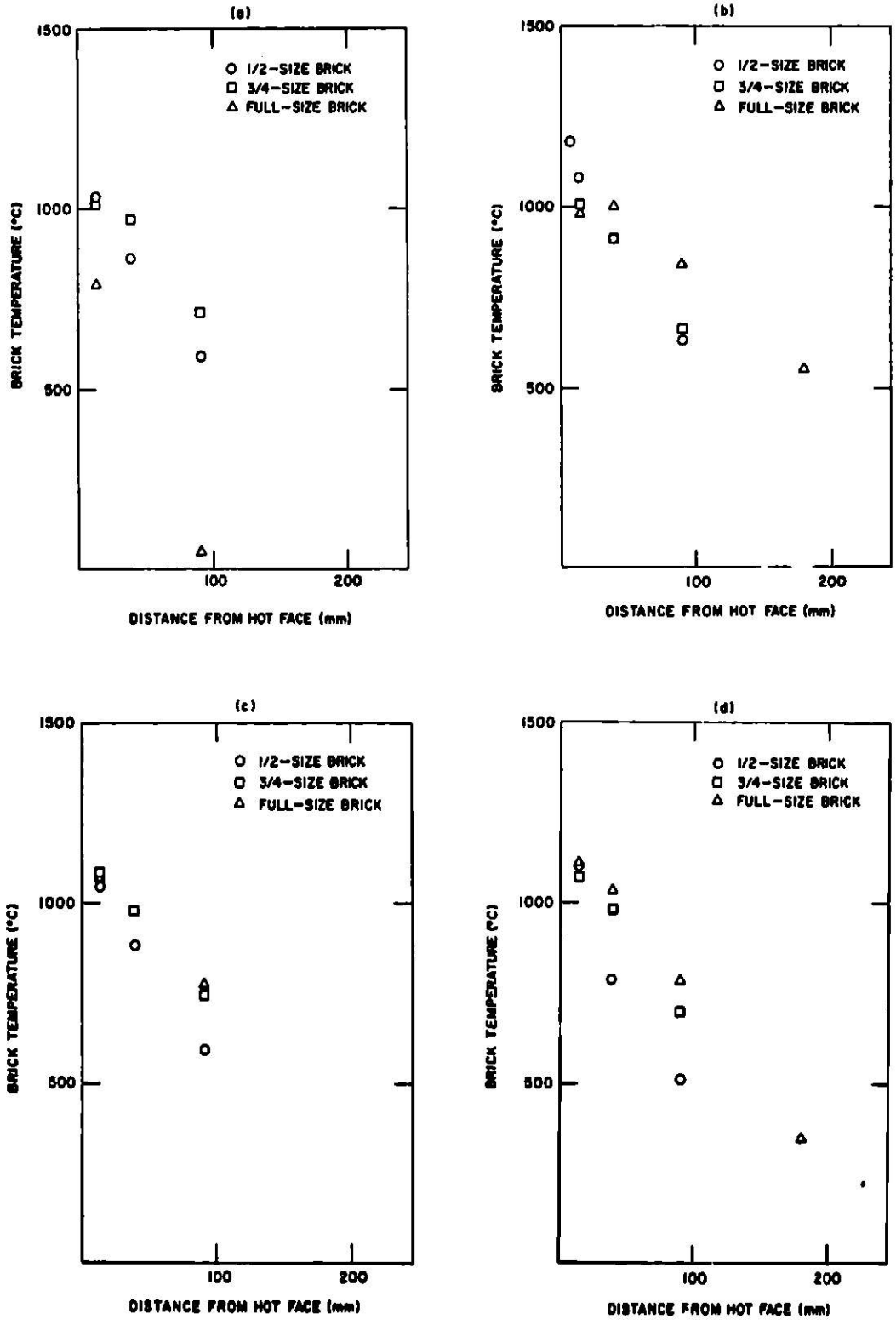

Fig. 2. Temperatures in Bricks during Test Run 4 at Four Locations in Full-length Bricks and at Three Locations in 3/4- and 1/2-length Bricks. (Lack of data points indicates thermocouple failed.) (a) Nitride-bonded silicon carbide, (b) silicate-bonded silicon carbide, (c) oxynitride-bonded silicon carbide, and (d) silicon oxynitride. ANL Neg. No. 306-77-386.

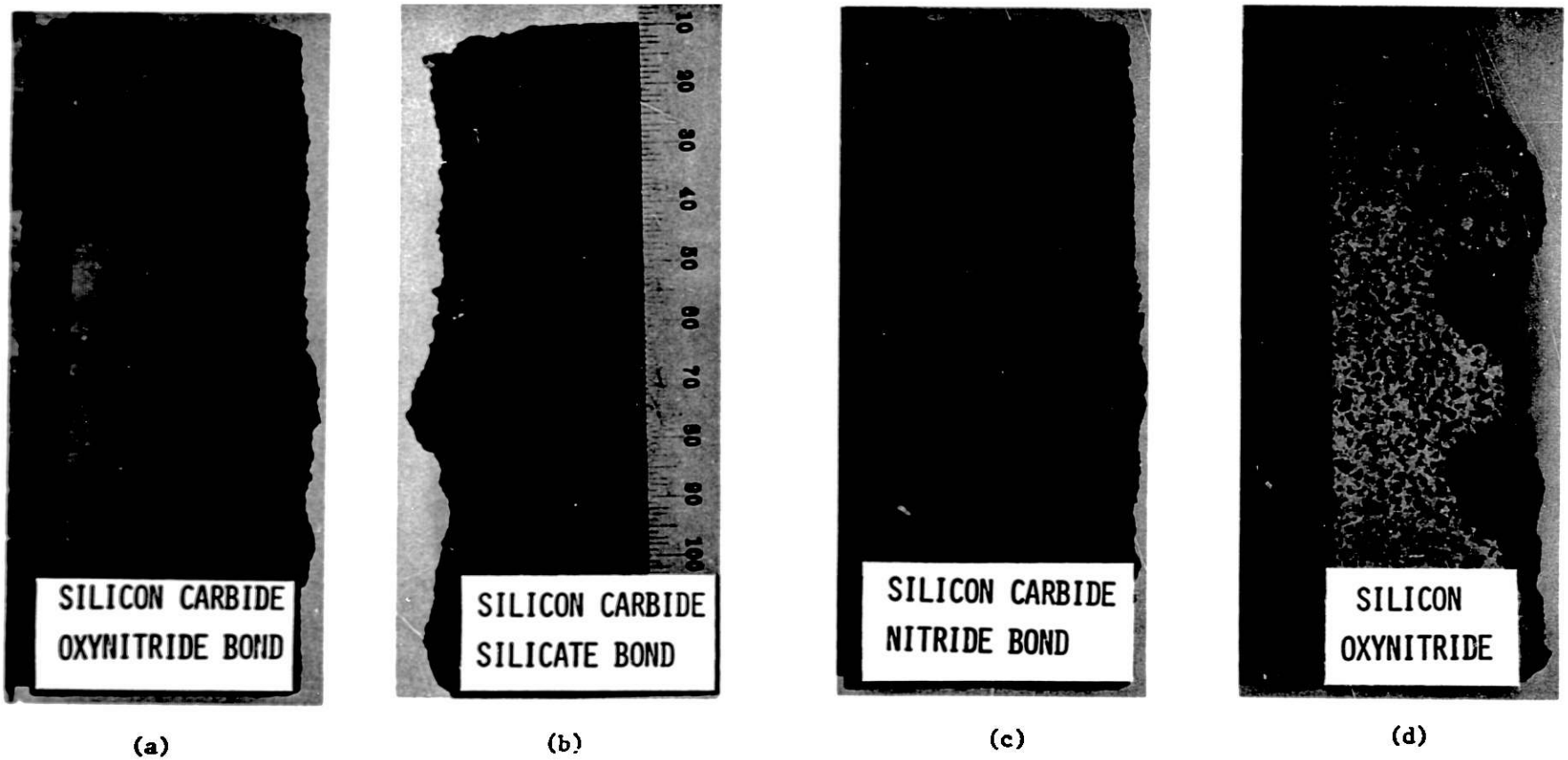

Fig. 3. Posttest Photographs of the 3/4-length Bricks Subjected to Slag Attack in Run 4. The vertical faces opposite the ruler were exposed to the slag. (a) Oxynitride-bonded SiC (number 37), (b) silicate-bonded SiC (number 93), (c) nitride-bonded SiC (number 91), and (d) silicon-oxynitride (number 36). Note the three levels of slag attack. ANL Neg. No. 306-77-387.

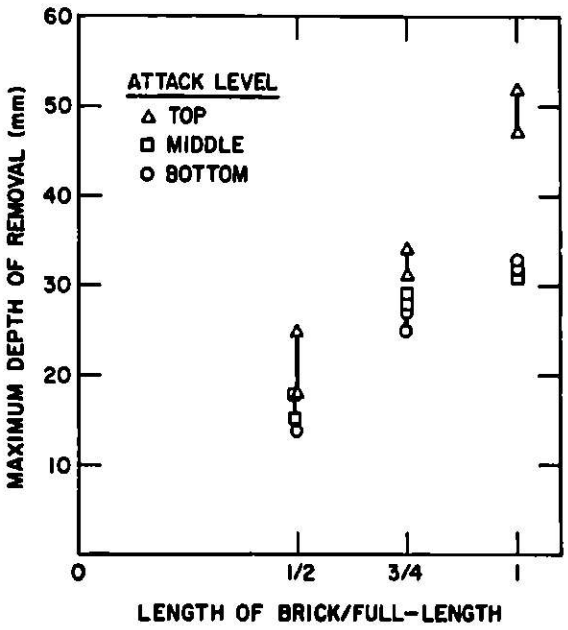

Fig. 4. Maximum Depth of Removal as a Function of Brick Length for Silicon-oxynitride Refractory Bricks Exposed in Run 4. ANL Neg. No. 306-77-372.

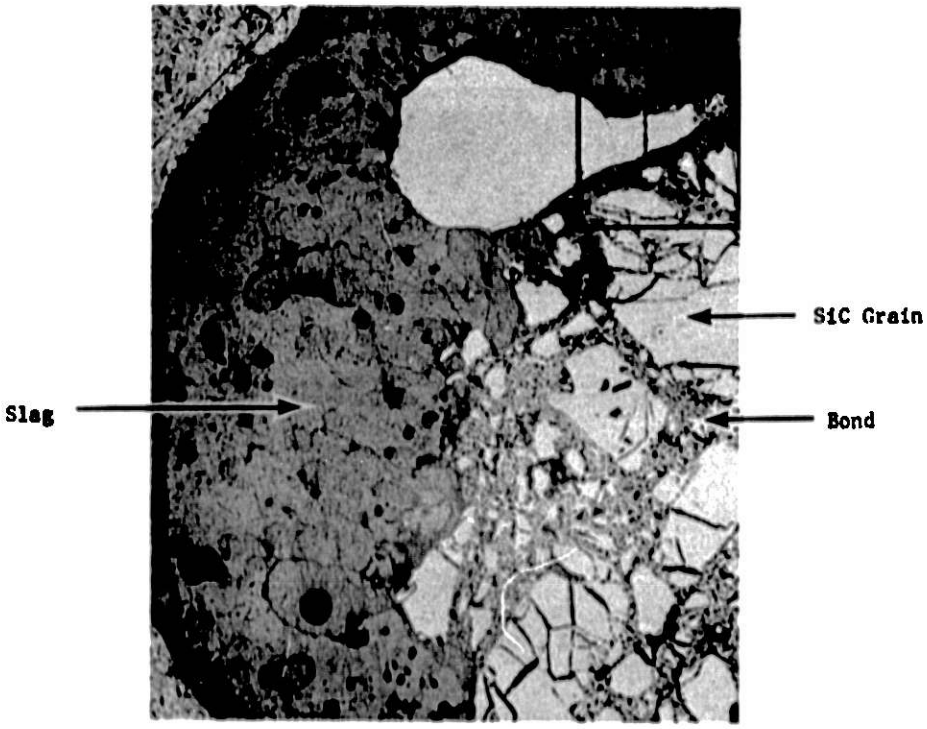

Fig. 5. Polished Section of Oxynitride-bonded SiC Brick (Number 37) Exposed to Coal Slag. Gray phase at left is adherent slag. The area in the box is shown at higher magnification in Fig. 6. (Taken with reflected light.) ANL Neg. No. 306-77-391.

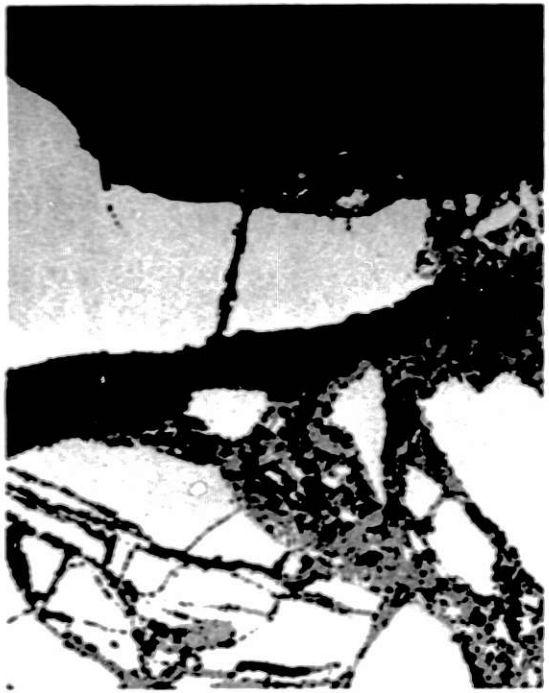

Fig. 6. Higher Magnification View of Fig. 5 Showing Slag Penetration along Bond Phase of Oxynitride-bonded SiC Brick (Number 37). (Taken with reflected light.) Magnification 100X. ANL Neg. No. 306-77-394.

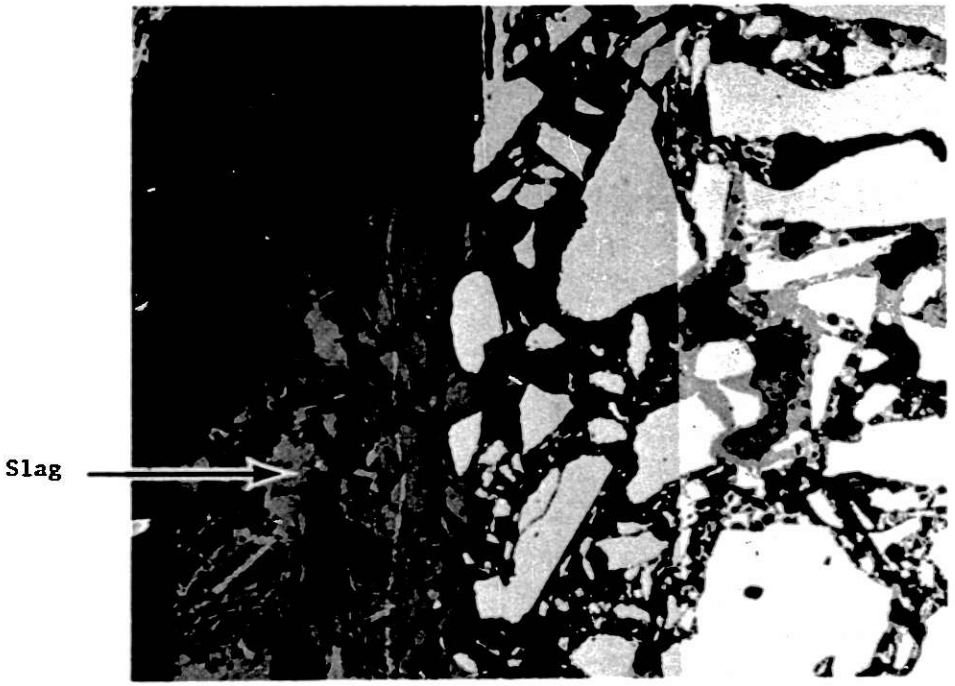

Fig. 7. Polished Section of the Silicate-bonded SiC Brick (Number 93) -- Coal-slag Interface. (Taken with reflected light.) Magnification 100X. ANL Neg. No. 306-77-390.

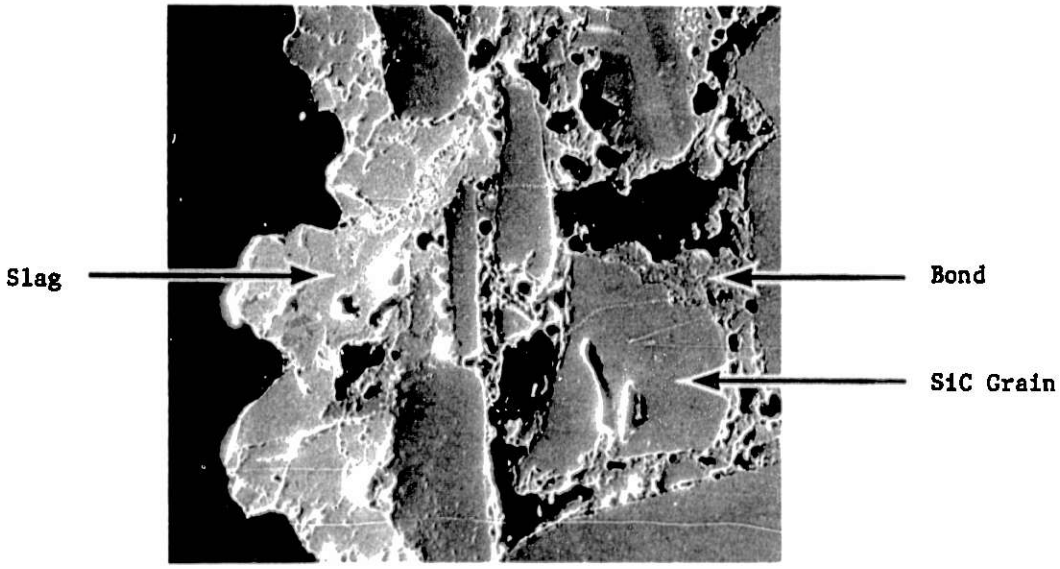

Fig. 8. Scanning-electron Micrograph Showing Slag Remaining on Surface of Silicate-bonded SiC Brick (Number 93). Only slight penetration of slag along the bond is apparent. Magnification 150X. ANL Neg. No. 306-77-392.

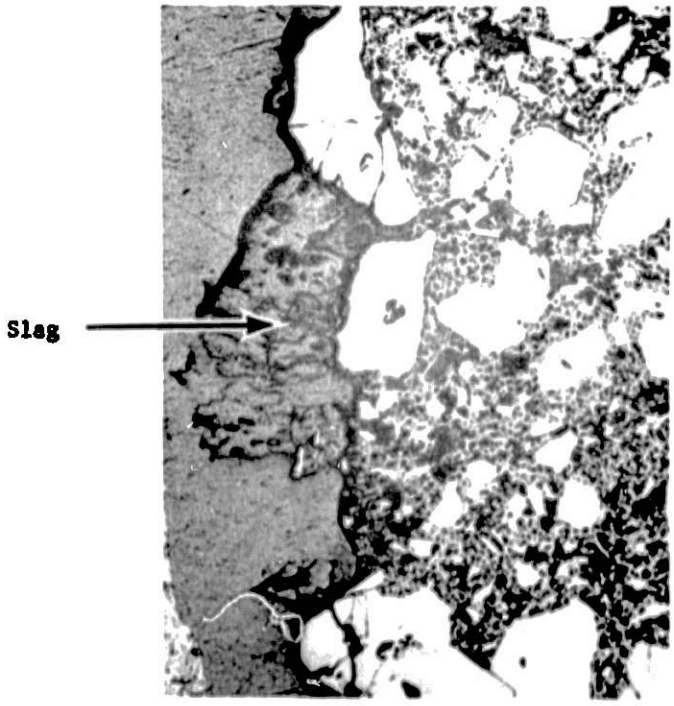

Fig. 9. Polished Section of Nitride-bonded SiC Brick (Number 91) Exposed to Coal Slag Showing the Degree of Slag Penetration. Magnification 32X. ANL Neg. No. 306-77-393.

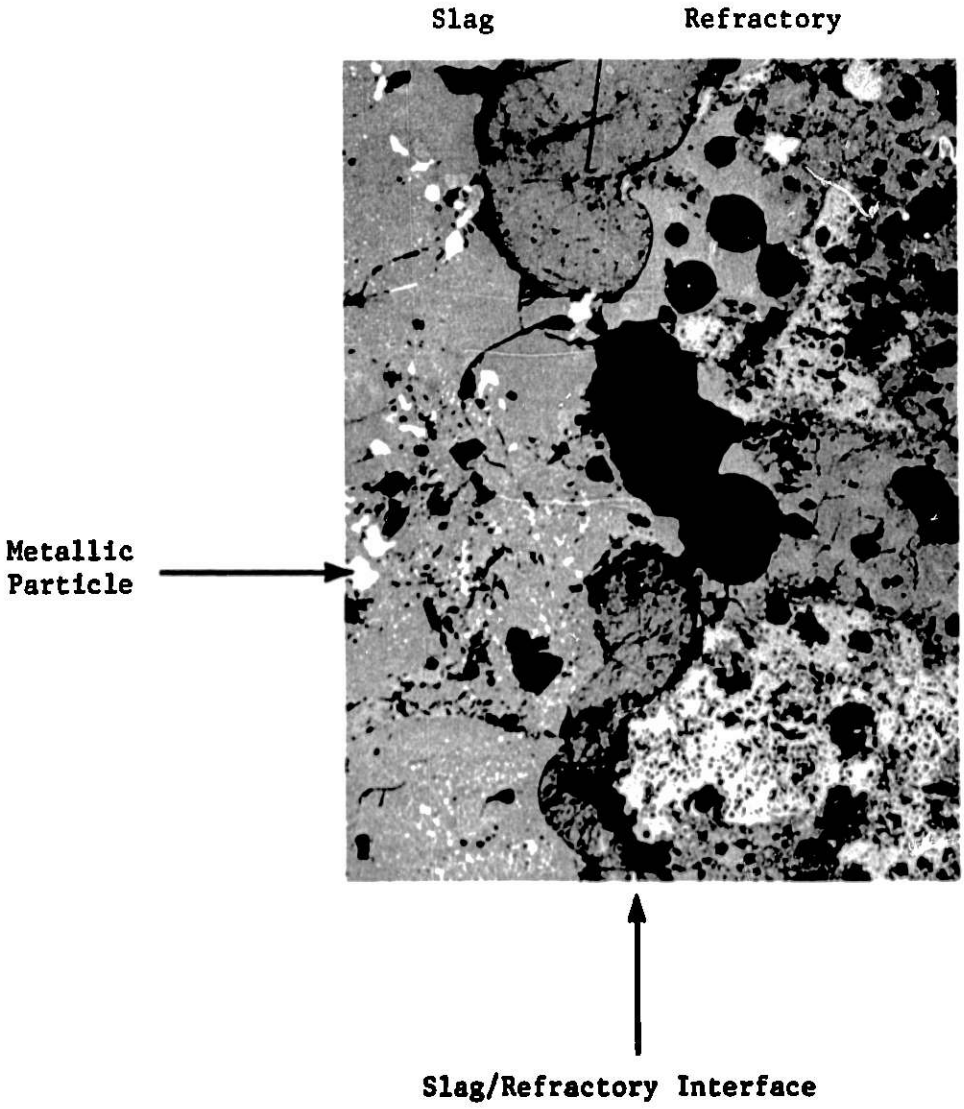

Fig. 10. Polished Section of Silicon-oxynitride Brick (Number 36) Exposed to Coal Slag Showing Refractory on the Right and Slag with Entrained Metallic Particles on the Left. (Taken with reflected light.) Magnification 100X. ANL Neg. No. 306-77-389.

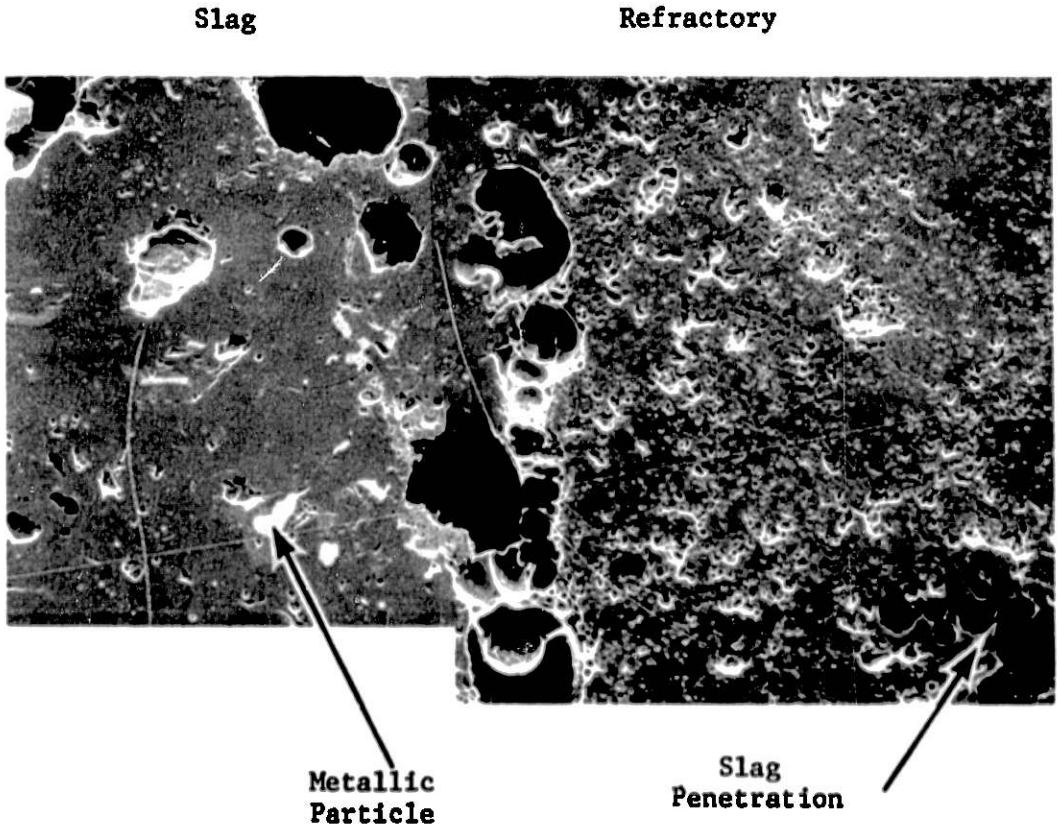

Fig. 11. Scanning-electron Micrograph Showing the Interactions between Slag (Left) and Silicon-oxynitride Brick (Number 36). At lower right corner is an island of slag that has penetrated into the bulk of the refractory. Magnification 150X. ANL Neg. No. 306-77-388.

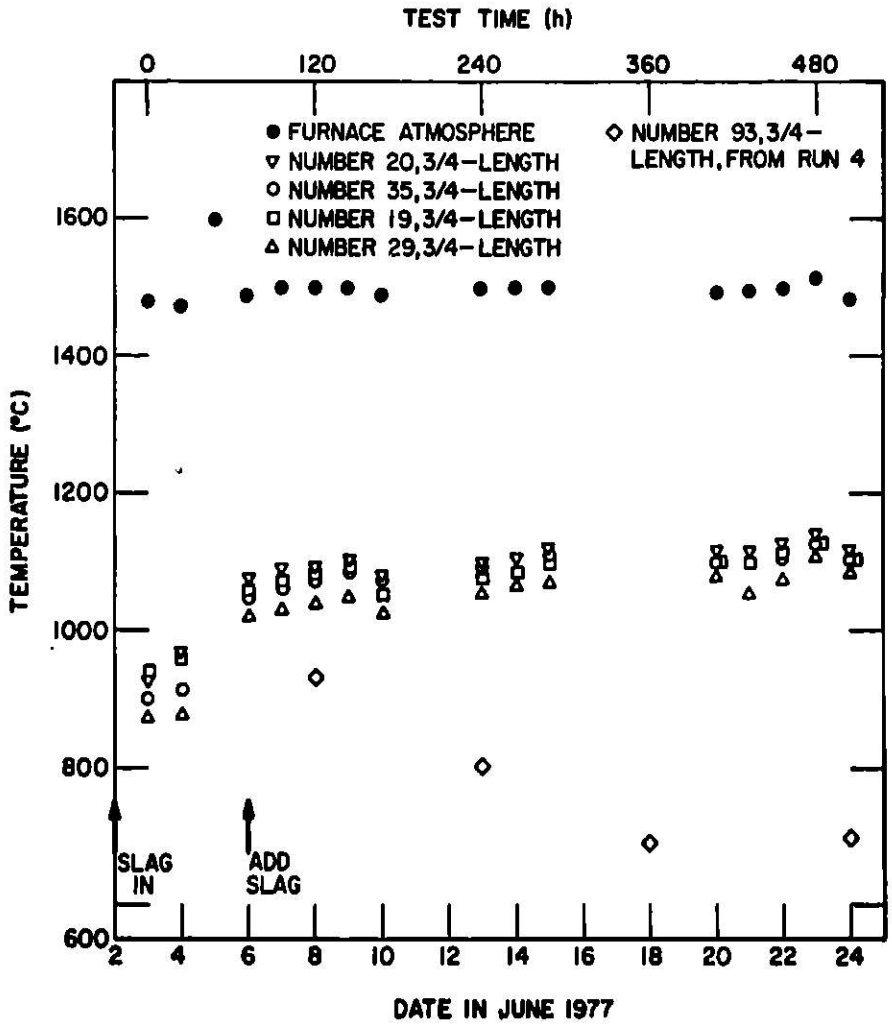

Fig. 12. Furnace Plenum Temperature and Temperature 38.1 mm (1.5 in.) from the Hot Face of Magnesia-chromia 3/4-length Refractory Bricks during Run 5. ANL Neg. No. 306-77-381.

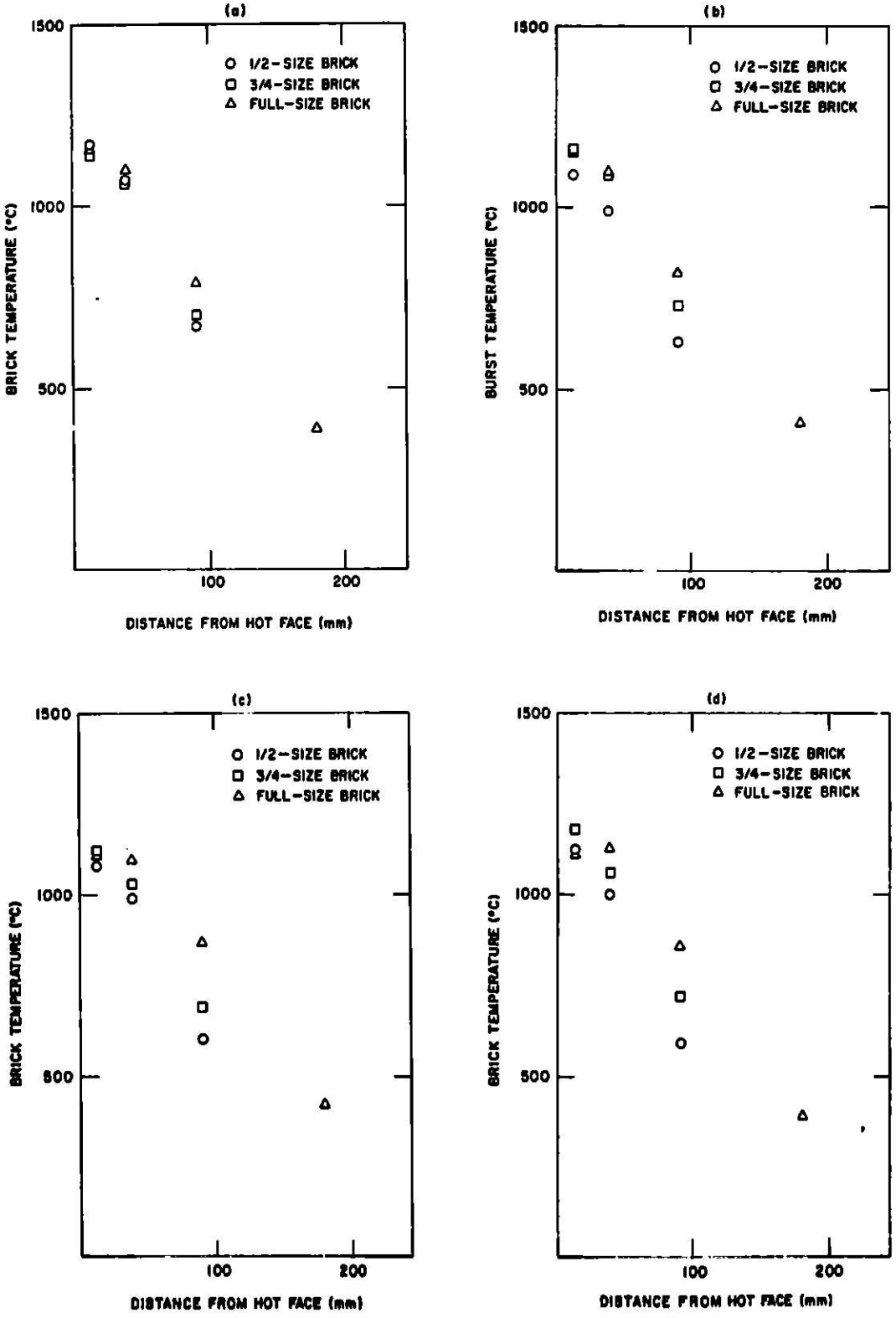

Fig. 13. Temperatures in Magnesia-chromia Bricks during Test Run 5 at Four Locations in Full-length Bricks and at Three Locations in 3/4- and 1/2-length Bricks. (a) Refractory number 19, (b) refractory number 20, (c) refractory number 29, and (d) refractory number 35. ANL Neg. No. 306-77-385.

MILESTONE CHART

FY 1977

Task A — Evaluation of Ceramic Refractories for Slagging Gasifiers

a. Redesign slag-corrosion test rig to provide prototypic temperature profiles

b. Fabricate and assemble new test rig

c. Conduct slag-corrosion resistance tests

d. Perform analysis of refractory samples

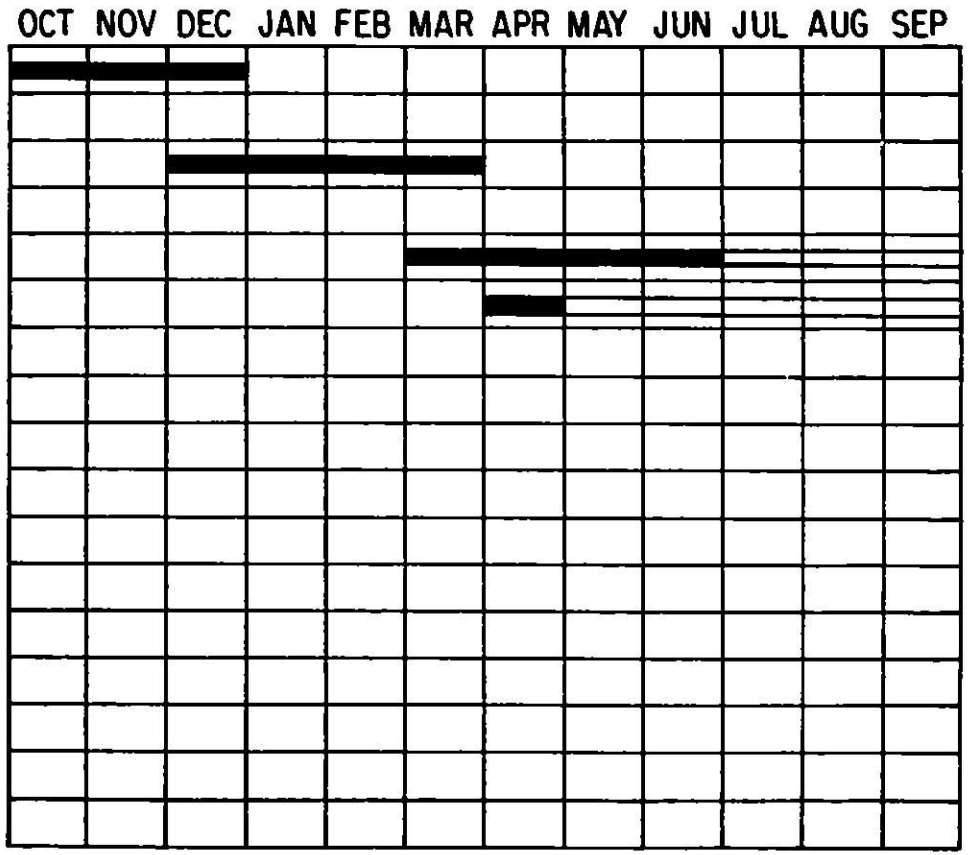

Scheduled

Progress

Scheduled Extension

Task B -- Evaluation of Ceramic Coatings for Coal-conversion Plants
(S. Danyluk, R. B. Poeppel, and G. M. Dragel)

Metallic specimens with partial or total coatings that were described in the previous quarterly report[6] have been shipped to ANL by Solar. Progress on the metallographic investigation of these samples has been delayed because the samples have not been received.

MILESTONE CHART

FY 1977

Task B — Evaluation of Ceramic Coatings for Coal-conversion Plants

a. **Metallographic analysis of coated samples**

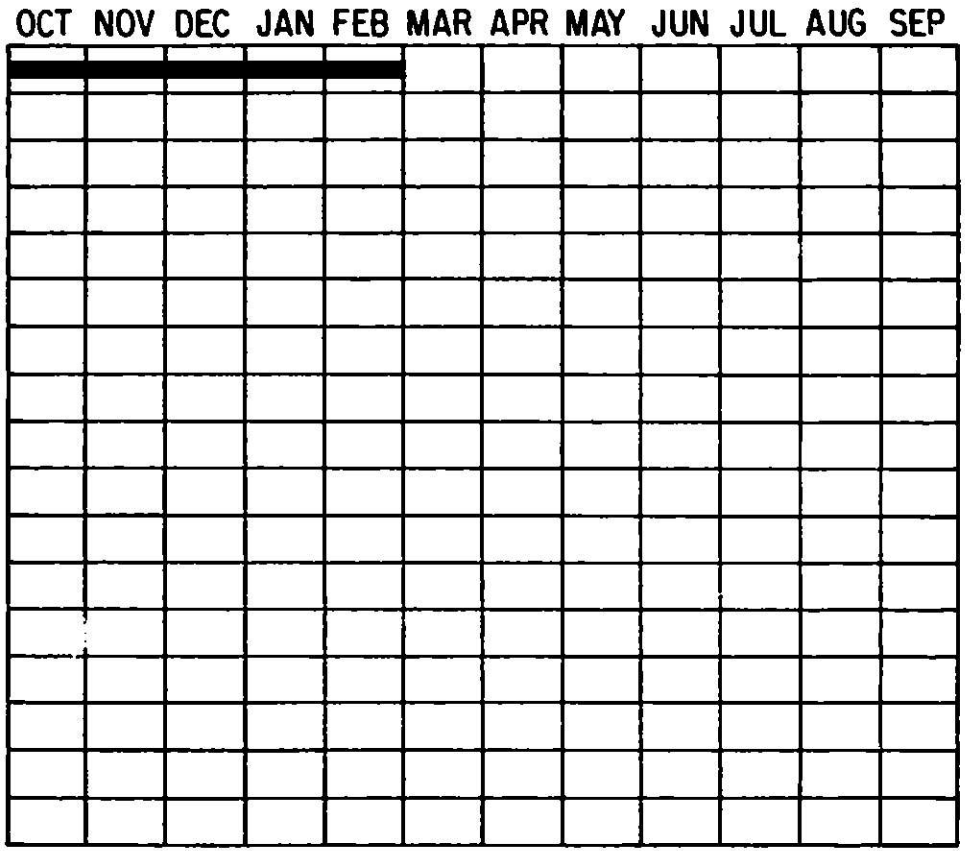

Scheduled

Progress

Scheduled Extension

Task C -- Application and Development of Nondestructive Evaluation Methods for Coal-conversion Processes *(W. A. Ellingson, W. J. Shack, C. L. Johnson, and C. K. Hsieh)*

1. Erosive-wear Detection and Monitoring

a. Metallic Transfer Lines

(1) Field Studies. The in-situ, high-temperature, ultrasonic erosive-wear detection system installed on the Bi-Gas Pilot Plant[5] has been working satisfactorily, and initial erosive wear on the 254-mm (10-in.)-diameter A106B low-carbon steel main coal feed line has been measured. Figure 14 is a schematic of the top blocked-tee measurement locations and shows the thickness loss measured to date. The data indicate that nominally 5% of the wall thickness of the hub has been eroded during the 200 h of exposure. These data will be verified by direct-contact ultrasonic readings to be taken next quarter. To date, the system has operated in an intermittent mode because of the present concern that potential arcing in the electronic data-acquisition system could ignite local gases which have leaked from the gasifier main vessel. A positive-pressure chamber was intended to be constructed around the electronic system to avoid this problem but costs so far have prevented this.

During the past hard winter, the transducers and couplant were exposed to severe weather conditions. This has caused concern as to the reliability of the data. To avoid this exposure, a hood has been designed and fabricated to enclose the waveguides and protect the transducers and couplant. This will be installed in August.

The measurement of erosive wear on the Type 316 stainless steel off-gas blocked tee has been delayed until a stainless steel waveguide design has been finalized. The stainless steel waveguide will permit a similar metal weld to be made rather than a dissimilar weld if the present carbon steel design were to be used. Laboratory studies conducted during the present quarter indicate that a 9.5-mm (3/8-in.)-diameter 7.5-MHz highly damped transducer together with a 9.5-mm (3/8-in.)-diameter knurled waveguide, similar to the carbon steel waveguide previously developed,[3] will work well. Present activities are centered on developing the appropriate field weld parameters so that the new design may be directly attached in the field.

Off-line erosive-wear measurements were made during the present quarter on the HYGAS cyclone separator. The 2000-h exposure data obtained during the recent HYGAS shut-down is in good agreement with the previously obtained data, 0.013 mm/day, as is shown in Fig. 15. The material in this case is Stellite 6B laminated on a Type 316 stainless steel base as previously described.[1,2] The location of the most erosive wear was of interest in this shutdown. The solids outlet neck had grooves with depths greater than 3 mm and this has caused concern.

The ultrasonic erosive-wear detection system installed at the Synthane Plant last year has experienced problems due to the initial complex design that required the over-pressure sleeve previously described.[7] The reliability of the present erosive-wear detection system has negated the

original over-pressure sleeve requirement, and a new Type 304 stainless steel 90°, 305-mm (12-in.) radius elbow has been built and fully instrumented and will be installed in mid-August. The originally installed elbow will be taken out of service and fully characterized for erosive wear both nondestructively and destructively. In addition to the design change in the elbow, recent laboratory studies have shown that a 9.5-mm (3/8-in.)-diameter, 7.5-MHz transducer produces a much sharper pulse and allows repetitive measurements with a variation of ±0.05 mm (±0.002 in.). Thus, the new installation will be cleaner in design, have a higher operational reliability, and provide more accurate data.

b. Refractory-lined Transfer Lines

(1) Infrared. A major effort has been made during the present quarter to develop a three-dimensional model for the study of heat transfer in refractory-lined transfer lines. The system used for analysis is shown in Fig. 16. This is a composite wall structure with a refractory lining cast onto a steel shell. The boundary conditions imposed on the surfaces consisted of a prescribed surface temperature (815°C) on the inside (hot) surface and convective cooling on the outside surface. To economize the numerical solution, planes of symmetry were used where temperature gradients vanished. The heat transfer was studied under steady-state conditions.

A computer program was used to study the thermal patterns for the 27 cavity configurations listed in Table V. The data used in the computation are also given in the table. The data output from the program consisted of an isotherm map, a three-dimensional surface-temperature plot, and a three-dimensional isometric sketch of the cavity configuration. A sample of these outputs for various cavity sizes of depth, total azimuthal angle, and axial length equal to 25.4 mm, 240°, 203.2 mm, respectively, is shown in Fig. 17. Along the axis for angular direction in the three-dimensional plot, point 13 represents the center line of the cavity. The temperature distribution is symmetrical with respect to this center line, which is well demonstrated in both the isotherm map and the three-dimensional temperature plot.

The effect of a change in cavity configuration on the surface temperature distributions is demonstrated in Figs. 18 and 19. A deepening of the cavity increases the peak temperature in the temperature plot (Fig. 18). Also, a slight increase in the edge temperatures occurs when the cavity is is deepened. A marked increase in the volume underlying the temperature surface is observed. This feature is particularly noteworthy since it can be easily measured by means of infrared scanning. A widening of the cavity produces similar results, as shown in Fig. 19.

Two additional features were extracted for comparison: the area enclosed inside isotherm loops and the integrated volume as a function of temperature. The latter is, in essence, an extension of the integrated-volume feature mentioned in the previous paragraph. For this case, the volume is evaluated above each temperature level to examine its capability

in the identification of the flaw. Figures 20 and 21 show these feature curves. The area curves appear to be quite irregular, whereas the integrated energy equivalent (volume) curves are well behaved. These energy curves provide additional features for predicting flaws.

The modeling of heat transfer in a three-dimensional system is essentially complete. Parametric studies involving the effects of the convective heat-transfer coefficient, contact resistance, surface radiative properties, and curvatures are still to be accomplished. In addition, the program will be extended to include the study of a double-layered refractory case. The programs will be helpful to determine the limitations of the infrared scanning method in applications. These are scheduled for the next quarter of work.

2. Refractory-Installation Practices

a. Acoustic Emission

The design of firing schedules to assure long-time reliable operation for castable refractory installations has received relatively little attention. However, recent work[7,8] has addressed this topic. Crowley[7] used time-incremental weighings of samples to determine water loss as a function of time. Givan et al.[8] examined the thermal gradients in various sample sizes so that the interpretation of the strength increase (decrease) of samples subjected to different heat-up rates would be correct and not involve the magnitude of the thermal gradient, which is affected by sample size. The results of Givan et al.[8] show that a sample size with a cross section of 25 x 25 mm, when fired at different heat-up rates, will be reasonably isothermal (ΔT <20°C). With the development of acoustic-emission techniques, recent investigators[9,10] have shown that apparent micro-/macrocrack activity in ceramic (refractory) materials can be detected. The purpose of the work performed in this task is to develop the acoustic-emission technique, with sufficient understanding of the detected acoustic activity, such that better control of the firing schedule of installed refractory concretes can be obtained. Previous work in this task[4] has shown that fast cooling of samples resulted in significant acoustic activity, which perhaps implies the development of large numbers of microcracks. Therefore, seven (7) refractory firings were conducted on high (95%) and low (50-60%) alumina refractories with calcium aluminate bonds to determine the relation of the detected acoustic activity to sample cracking. The methods of sample preparation and the acoustic-emission data acquisition system has been previously described.[6] All samples were 25 x 25 x 260 mm long with thermocouples installed in the samples to establish the differential temperature between the furnace space and the samples. Thermal cycling was employed in the following manner: (1) 0 to 120°C in 8 h followed by a preselected cool-down schedule, either furnace cooling or programmed linear cool, (2) reheat to 500°C in 8 h followed by one of the aforementioned cooling schedules, and (3) heat to 1000°C in 24 h, hold for 2 h and then cool at one of the selected cooling schedules. The acoustic-emission data obtained was plotted as total ringdown counts and as count rate, dN/dt, versus time.

To obtain characteristic acoustic data on high, medium, and low alumina refractories, products with similar bonding material from several manufacturers will be examined. This quarter, two high-alumina and one low-alumina products were examined.

Figure 22a shows typical total counts versus time for a 95% alumina refractory from producer A, and Fig. 22b shows the sensitivity of count rate to the change in output counts. Data in Fig. 22 are for a linear cool down. Note that, at the end of the 1000°C run when cooling began, little change in acoustic activity is detected. Figure 23a shows counts versus time for exponential (furnace) cooling of the same refractory materials, and Fig. 23b shows the count rate. Note in Fig. 23b that a significant acoustic activity is detected immediately after the 1000°C run while the steep cooling rate is taking place. Figures 24 and 25 show the characteristic acoustic emission obtained from the low-alumina (60%) samples. The differences in detected acoustic activity between the high- and low-alumina samples are (1) the high-alumina samples yield higher total ringdown counts and higher count rates than the low-alumina samples, and (2) the effect of exponential cooling on acoustic activity is much less severe on the low-alumina samples. This is in agreement with data reported earlier[4] (Fig. 26), which indicated that the counts per acoustic event are greater for the high-alumina (high density) refractory than for the low-alumina (low density) refractory. To be noted in all samples tested, however, is the fact that the highest acoustic activity occurs during heatup to 500°C. This is in agreement with the evidence available in the literature.[11] In the next quarter, larger samples 75 x 75 x 250 mm will be fired at similar heating and cooling rates as well as with very rapid heating to produce large cracks. This will allow a better definition of comparative acoustic-emission signatures.

3. Component Inspection

a. Acoustic Monitoring of Valves

During the present quarter, acoustic monitoring of a full-size ball valve was carried out at the MERC-VTF through the cooperation of John Gardner (Project Leader, Valve Test Facility). The valve examined was a Jamesbury 4-in. ball valve (Fig. 27). It was mounted in the static test facility at MERC, which is a blowdown-type test system. A plenum chamber is pressurized with dry air, and the leak rate through the test valve is determined by recording the pressure decay within the plenum chamber. The pressure-decay curves are recorded on a strip-chart recorder; the leak rate can be determined from the pressure-decay curves and the known volume of the plenum chamber.

The acoustic-monitoring system used consisted of an AET 201 signal-channel processor, an AET 140A preamplifier, and an HP 3475B digital multimeter. A Tektronix 314 portable oscilloscope was used to visually monitor the acoustic-emission system. The preamplifier and signal processor combination were set to give an overall gain of 100 dB. Three transducers were examined: AET Models 175L, 375L, and 750L. These are resonant response transducers with peaks at 175, 375, and 750 kHz, respectively.

The 4-in. valve examined was a "good" valve with relatively little leakage. The leakage rate considered acceptable by MERC is 1.8×10^{-5} $m^3/s/mm$ (1 cfm/in.) diameter. Thus, for the 102-mm (4-in.)-diameter valve used in the present experiments, the maximum acceptable leak rate is 1.8×10^{-3} m^3/s (4 cfm). The maximum leak rate in the present tests was only 7.2×10^{-4} m^3/s (1.6 cfm), well within the limit of acceptability.

For each test, the valve was pressurized, acoustically monitored for 10 s, and then depressurized and cycled in preparation for the next test. For safety reasons, the maximum test pressures were limited to 1.03 MPa (150 psi). Initially, the valve was monitored at three locations, as shown in Fig. 28a-c; however, no significant difference was observed for the measurements at the three locations, and thus the bulk of the measurements were made on the valve flange (Fig. 28a).

The results obtained using the 175-kHz transducer are shown in Table VI;* the root-mean-square (rms) acoustic-emission values in Table VI should be compared with the background noise level of 0.218 V. The first two tests showed extremely high acoustic-emission levels, which completely saturated the electronics; in this case, the valve was leaking through the stem. After the valve was recycled and taken through a sequence of high- and low-pressure runs, the leakage seemed to be primarily internal. The data in Table VI show a rough correlation between acoustic output and leakage rate. The correlation is slightly better between the acoustic output and the driving pressure across the valve. For pressures >0.90 MPa (130 psi), the acoustic output is fairly strong; a threshold level appears to occur at ∿0.84 MPa (123 psi) or a leakage rate of 1.55 m^3/s (0.86 cfm).

Data in Tables VII and VIII show that the 375 and 750 kHz transducers are much less sensitive in detecting leakage than the 175 kHz transducer, as was expected from our previous experience and laboratory testing. However, since the background noise levels were 0.218 and 0.215 V, respectively, both transducers were able to detect even the relatively low levels of leakage occurring in this valve.

Previous field testing has indicated that the 175 and 375 kHz transducers are too sensitive to structure-borne noise to be used in operating gasification plants. The rapid attenuation of higher frequencies makes the 750 kHz transducer an excellent choice in terms of background noise rejection. The present tests indicate that, although the 750 kHz transducer is much less sensitive than the 175 kHz transducer, it can detect leakage at relatively low levels. During the next quarter, additional field testing will be carried out on full-size valves to confirm the initial results reported here and to establish a threshold level of acoustic emission for unacceptable leakage rates.

---

*The leakage rates presented in Tables VI-VIII were computed by R. G. Hornbeck of the MERC staff from the pressure-decay data.

TABLE V. Test Conditions

System Dimensions

ID = 101.6 mm

OD = 266.7 mm

Refractory Thickness = 76.2 mm

Height = 508 mm

Parameters Related to Boundary Conditions

T_o = 815.5°C

R_∞ = 26.6°C

$h = 5.68 \times 10^{-5}$ W/mm^2·°C

Parameters Related to Material Properties

$k_1 = 6.62 \times 10^{-4}$ W/mm·°C

$k_2 = 4.67 \times 10^{-2}$ W/mm·°C

Cavity Sizes Tested

Depth = 12.7, 25.4, 38.1 mm

Angular Span = 120, 180, 240 deg

Height = 101.6, 203.2, 304.8 mm

TABLE VI. Acoustic Emission rms (V) and Leakage Rate (175 kHz Resonant Transducer)

Pressure			Leakage Rate	
MPa	(psi)	AE rms (V)[a]	m^3/s	(Cfm)
1.02	(148)	∿3.58	2.9×10^{-5}	(1.57)
0.95	(138)	∿3.58	2.0×10^{-5}	(1.07)
0.95	(138)	0.80	1.67×10^{-5}	(0.92)
0.94	(136)	0.55	1.67×10^{-5}	(0.98)
0.92	(133)	0.30	1.51	(0.84)
0.91	(132)	0.231	1.62	(0.90)
0.91	(132)	0.36	1.69	(0.94)
0.90	(130)	0.38	1.67	(0.93)
0.89	(129)	0.221	1.53	(0.85)
0.88	(128)	0.220	1.58	(0.88)
0.87	(126)	0.230	1.67	(0.93)
0.84	(123)	0.220	1.55	(0.86)

[a]Background level 0.218 V.

TABLE VII. Acoustic Emission rms (V) and Leakage Rate (375 kHz Resonant Transducer)

Pressure			Leakage Rate	
MPa	(psi)	AE rms (V)[a]	m^3/s	(Cfm)
0.96	(139)	0.222	1.82	(1.01)
0.96	(139)	0.240	1.85	(1.03)
0.94	(136)	0.221	1.69	(0.94)
0.94	(136)	0.220	1.78	(0.99)
0.92	(134)	0.218	1.73	(0.96)
0.91	(132)	0.218	1.78	(0.99)
0.88	(128)	0.218	1.58	(0.88)

[a]Background level 0.218 V.

TABLE VIII. Acoustic Emission rms (V) and Leakage Rate (750 kHz Resonant Transducer)

Pressure			Leakage Rate	
MPa	(psi)	AE rms (V)[a]	m^3/s	(Cfm)
1.07	(155)	0.219	1.89	(1.05)
1.05	(153)	0.218	1.82	(1.01)
1.03	(150)	0.215	1.93	(1.07)
1.00	(145)	0.215	1.75	(0.97)

[a]Background level 0.215 V.

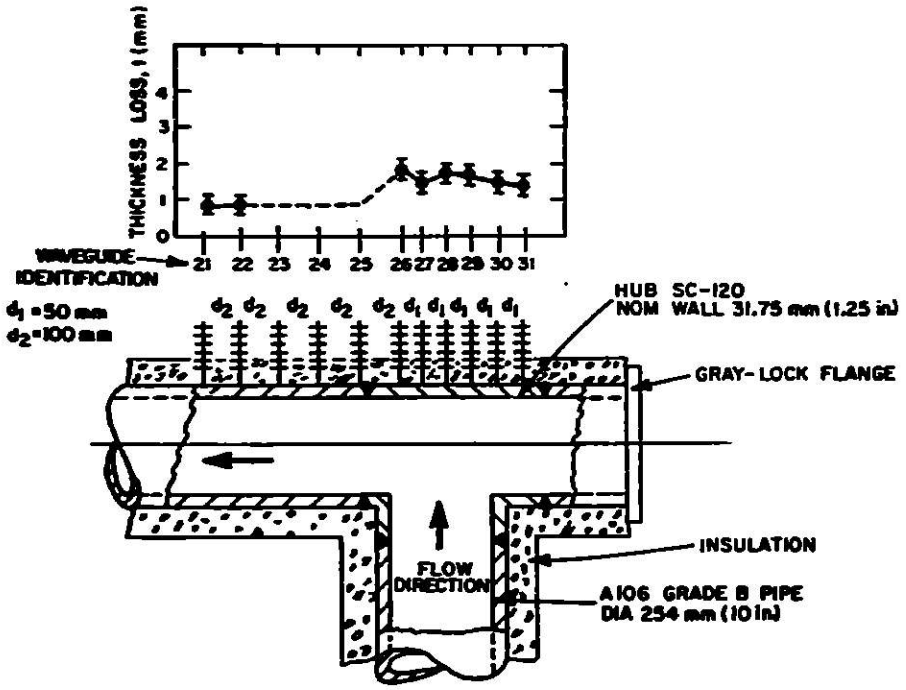

Fig. 14. Schematic of Bi-Gas Erosive-wear Detection Locations on Blocked Tee and Initial Erosive-wear Pattern Detected after 200-h of Exposure. ANL Neg. No. 306-77-374.

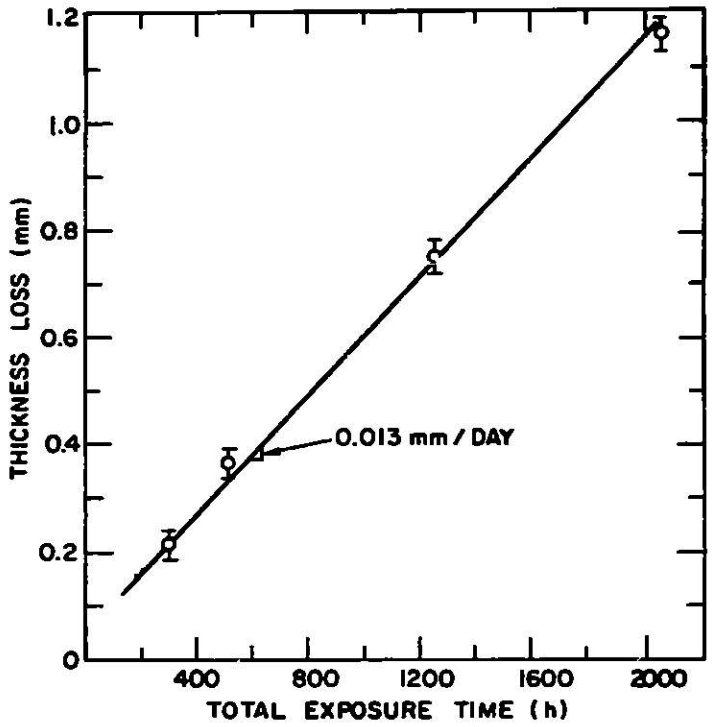

Fig. 15. Erosive Wear of Stellite 6B Hard Facing on HYGAS Cyclone Separator as Measured by Ultrasonic Techniques. ANL Neg. No. 306-77-373.

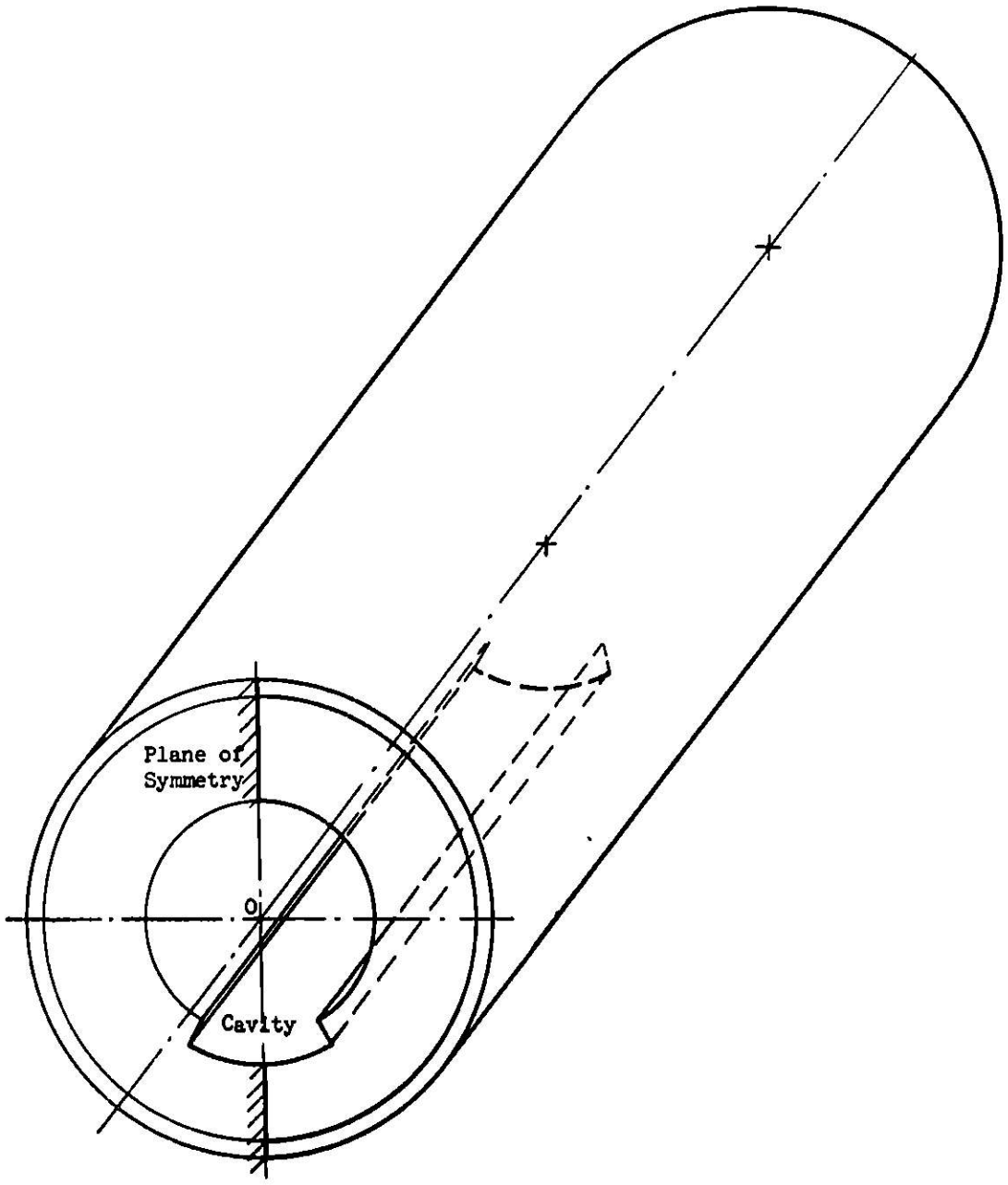

Fig. 16. A Three-dimensional Model in Cylindrical Coordinates. ANL Neg. No. 306-77-396.

SURFACE ISOTHERM MAP:

LEGEND:

SYMBOL	ISOTHERM BAND WIDTH (Deg.)
A	93.3 to 95.9
B	98.6 101.2
C	103.8 106.5
D	109.2 111.7
E	114.5 117.1
F	119.7 122.3
G	125.0 127.6
H	130.3 132.9
I	135.6 138.2
J	140.9 143.5
K	146.2 148.8

```
**************************
EEEEEEE             EEEEEEE
EEEE      FFFFFFF       EEEE
   FF  GGGGGGGGGGG  FF
FF G   III      III   G FF
  G  I JJ         JJ I  G
  GH  J      K      J  HG
  G  I JJ         JJ I  G
FF G   III      III   G FF
   FF  GGGGGGGGGGG  FF
EEEE      FFFFFFF       EEEE
EEEEEEE             EEEEEEE
**************************
```

THREE-DIMENSIONAL SURFACE TEMPERATURE PLOT

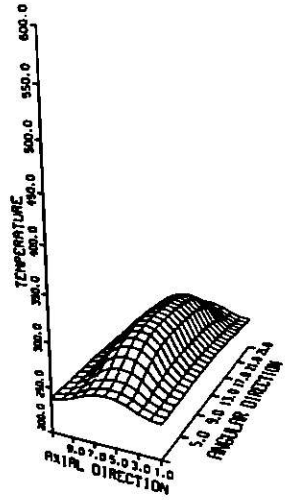

RECONSTRUCTION OF CAVITY CONFIGURATION

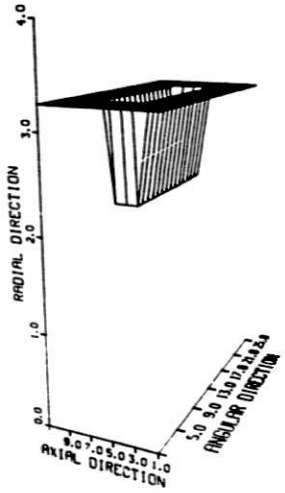

Fig. 17. A Sample Presentation of Cavity Configuration and Temperature Data. ANL Neg. No. 306-77-401.

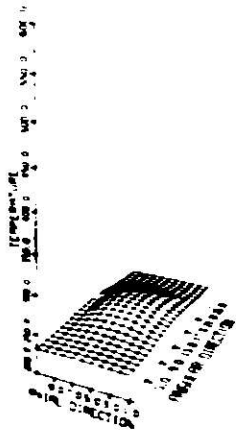

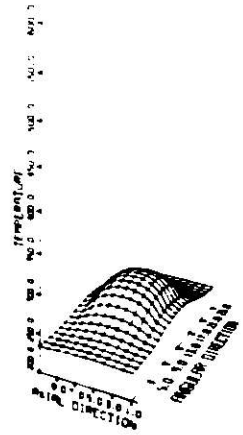

THREE-DIMENSIONAL SURFACE TEMPERATURE PLOT

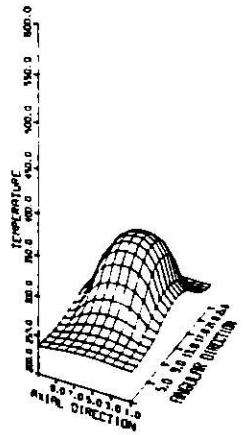

RECONSTRUCTION OF CAVITY CONFIGURATION

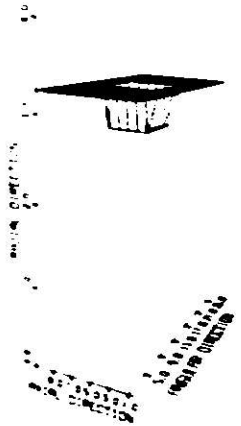

Cavity Size:

(12.7 mm x 120° x 304.8 mm)

RECONSTRUCTION OF CAVITY CONFIGURATION

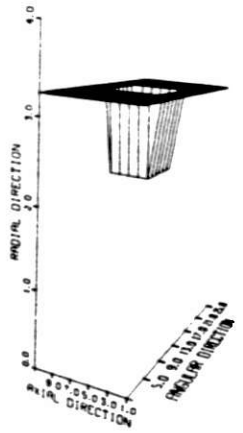

(25.4 mm x 120° x 304.8 mm)

RECONSTRUCTION OF CAVITY CONFIGURATION

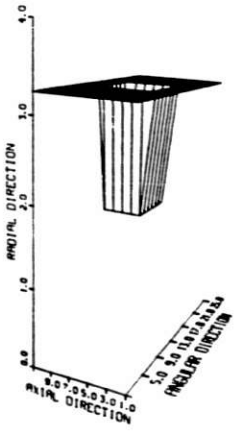

(38.1 mm x 120° x 304.8 mm)

Fig. 18. Effect of Cavity Depth on Temperature Data. ANL Neg. No. 306-77-398.

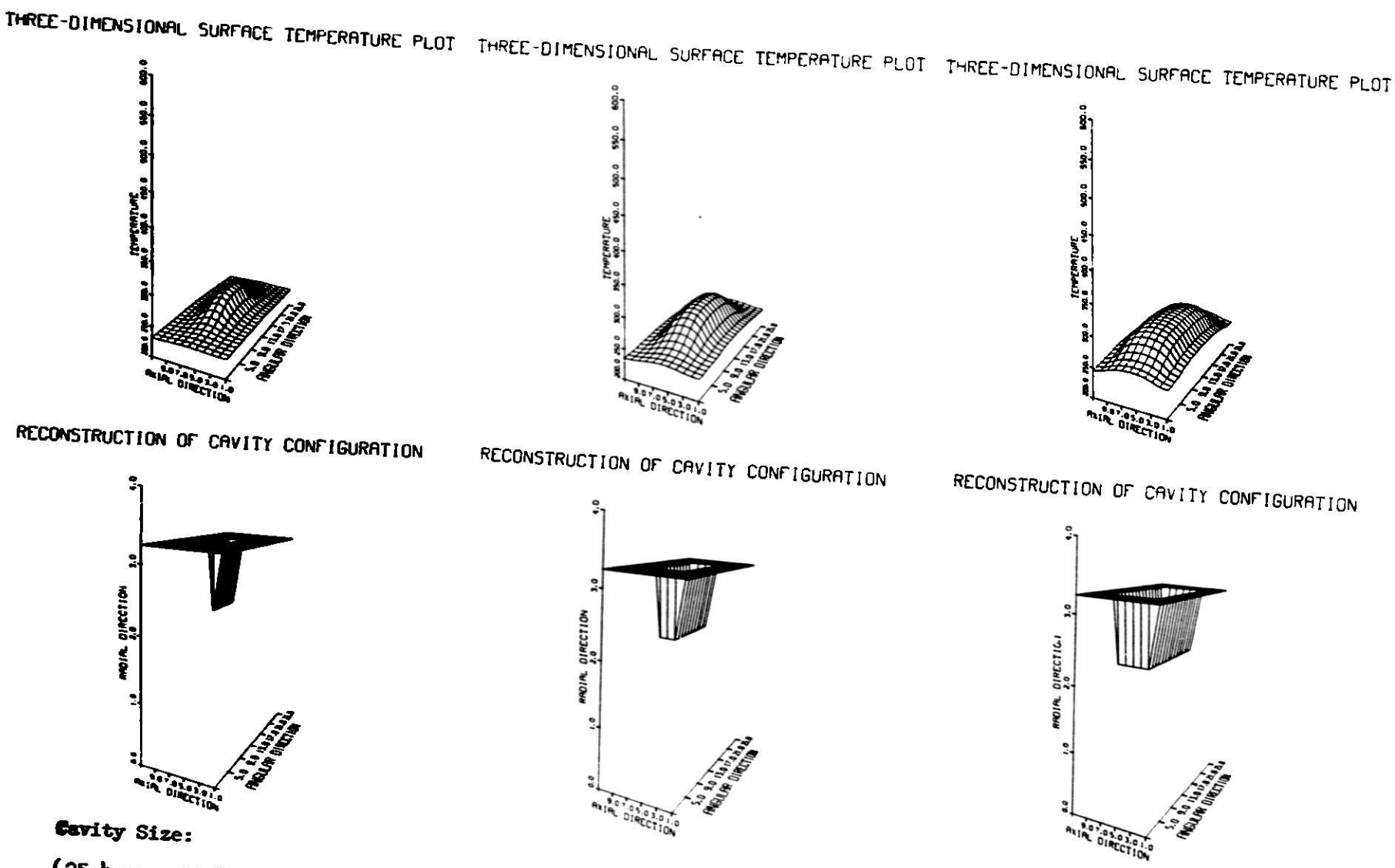

Fig. 19. Effect of Cavity Width on Temperature Data. ANL Neg. No. 306-77-399.

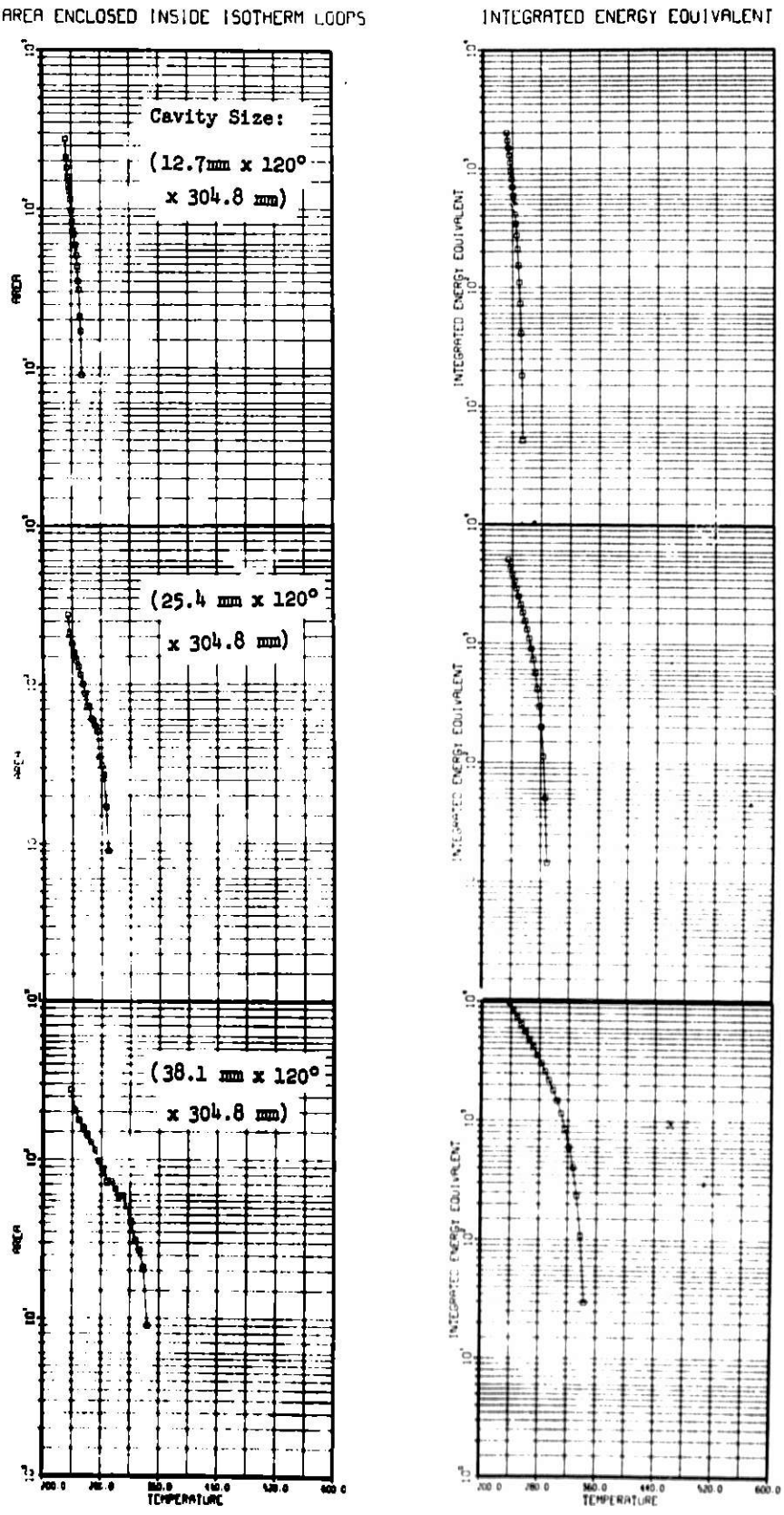

Fig. 20. Feature Curves for Gases Given in Fig. 18. ANL Neg. No. 306-77-397.

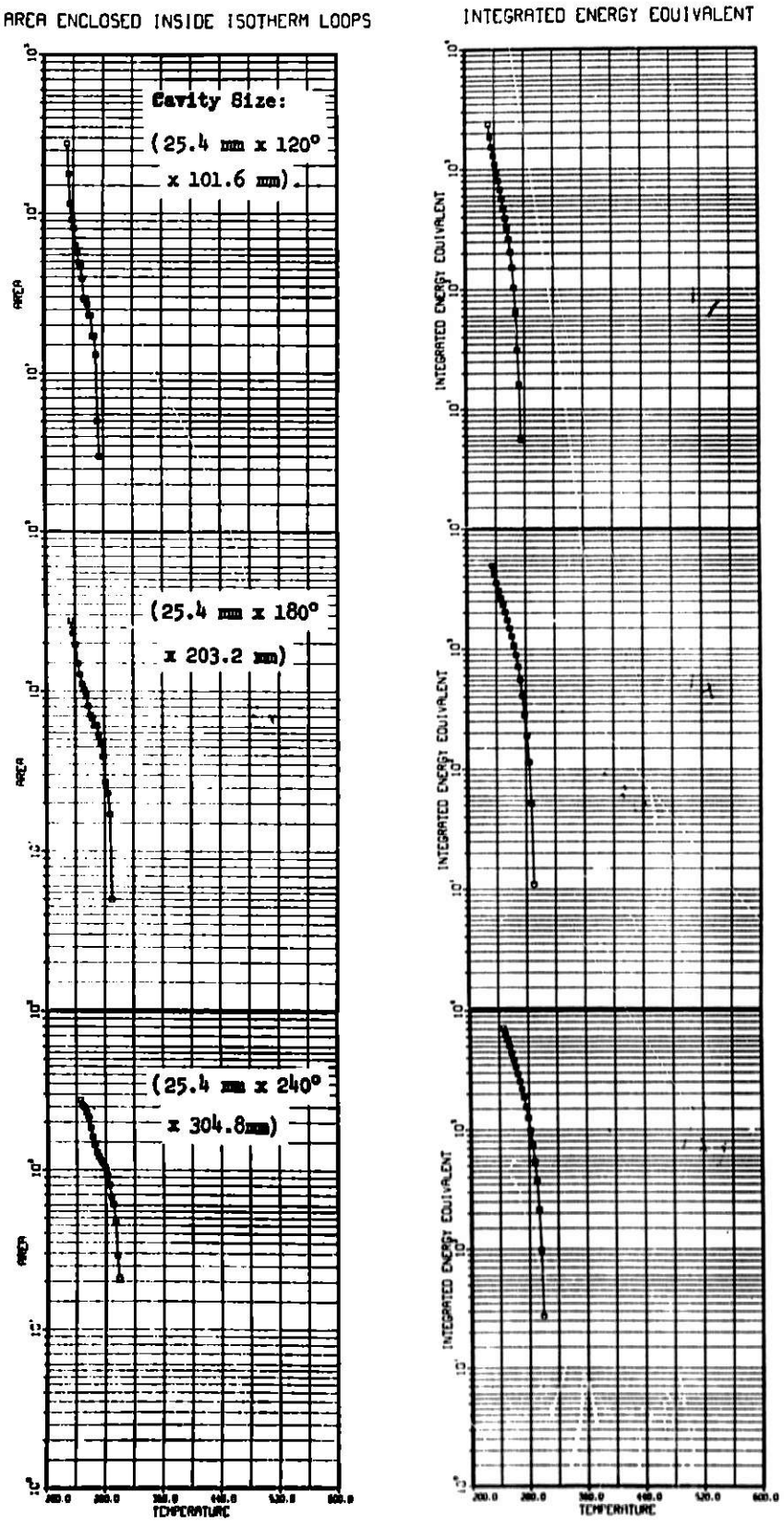

Fig. 21. Feature Curves for Gases Given in Fig. 19. ANL Neg. No. 306-77-400.

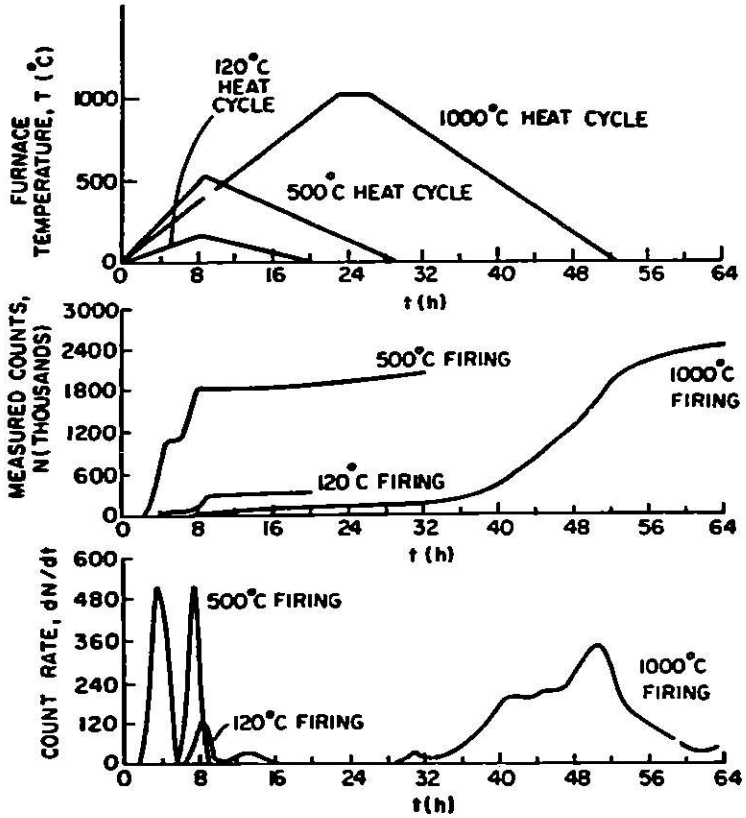

Fig. 22. Characteristic Acoustic Emission Obtained from Monolithic, Isothermally Heated, Refractory Specimens of 95% Alumina with Controlled Cooling. (a) Total ringdown counts vs time for sample under thermaly cycling and (b) count rate vs time for data in (a). ANL Neg. No. 306-77-408.

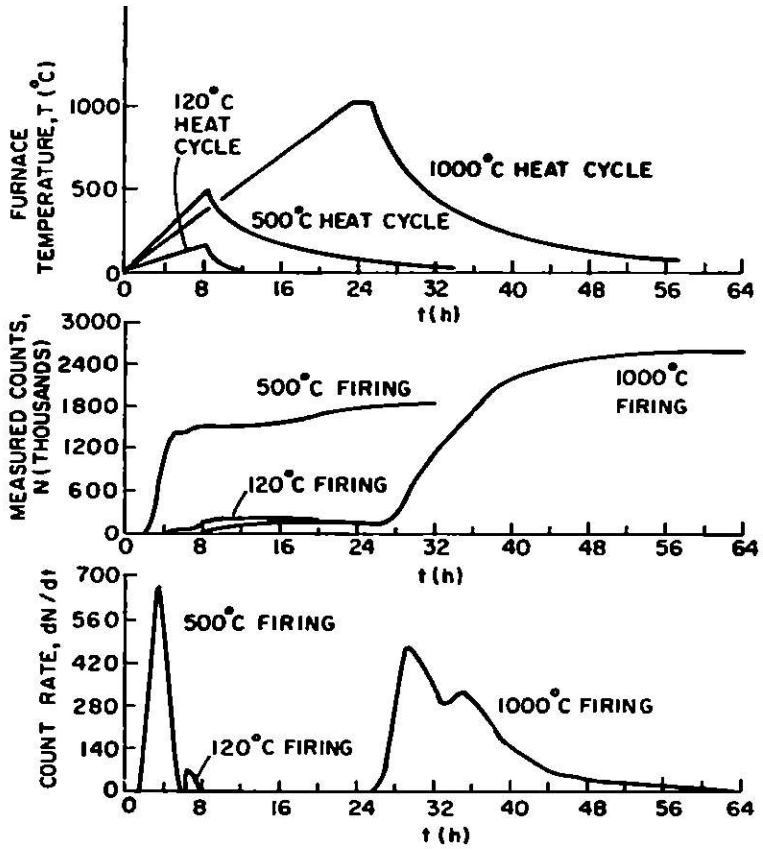

Fig. 23. Characteristic Acoustic Emission Obtained from Monolithic, Isothermally Heated, Refractory Specimens of 95% Alumina with Exponential (Furnace) Cooling. (a) Total ringdown counts vs time for sample under thermal cycling and (b) count rate vs time for data in (a). ANL Neg. No. 306-77-411.

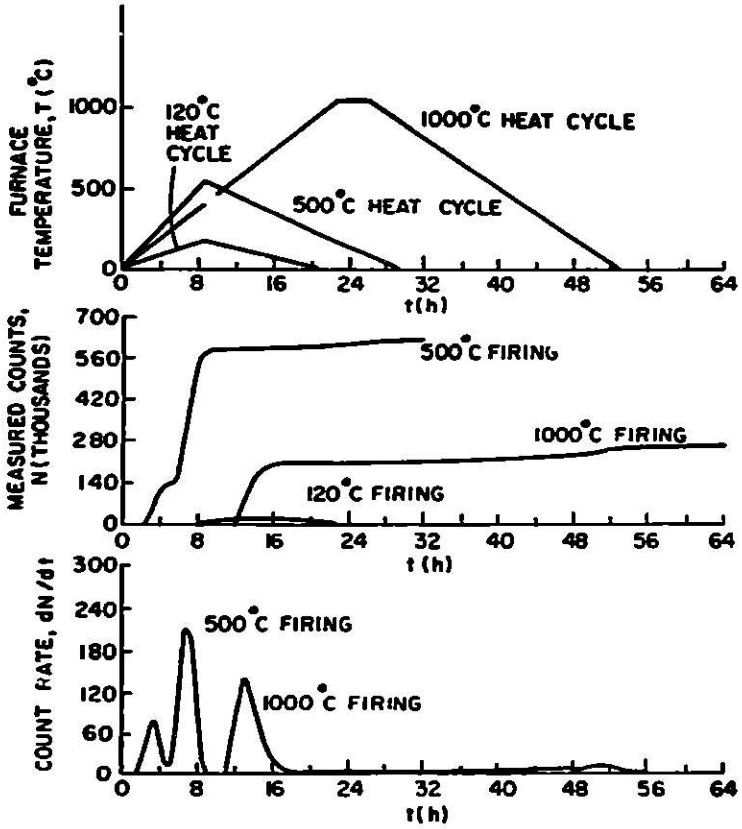

Fig. 24. Characteristic Acoustic Emission Obtained from Monolithic, Isothermally Heated Refractory Specimens of 60% Alumina with Controlled Cooling. (a) Total ringdown counts vs time for sample under thermal cycling and (b) count rate vs time for data in (a). ANL Neg. No. 306-77-409.

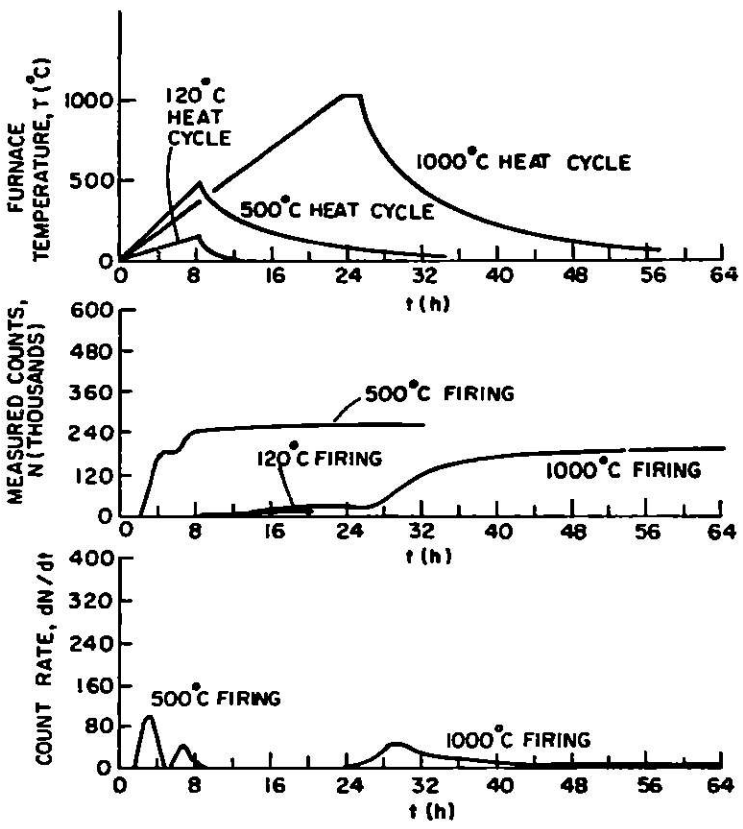

Fig. 25. Characteristic Acoustic Emission Obtained from Monolithic, Isothermally Heated Refractory Specimens of 60% Alumina with Exponential (Furnace) Cooling. (a) Total ringdown counts vs time for sample under thermal cycling and (b) count rate vs time for data in (a). ANL Neg. No. 306-77-410.

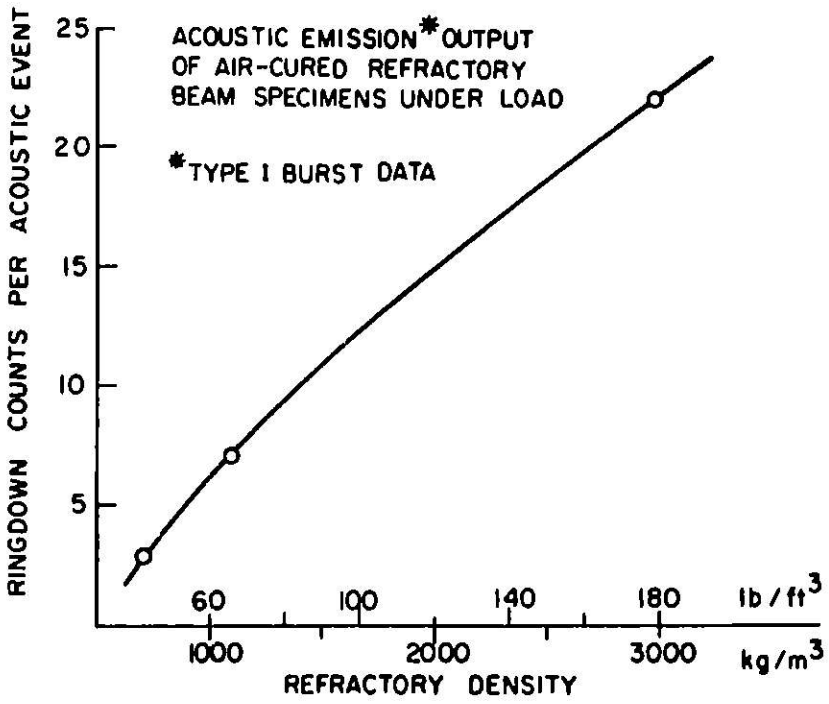

Fig. 26. Detected Acoustic Activity for Various Refractory Densities when Fractured under Load. ANL Neg. No. 306-77-407.

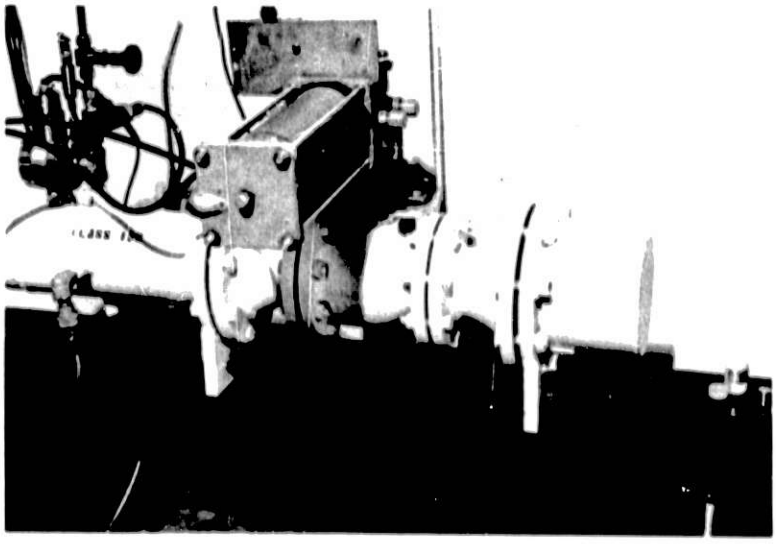

Fig. 27. Jamesbury 4-in. Ball Test Valve as Installed in MERC Static Valve Facility. ANL Neg. No. 306-77-395.

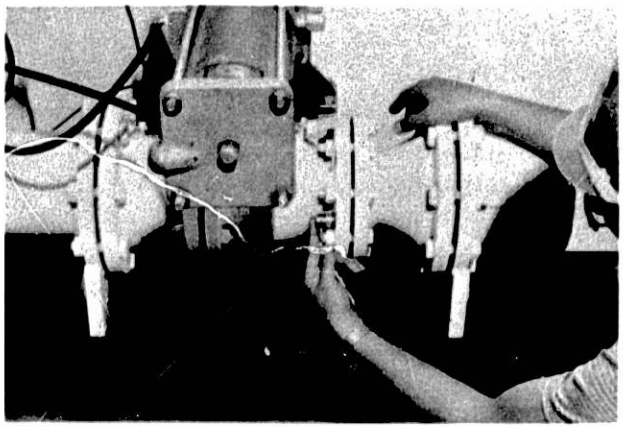

(a)

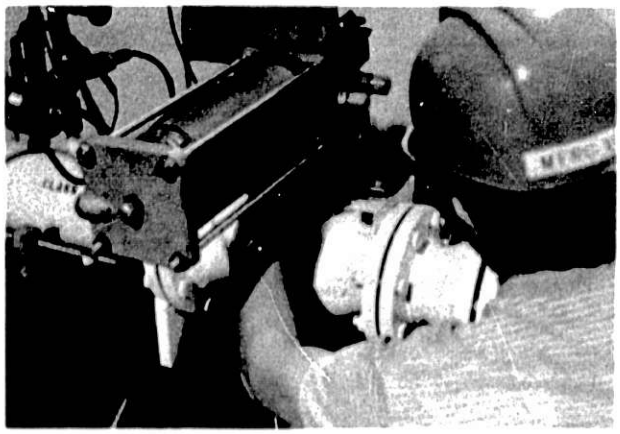

(b)

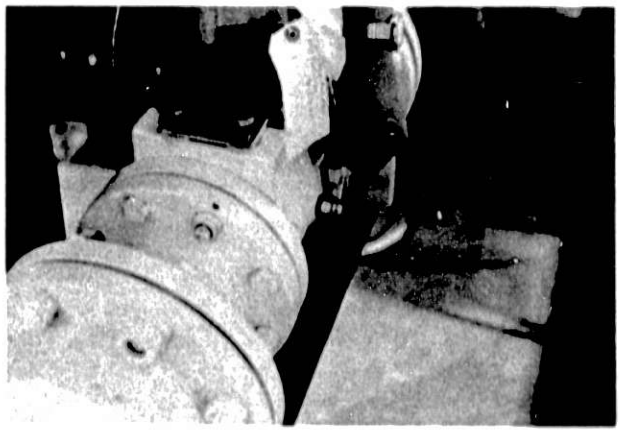

(c)

Fig. 28. Transducer Locations for Acoustic Monitoring. ANL Neg. No. 306-77-383.

MILESTONE CHART

FY 1977

C-1 — Acoustic Emission for Refractory-installation Procedures

a. Study sensitivity of acoustic emission to cracking during curing

b. Examine crack patterns by dye penetrant, gamma radiography

c. Perform metallographic examinations and correlate cracking with acoustic emission

d. Determine mechanical properties for the refractories and correlate mechanical properties to acoustic-emission parameters

e. Initiate tests on the refractories in simulated coal-conversion environments

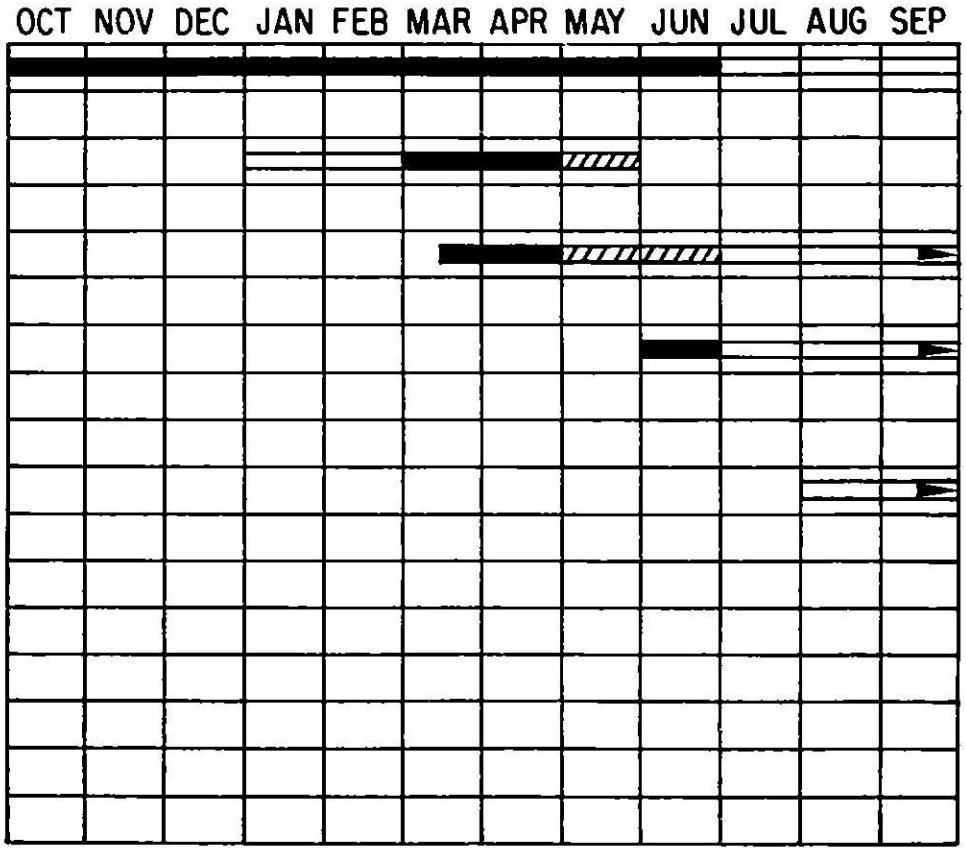

Scheduled

Progress

Scheduled Extension

MILESTONE CHART

FY 1977

C-2 — Valve Leak Detection

a. Noise survey in operating conversion plants

b. Cross talk tests

c. Recommendations for a qualitative leak-detection system

d. Stand-off wave guides

e. Quantitative detection system

f. Full-size valve tests at MERC

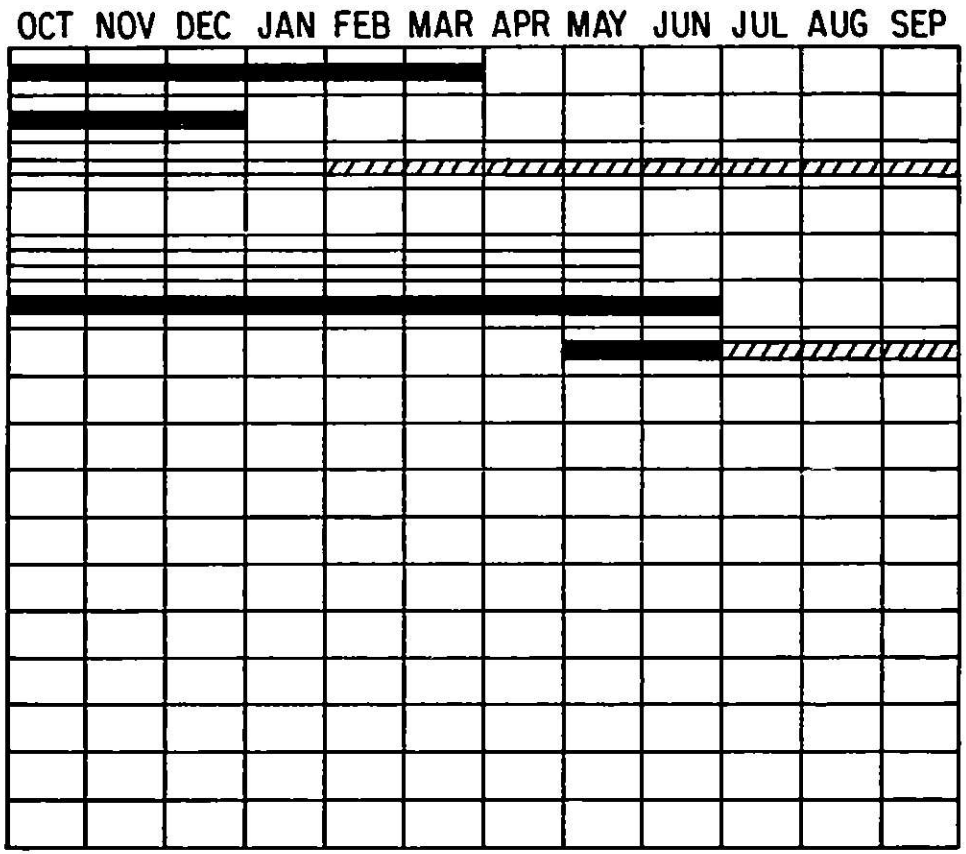

Scheduled

Progress

Scheduled Extension

MILESTONE CHART

FY 1977

C-3 — Application of Passive Infrared Imaging

a. Bibliographic search

b. Develop analytical heat-transfer models

c. Modify computer image analysis of infrared images studying time-dependent fluctuations

d. Conduct laboratory studies to verify analytical model

e. Conduct field studies on CO_2 Acceptor two-component transfer line

f. Conduct field studies as needed on pilot and demonstration plants

g. Initiate work on relating thermal warping of valve bodies to valve design

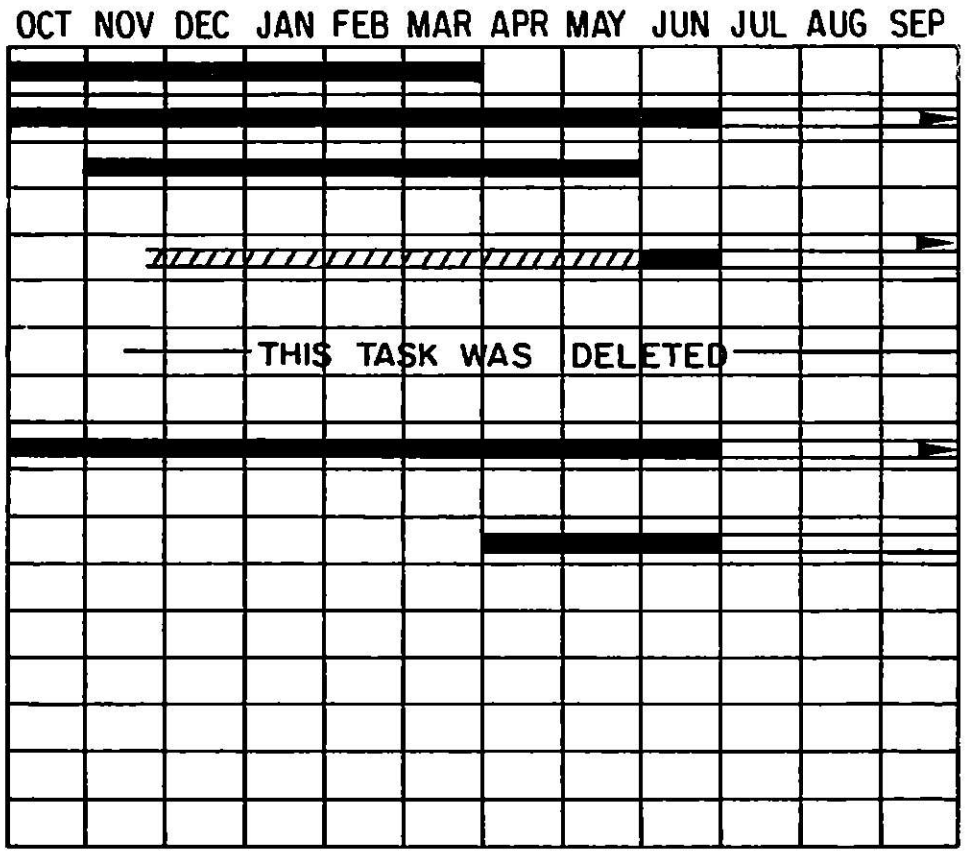

Scheduled

Progress

Scheduled Extension

MILESTONE CHART

FY 1977

C-4 — Ultrasonic Studies Related to Coal-conversion Systems

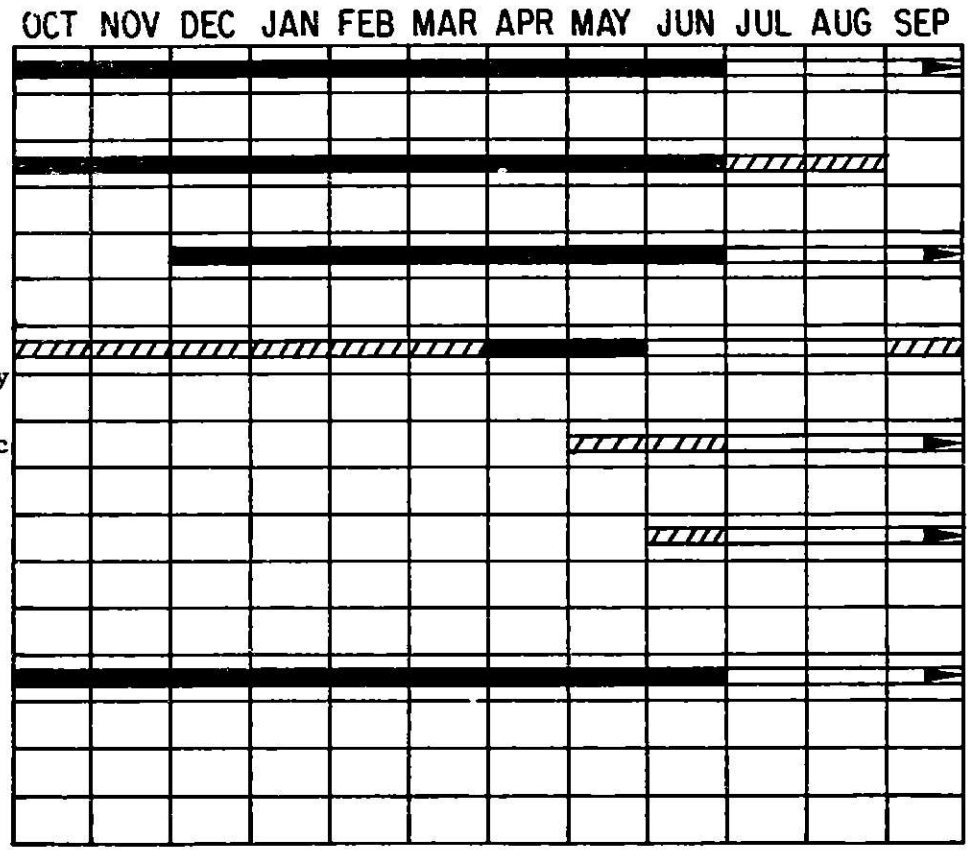

a. Collect data from Synthane installation and analyze

b. Complete field installation at the Bi-Gas System

c. Collect and analyze data from Bi-Gas installation

d. Study effect of channeling on reflected signal characteristics and relate to reliability

e. Initiate study on applicability of ultrasonic testing to corrosion-induced wall thinning

f. Initiate work on high-temperature transducer design and electronic-transfer-function characteristics

g. Conduct specialized field activities in direct support of pilot and demonstration plants

Scheduled

Progress

Scheduled Extension

MILESTONE CHART

FY 1977

C-5 — Gamma Radiography for Application to Refractory-layered Structures

a. Conduct literature search on gamma radiography for application to porous media

b. Report results of Bi-Gas field tests

c. Conduct field test at Battelle on transfer line

d. Compare gamma radiographs to infrared images

e. Continue laboratory studies on spatial resolution for bore definition

f. Conduct studies on full-scale mockups

g. Conduct specialized field tests on demand from pilot and demonstration plants

h. Continue crack-resolution studies in the laboratory

i. Initiate work on slag-refractory thickness ratios versus film density

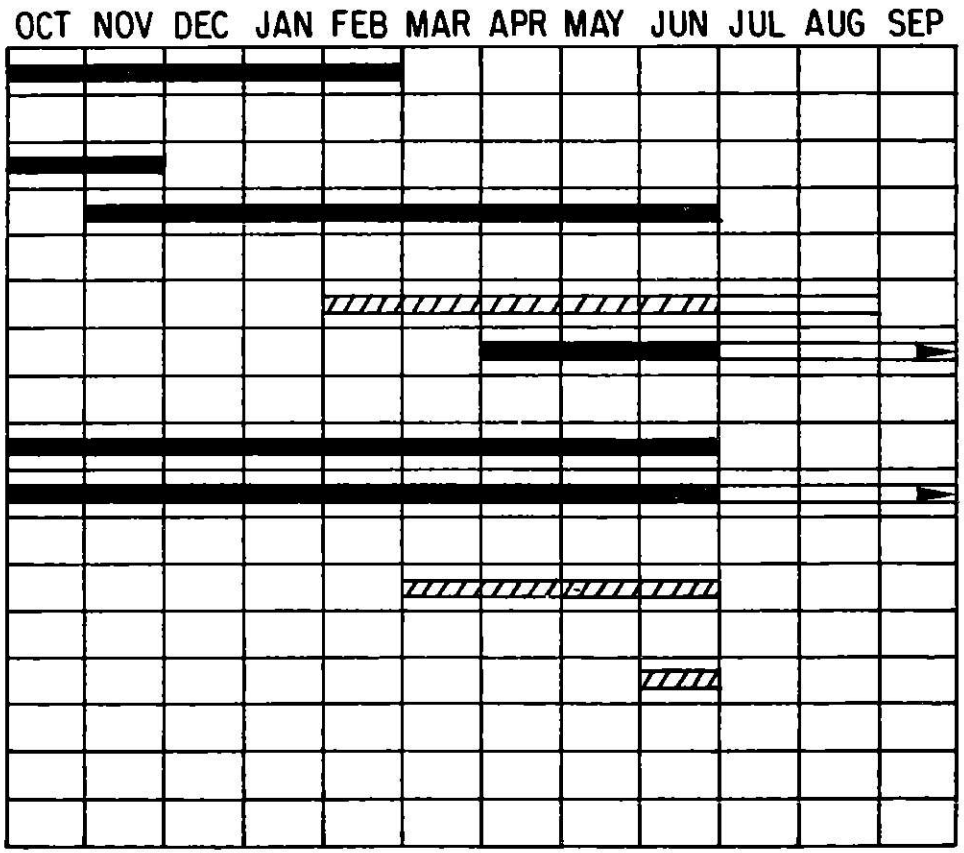

Scheduled

Progress

Scheduled Extension

Task D -- Corrosion Behavior of Materials in Coal-conversion Processes
(K. Natesan and O. K. Chopra)

The objectives of this program are to (1) develop uniaxial tensile data on four selected commercial alloys upon exposure to multicomponent gas environments, (2) experimentally evaluate the high-temperature corrosion behavior of iron- and nickel-base alloys in gas environments with a wide range of oxygen, sulfur, and carbon potentials, and (3) develop a systems approach based upon available thermodynamic and kinetic information so that possible corrosion problems in different coal-conversion processes can be evaluated.

1. Uniaxial Tensile Properties

The experimental program that involves generation of uniaxial tensile data on four selected alloys upon exposure to the multicomponent gas environments has been discussed in detail in an earlier report.[5] Results of initial corrosion experiments on specimens of Type 310 stainless steel, Incoloy 800, Inconel 671, and U. S. Steel Alloy 18-18-2 in the selected gas mixtures were reported in the last quarterly report.[6] Uniaxial tensile specimens of the four alloys were fabricated according to ASTM Standard E8-69. The specimens had a gauge length of 20.3 mm, a width of 5.1 mm, and a thickness of 2.54 mm. The specimens were loaded by means of pins that pass through holes in the enlarged end sections to minimize misalignment. The total elongation was measured between small indentations made on the specimen surface prior to testing. The specimens were tensile tested in an Instron machine at a crosshead speed of 8.33×10^{-3} mm s^{-1}. This speed corresponds to the initial strain rate of 4.1×10^{-4} s^{-1} for the 20.3-mm gauge-length specimens. All tests were conducted in vacuum, and the test temperatures were maintained within ±2°C.

During the present quarter, tensile tests were conducted on the four alloys in the as-received condition at temperatures of 750, 871, and 982°C. Figure 29 shows several specimens of the different alloys before and after tensile testing at various temperatures. The load-elongation data from the tensile tests were converted to true stress-true strain curves by assuming a constant volume approximation. Figures 30-33 show the true stress-true strain curves for Incoloy 800, Type 310 stainless steel, U. S. Steel Alloy 18-18-2, and Inconel 671, respectively, at the three test temperatures. It is evident that the flow stress at a given strain tends to decrease with an increase in test temperature. The effect of test temperature on the true strain values is minimal for Incoloy 800 and U. S. Steel Alloy 18-18-2. However, an increase in test temperature from 750 to 982°C results in significant increases in true strain values for Type 310 stainless steel and Inconel 671.

The load-elongation data obtained from different tests were also used to evaluate the engineering tensile properties (0.2% yield stress, ultimate tensile strength, uniform strain, and total elongation) for the four alloys, and the results are listed in Table IX. It should be noted that the uniform strain values obtained on all specimens were considerably smaller than the total elongation values. During the next quarter, specimens of the four alloys will be tensile tested after exposure for 1000 h to selected multicomponent gas mixtures.

2. Thermodynamics of Multicomponent Gas Mixtures

During the present quarter, a generalized approach, based on thermodynamic equilibria of gas mixtures, has been developed to evaluate the chemical potentials of the reactive elements, i.e., O, S, C, H, and N in multicomponent gas streams over a wide range of gas compositions, pressures, and temperatures.[12]

Studies of the kinetics and the mechanism of the reaction between multicomponent gases and condensed phases require that the chemical potential of different reactive elements be established before their interactions with the alloys can be considered. In binary and some ternary gas mixtures, the chemical potentials can be readily established as a function of temperature, based on the room-temperature gas composition and free-energy data for the reactions. For example, at any temperature, the partial pressure of S_2 can be determined from the H_2/H_2S pressure ratio, the partial pressure of O_2 can be obtained from H_2/H_2O, CO/CO_2, or SO_2/SO_3 ratios, and the carbon activity a_c can be established by the CH_4/H_2 ratio in the gas mixture. In multicomponent gas mixtures, the reaction kinetics are complex, since reaction equilibria between several gas species must be considered.

For this purpose, a computer program[13] was developed by which equilibrium partial pressures of various gas species could be evaluated at elevated temperatures for a given room-temperature composition. For a gas system that consists of CO, CO_2, H_2, H_2O, H_2S, and N_2 or NH_3, several gas equilibria were used to formulate a set of nonlinear algebraic equations. Solutions were obtained that satisfy the conservation of the different reactive elements (i.e., C, H, S, O, and N) and the total pressure of the gas mixture. The results of the analysis were used to establish the elevated-temperature gas compositions, partial pressures p_{O_2}, p_{S_2} and p_{N_2}, and carbon activity a_c in the gas mixture.

3. Chemical Potentials of Carbon and Oxygen

The values of a_c and p_{O_2} at 1148 K and 1-atm pressure are shown in Figs. 34a and 34b, respectively, as a function of the volume ratio of CH_4/H_2 for different CO/CO_2 ratios in the room-temperature gas composition. The amount of H_2S and NH_3 in the mixture was <1%. Figure 34 shows that, for a gas mixture without H_2O, the values of a_c and p_{O_2} are influenced by both the CH_4/H_2 and CO/CO_2 ratios; however, the effect decreases when the CH_4/H_2 ratio is <0.001. The carbon activity reaches a value of unity in gas mixtures that contain CO/CO_2 >7.0 and CH_4/H_2 >0.05. This is reflected in the values of p_{O_2} by a break in the curves shown in Fig. 34b, which is due to deposition of soot from the gas mixture.

Additions of H_2O to the gas mixture increase the value of p_{O_2} and decrease the value of a_c. The change is appreciable when the CH_4/H_2 ratio in the gas is <0.01. In fact, for this condition, the influence of the CO/CO_2 ratio on a_c and p_{O_2} is completely masked by the presence of H_2O.

The values of a_c and p_{O_2} can be estimated from Fig. 34 for a wide range of CO/CO_2 ratios and for different amounts of H_2O content in the gas mixture. Figure 34 can be modified by plotting a_c and p_{O_2} as a function

of the atomic ratio C/H for different ratios of C/O in the room-temperature gas composition. These curves are shown in Figs. 35a and 35b. Unique values of a_c and p_{O_2} are obtained for a given set of C/H and C/O values irrespective of the individual amounts of the various gases in the mixture. If the H_2S and NH_3 contents in the gas are increased to 10 vol %, a change of <3% would result in the values of a_c and p_{O_2}. The curves shown in Fig. 35 were used to plot isopotential lines for C and O as a function of the C/H and C/O ratios. This figure reflects several characteristics of the reaction equilibria in multicomponent gas mixtures at elevated temperatures. The most prominent feature is the shape of the isoactivity lines for carbon. The knee in the isoactivity lines indicates a transition in the reaction that controls the carbon activity in the gas mixtures. Above the knee, the isoactivity lines are relatively insensitive to the C/H ratio, which indicates that the value of a_c is controlled primarily by the CO-CO_2 reaction. Below the knee, a_c is established by the CH_4-H_2 reaction, and the isoactivity lines are insensitive to variations in the C/O ratio. The knee is the transition region in which both reactions are effective.

The partial pressure of oxygen is established basically by the amount of O in the mixture, except in the region where $a_c = 1$ (upper right corner of the diagrams). In this region, the amount of C in the gas phase changes continuously as a result of the deposition of soot. The knee in the isoactivity lines occurs at a p_{O_2} value of 1×10^{-20} atm at 1148 K. It should be pointed out that, since the $2CO \rightarrow CO_2 + C$ and $CH_4 \rightarrow 2H_2 + C$ reactions are promoted and retarded, respectively, by an increase in pressure, the effect of pressure on chemical potentials in gas mixtures which correspond to regions above and below the knee will be different. This effect will be discussed in greater detail in the next section.

The points shown in Fig. 36 correspond to the gas compositions anticipated in various coal-gasification processes.[14] These processes lie in the region above the knee. The range of interest for the C/H and C/O ratios is from 0.1 and 0.4 and 0.35 to 0.75, respectively.

4. Chemical Potential of Sulfur

The variation in the partial pressure of S_2 which changes in the room-temperature gas composition is more complex. In addition to the C/H and C/O ratios, the value of p_{S_2} also depends upon the atomic ratio C/S in the gas mixture. Figure 37 shows the plots of p_{S_2} as a function of C/S for different C/O values at 1148 K. The figure shows that, for gas compositions with C/H <0.05, the effect of oxygen on the value of p_{S_2} is negligible. Under these conditions, p_{S_2} is controlled by the H_2S-H_2 reaction.

In the region of interest for coal-gasification processes, namely, C/H = 0.1 to 0.4, an increase in O in the gas mixture decreases the partial pressure of S. For these gas compositions, the SO_2 and SO_3 reactions also influence the values of p_{S_2}. For a gas composition with C/H = 0.4 and C/S = 300 at 1148 K, the value of p_{S_2} decreases from 10^{-7} to 10^{-8} atm when C/O increases from 0.4 to 0.8. The corresponding change in p_{O_2} is considerably greater, from 10^{-16} to 5×10^{-19} atm. On the other hand, an order of magnitude change in S in the gas mixture changes p_{S_2} by two orders of magnitude without changing the value of p_{O_2}. The effect of variations in gas composition on the chemical potentials is considered in the next section.

5. Effect of Variation in Gas Composition

The room-temperature gas composition anticipated in various coal-gasification processes varies over a wide range, depending on the type of process, the temperature of operation, and feedstock composition. It is important to consider the influence of individual constituents of the gas mixture on the chemical potentials of C, O, and S. The gas composition in the Synthane process for conversion of coal into high-Btu gas is plotted as point H in the 1273 K isopotential diagrams shown in Figs. 38a and 38b. Points A and B correspond to different values of H_2O content, and points C and D represent a change in the CH_4 content in the gaseous environment. The compositions of these gas mixtures are listed in Table X.

Figure 38a shows that, when the amount of H_2O changes from 45 to 25% (i.e., points A and B, respectively) without changing the relative amounts of other gas species, the value of p_{O_2} decreases from approximately 3×10^{-15} to 7×10^{-16} atm and a_c increases from 0.003 to 0.008. Similarly, a change in the CH_4 content from 4 to 20 vol %, i.e., points C and D, respectively,* decreases p_{O_2} from $\sim 5 \times 10^{-15}$ to 4×10^{-16} atm and increases a_c from 0.002 to 0.01.

The values of p_{S_2} can be estimated from Fig. 38b. Compositions A and C correspond to the isopotential curves for C/O = 0.4, and compositions B and D correspond to the curves for C/O = 0.6. Figure 38b shows that the variation of p_{S_2} with H_2O content in the gas mixture is insignificant. However, when the CH_4 content increases from 4 to 20 vol %, p_{S_2} decreases from $\sim 8 \times 10^{-8}$ to 1×10^{-8} atm.

A variation in the H_2 content in the gas mixture corresponds to a vertical shift of point H on the isopotential diagrams. Such a change results in similar changes in the partial pressures of S_2 and O_2. For example, when the ratio C/H increases by a factor of three, the values of p_{S_2} and p_{O_2} increase by a factor of nine.

Any change in the amount of H_2S in the gas mixture results in a change in the partial pressure of S alone. When H_2S increases from 0.1 to 1.0%, i.e., points H and H' in Fig. 38b, the value of p_{S_2} increases by two orders of magnitude without affecting the values of p_{O_2} and a_c.

6. Effect of Pressure

As was mentioned previously, the total pressure can influence the chemical potentials of C, O, and S via various gas reactions. The carbon activity in the gas mixture can either decrease or increase with an increase in pressure, depending on whether the CH_4-H_2 or the CO-CO_2 reaction establishes the carbon activity in the environment. Figure 39 shows the variation in a_c with pressure at 1148 K. The values of p_{O_2} and p_{S_2} shown in these figures represent the partial pressures of O_2 and S_2 in the gas mixture at a total pressure of 1 atm. Figure 39 shows the variation in carbon activity for a

*Conditions C and D on the isopotential diagrams can also be achieved by changing the relative amounts of CO and CO_2 in the gas mixture.

wide range of room-temperature gas compositions. For gas mixtures that lie below the knee in the isopotential diagram, i.e., $p_{O_2} \lesssim 10^{-20}$ atm, a_c decreases with an increase in pressure, however, for those above the knee, a_c increases with an increase in pressure. For example, a_c increases by a factor of 20 at 1148 K as the pressure increases from 1 to 100 atm. No significant change occurred in the values of a_c with variations in sulfur content of the gas mixture. The curves shown in Fig. 39 represent gas mixtures with $p_{S_2} = 10^{-7}$ atm. A change of <3% would result in the value of a_c when the H_2S concentration in the gas mixture changes by a factor of 10.

The effect of total pressure on the partial pressure of O_2 depends upon the values of a_c and p_{O_2} in the gas mixture at 1 atm. The variation in p_{O_2} with pressure is shown in Fig. 40 at 1148 K. In general, p_{O_2} increases with an increase in pressure, and the nature of the variation is different for various gas compositions. As seen in Fig. 40 for $p_{O_2} < 10^{-20}$ atm in the gas mixture at 1 atm, the total pressure in the range of from 1 to 10 atm influences the p_{O_2} and has virtually no effect at higher pressures. On the other hand, in the case of more oxidizing atmospheres ($p_{O_2} \geq 10^{-19}$ atm), p_{O_2} is independent of total pressure between 1 and 10 atm but increases rapidly at higher total pressures.

The increase in the partial pressure of S_2 with an increase in total pressure is similar to that observed for the partial pressure of oxygen. Figure 41 shows the variation in p_{S_2} with total pressure for three temperatures. In all cases, p_{S_2} was $\simeq 10^{-7}$ atm at a total pressure of 1 atm. Figure 41 shows that the influence of pressure on the values of p_{S_2} is stronger at pressures >10 atm, but the increase in p_{S_2} is smaller at higher temperatures. Even when the gas compositions were modified to yield $p_{S_2} = 10^{-5}$ or 10^{-9} atm, the effect of pressure was identical to that shown in Fig. 41.

7. Effect of N_2 Additions

In the agglomerated-ash and Consol CO_2-Acceptor processes for production of high-Btu gas, the environment in the regenerator section of the system contains 60 to 75 vol % N_2. Even for these gas mixtures, the chemical potentials of C, O, and S can be obtained from the isopotential diagrams shown in Figs. 36 and 37. The influence of pressure on the partial pressures of the reactive elements can then be estimated from Figs. 39-41. The only difference is that the partial pressures of O_2 and S_2 and the carbon activity at 1-atm pressure in a gas mixture containing 60 vol % N_2 will correspond to the values at 0.4 atm. In other words, N_2 is relatively inert in these multicomponent gas mixtures. The equilibrium constant for the N_2-NH_3 reaction is small in the temperature range of interest for coal-conversion processes. However, this reaction is quite sensitive to pressure, and the effect of N_2-NH_3 reaction on the values of p_{O_2}, p_{S_2}, and a_c are appreciable at pressures >40 atm.

The approach and the results presented thus far on the thermodynamic equilibria in multicomponent gas mixtures show that the chemical potentials of the reactive elements, i.e., O, S, C, H, and N, can be unequivocally established from the room-temperature gas composition, with total atomic ratios

of C/O, C/H, and C/S as parameters. The analysis can aid in the understanding of material behavior upon exposure to complex gas mixtures and also enable rational comparisons of corrosion data obtained by different investigators. The approach has been used extensively at Argonne National Laboratory to develop information on high-temperature corrosion and mechanical behavior of materials for application in coal-conversion systems.

TABLE IX. Tensile Properties of Four Selected Alloys in the As-received Condition

Alloy	Temperature, °C	0.2% Yield Stress, MPa	Ultimate Tensile Strength, MPa	Uniform Strain, %	Total Elongation, %
Incoloy 800	750	91.0	226.7	4	136
	871	30.7	119.7	4	123
	982	29.7	59.8	11	121
Type 310 Stainless Steel	750	49.2	257.9	4	38
	871	43.0	138.5	3	48
	982	25.4	55.0	15	78
U. S. Steel Alloy 18-18-2	750	63.5	191.2	8	70
	871	56.8	94.5	3	71
	982	31.5	52.0	2	68
Inconel 671	750	49.2	339.0	9	32
	871	42.0	141.1	5	87
	982	22.4	50.7	4	234

TABLE X. Compositions (Vol %) of the Gas Mixtures Shown in Fig. 38

Parameters	H	A	B	C	D
H_2	19.0	16.3	22.3	20.7	17.3
CO	9.0	7.7	10.6	9.8	8.2
CO_2	21.0	18.1	24.6	22.9	19.1
CH_4	12.0	10.3	10.1	4.0	20.0
H_2O	36.0	45.0	25.0	39.3	32.7
H_2S	0.1	0.086	0.117	0.109	0.091
NH_3	1.0	0.86	1.17	1.09	0.91

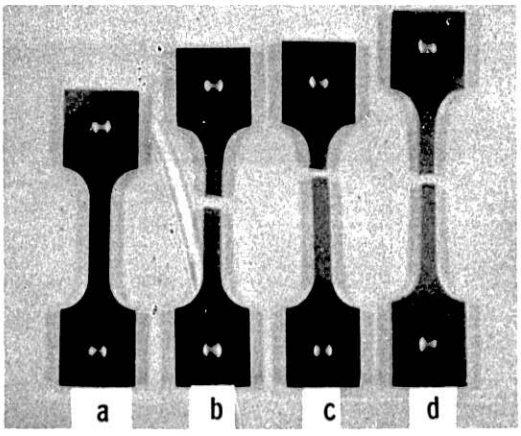

TYPE 310 SS

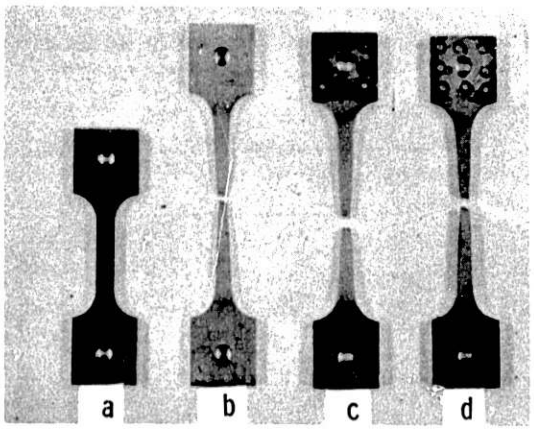

INCOLOY 800

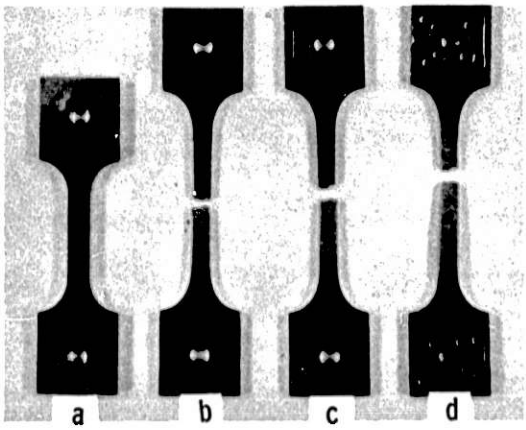

U.S. STEEL ALLOY 18-18-2

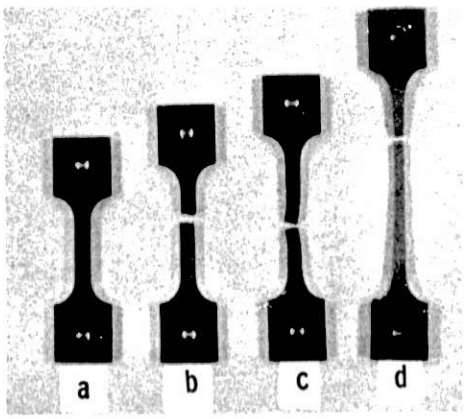

INCONEL 671

Fig. 29. Tensile Specimens of Different Alloys before Testing (a) and after Testing at 750°C (b), 871°C (c), and 982°C (d). ANL Neg. No. 306-77-384.

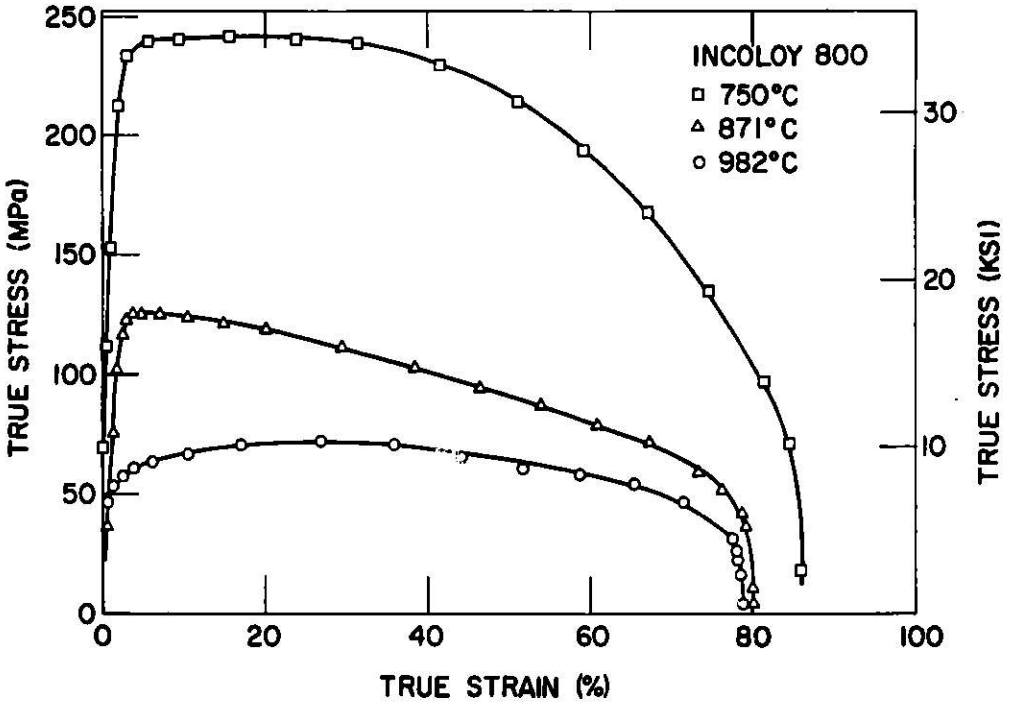

Fig. 30. True Stress-True Strain Curves for Incoloy 800 in the As-received Condition at 750, 871, and 982°C. ANL Neg. No. 306-77-376.

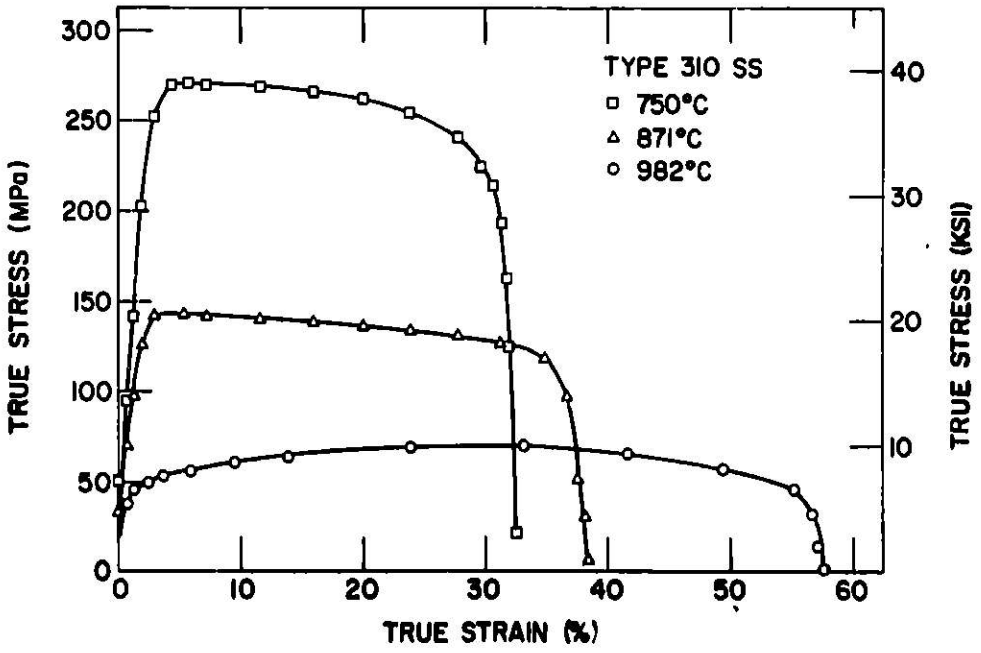

Fig. 31. True Stress-True Strain Curves for Type 310 Stainless Steel in the As-received Condition at 750, 871, and 982°C. ANL Neg. No. 306-77-380.

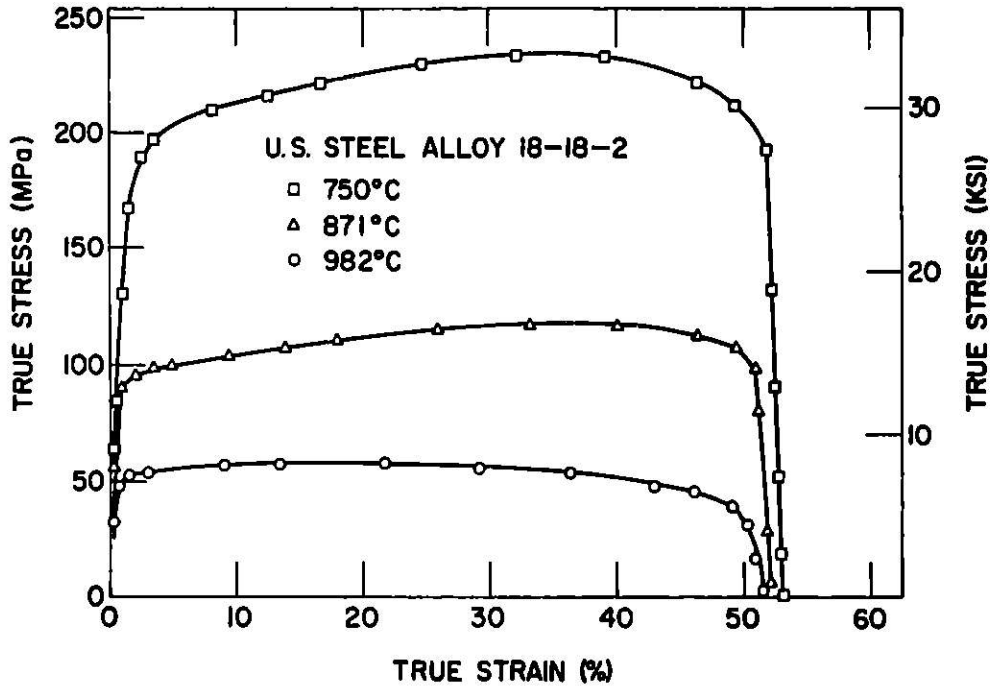

Fig. 32. True Stress-True Strain Curves for U. S. Steel Alloy 18-18-2 in the As-received Condition at 750, 871, and 982°C. ANL Neg. No. 306-77-377.

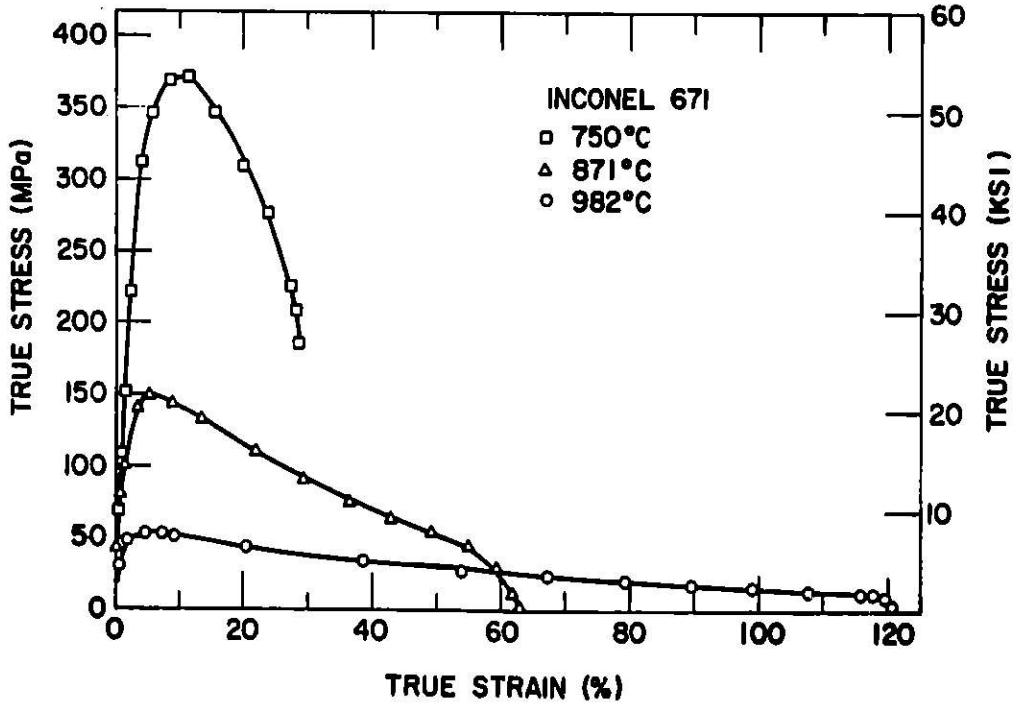

Fig. 33. True Stress-True Strain Curves for Inconel 671 in the As-received Condition at 750, 871, and 982°C. ANL Neg. No. 306-77-378.

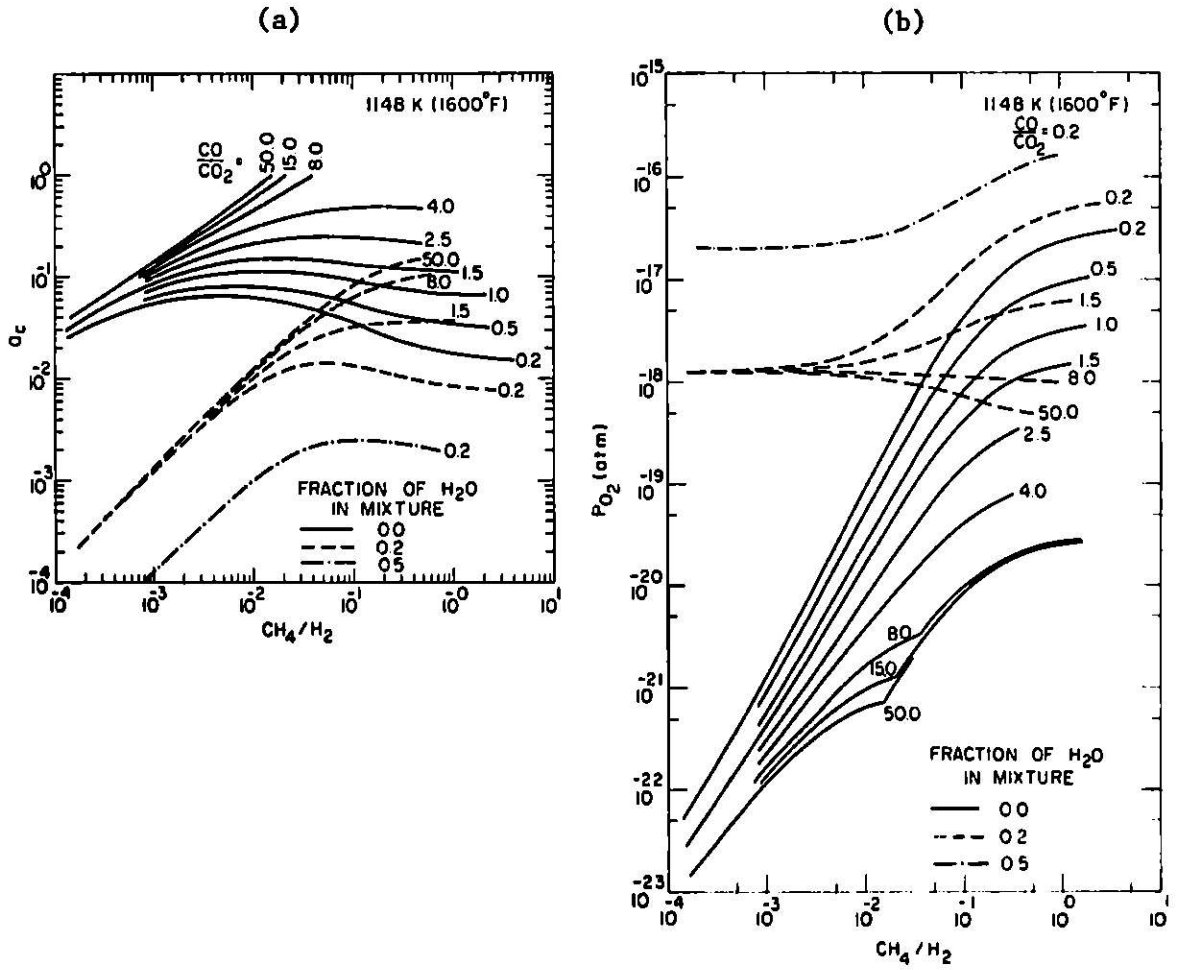

Fig. 34. The Variation in Chemical Potentials of (a) Carbon and (b) Oxygen at 1148 K and 1-atm Total Pressure as a Function of the Volume Ratio of CH_4/H_2 for Different CO/CO_2 Ratios and Volume Fractions of H_2O in the Room-temperature Gas Composition. ANL Neg. No. 306-77-286.

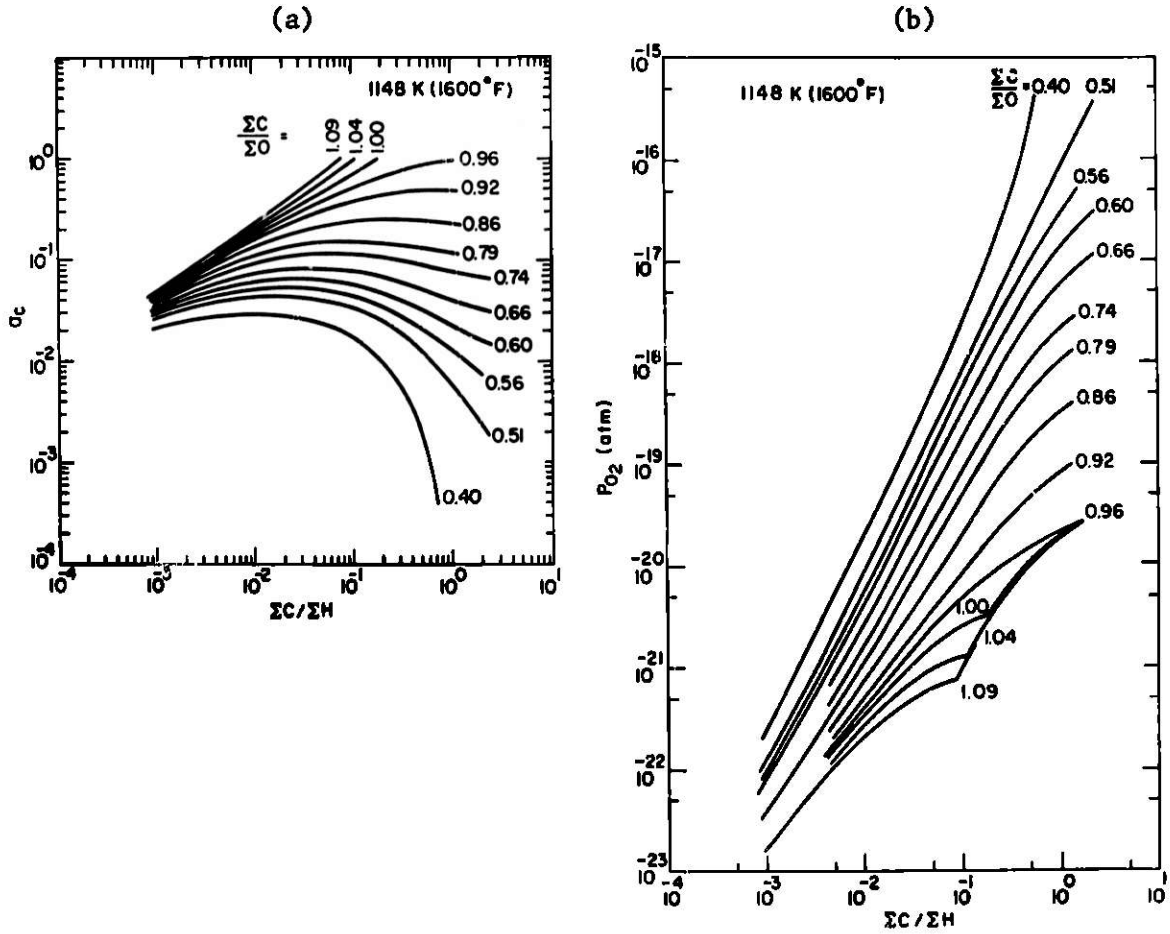

Fig. 35. The Variation in Chemical Potentials of (a) Carbon and (b) Oxygen at 1148 K and 1-atm Total Pressure as a Function of the Atomic Ratio C/H for Different C/O Ratios in the Room-temperature Gas Composition. ANL Neg. No. 306-77-292.

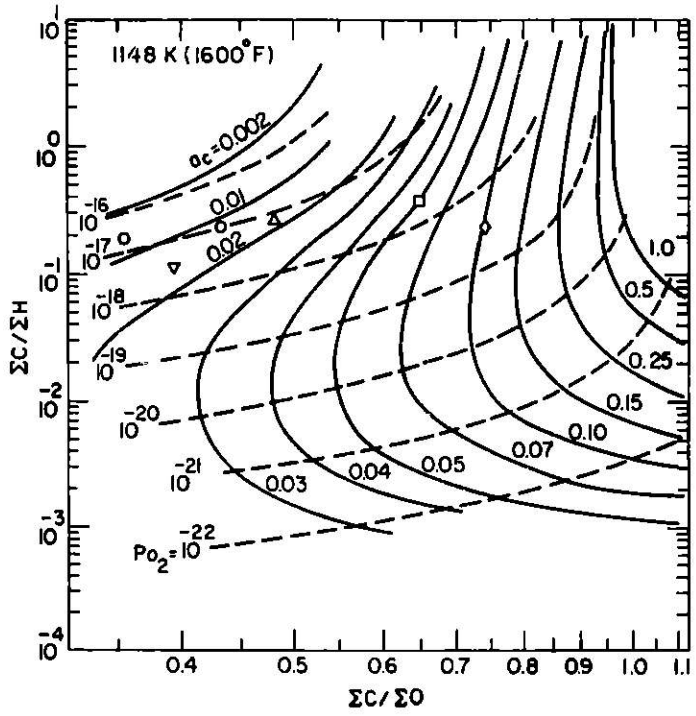

Fig. 36. Plots of the Isopotential Lines for a_c and p_{O_2} as a Function of C/H and C/O Ratios at 1148 K. The symbols represent gas compositions of the various coal-gasification processes. ANL Neg. No. 306-77-379.

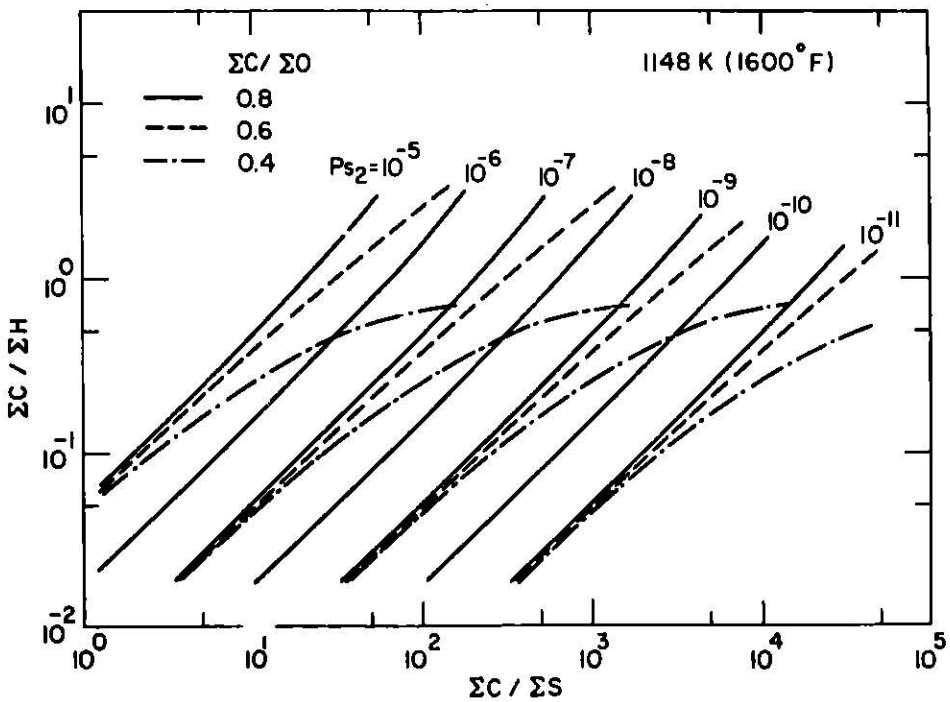

Fig. 37. Plots of the Isopotential Lines for p_{S_2} as a Function of C/H, C/S, and C/O Ratios at 1148 K. The symbols represent gas compositions of the various coal-gasification processes. ANL Neg. No. 306-77-375.

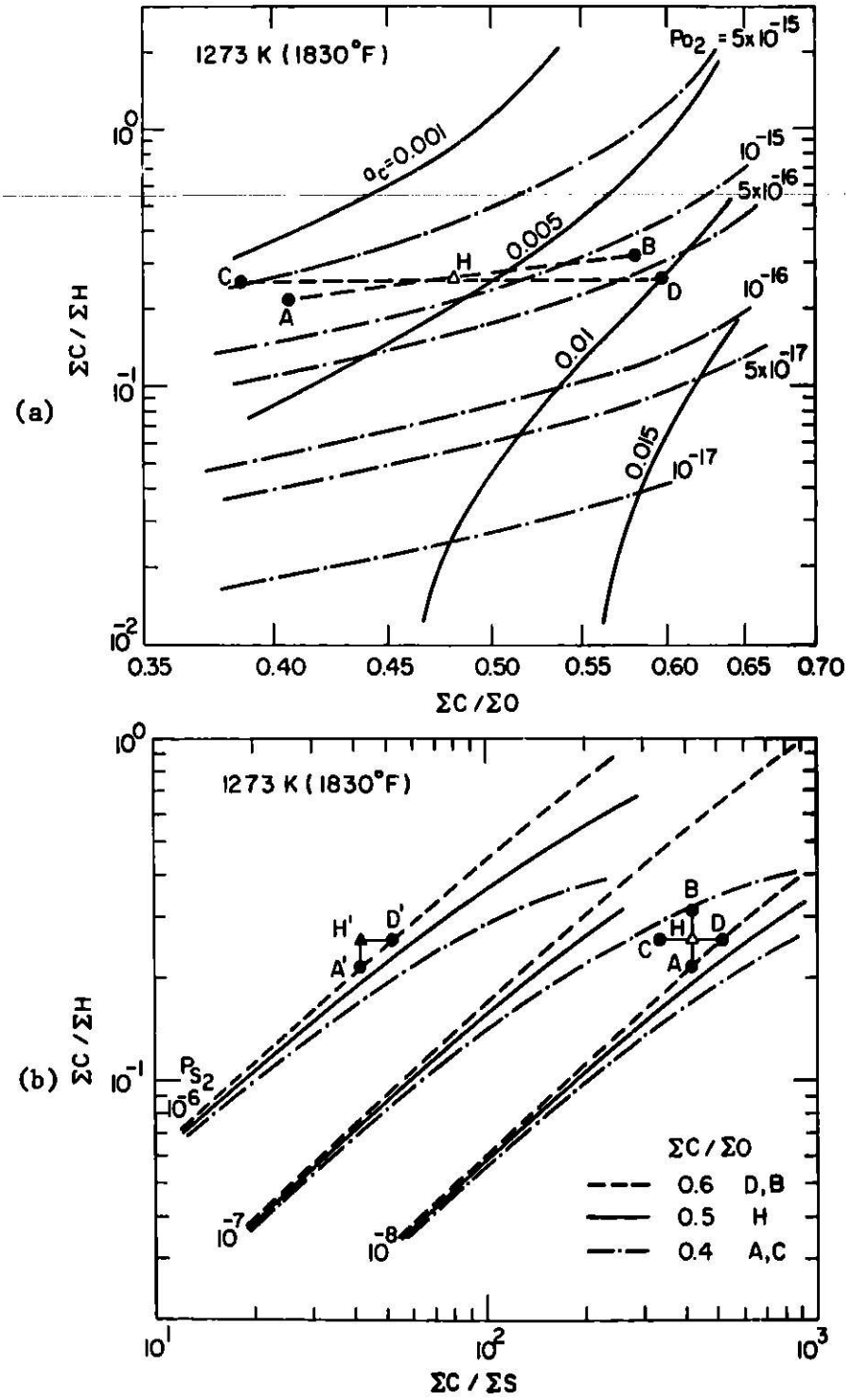

Fig. 38. Isopotential Diagrams at 1273 K Showing the Effect of Variations in the Contents of Different Constituents of the Gas Mixture on the Chemical Potentials of C, O, and S. (a) Isopotential lines for a_c and p_{O_2} and (b) isopotential lines for p_{S_2}. ANL Neg. No. 306-77-288.

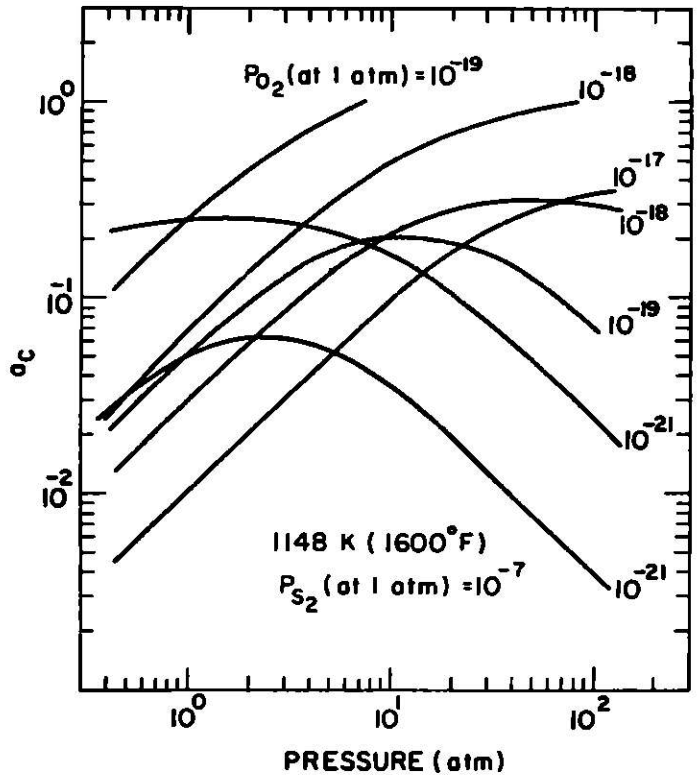

Fig. 39. The Variation in a_c with Total Pressure P at 1148 K. ANL Neg. No. 306-77-371.

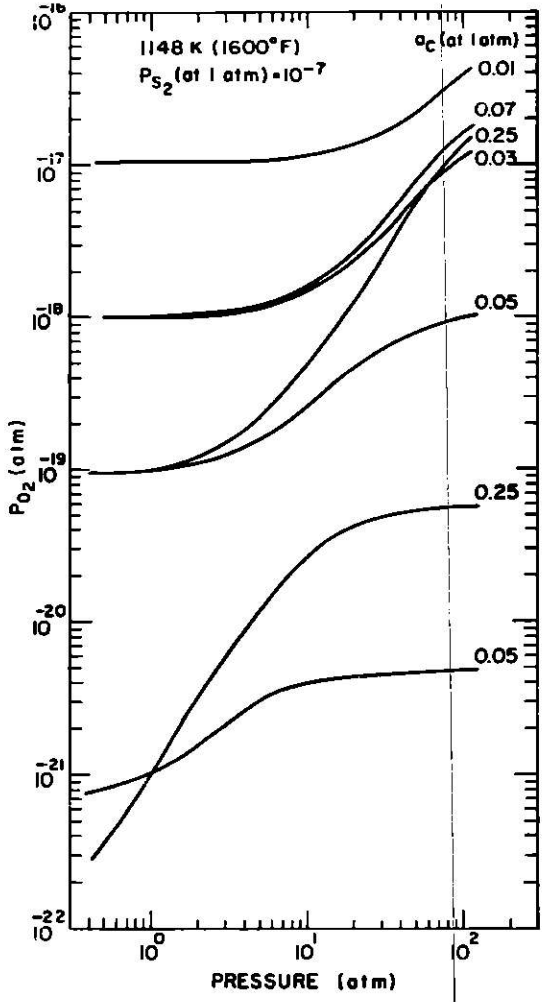

Fig. 40. The Variation in p_{O_2} with Total Pressure P at 1148 K. ANL Neg. No. 306-77-290.

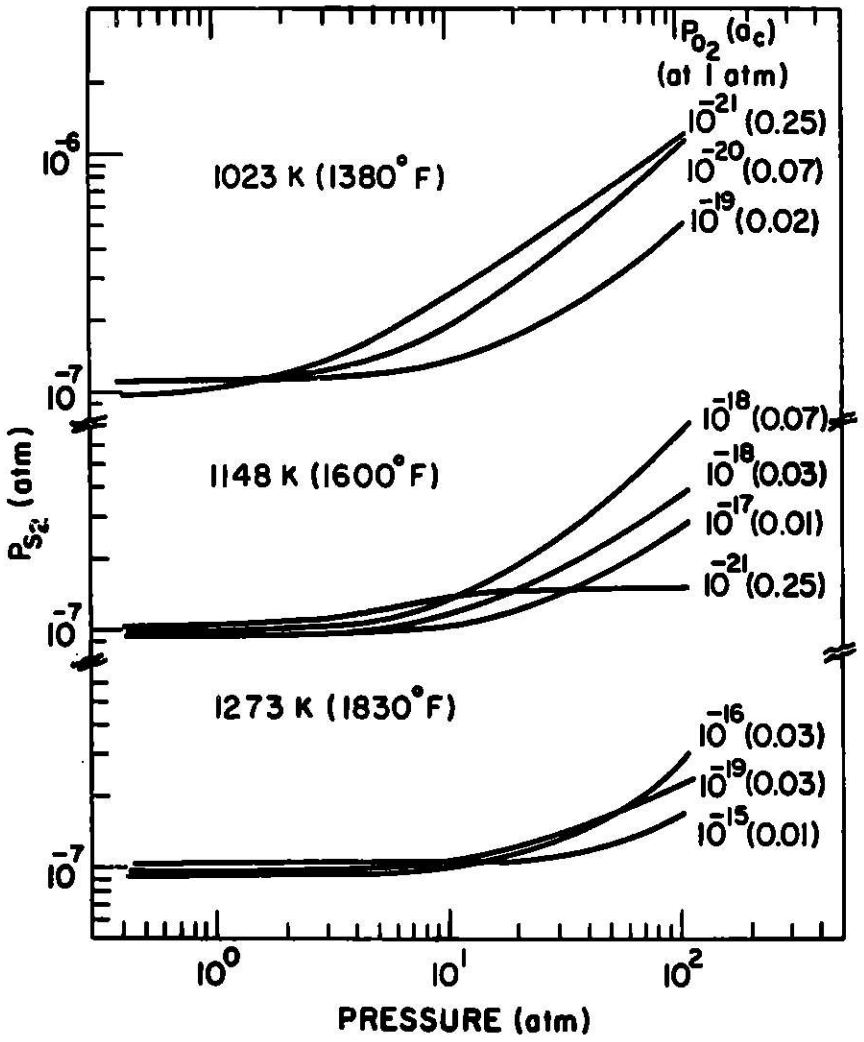

Fig. 41. The Variation in p_{S_2} with Total Pressure P. ANL Neg. No. 306-77-287.

MILESTONE CHART

FY 1977

Task D -- Corrosion Behavior of Materials for Coal-conversion Processes

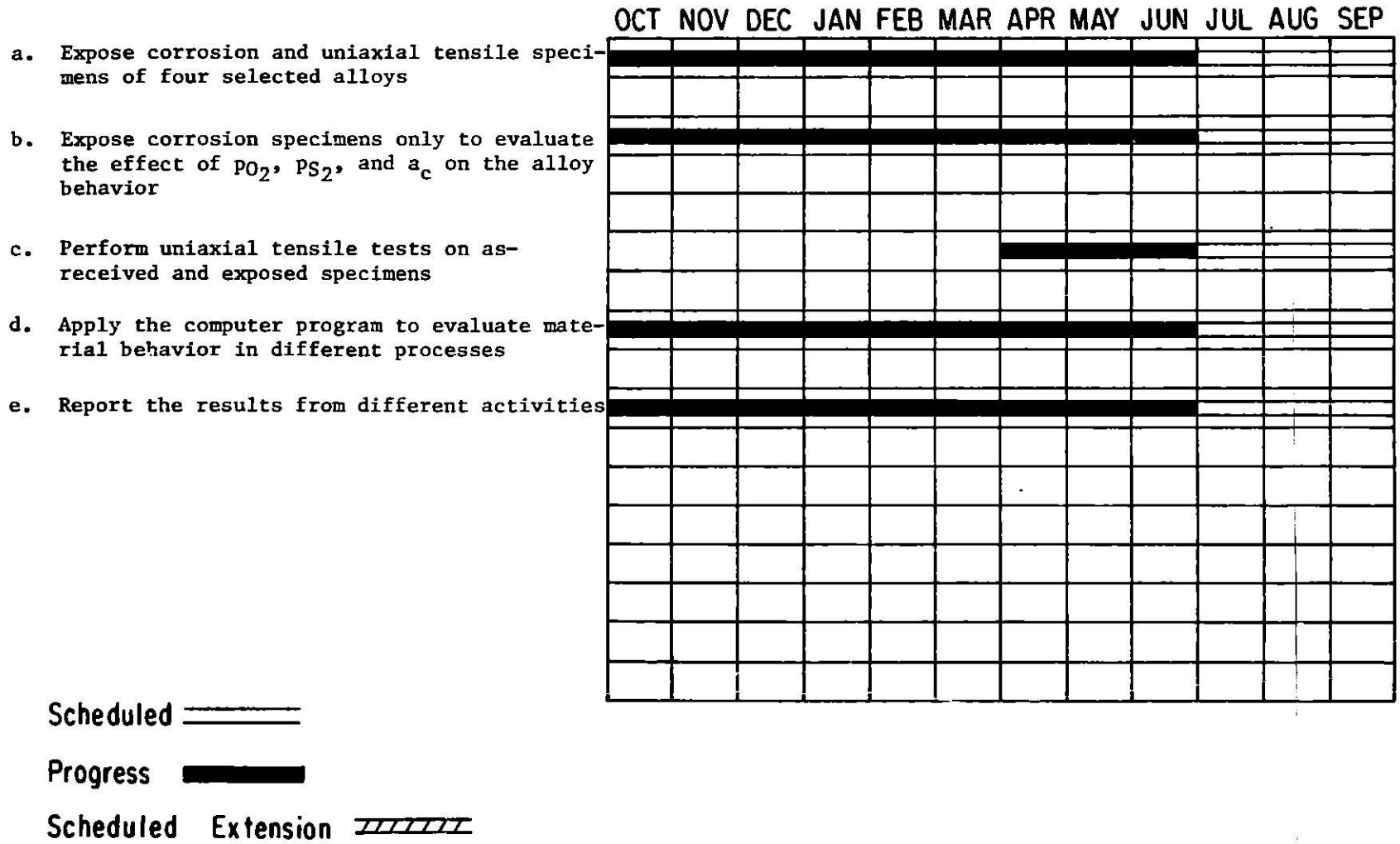

Task E -- Erosion Behavior of Materials in Coal-conversion Processes
(W. J. Shack and J. Y. Park)

During the present quarter, a work plan was developed for the experimental phase of the erosion task. The main objective of this phase will be to obtain engineering design data on erosion for various candidate materials. The laboratory erosion tests will be performed at temperatures and in atmospheres designed to simulate actual plant conditions, and the results will be bench marked against data obtained from the ongoing in-situ field measurements being made in the nondestructive testing task. To develop reliable quantitative estimates of the erosive-wear rate, careful control of important test variables such as temperature, particle velocity, impact angle, and environment will be maintained. This should facilitate comparison of the results with analytical models of the erosion process.

To perform the tests, a specially designed erosion test apparatus was developed by Solar under a subcontract from ANL. The apparatus consists of a motor-driven rotating "slinger" that propels erosive particles radially outward to strike test specimen targets mounted in a circle around the slinger. Erosive particles are delivered to the slinger at a controlled rate by a motor-driven belt feed mechanism. The feed mechanism and slinger assemblies are enclosed in a test chamber that permits operation at elevated temperatures under controlled gaseous environments. The test environment is controlled by an external system of bottled gases, manifolds, mixers, and preheaters. A schematic of the apparatus is shown in Fig. 42.

The materials and environmental conditions for the testing fall into two groups. The first group includes materials and conditions characteristic of coal-feed systems. In this case, the erosive material is coal, in which the temperatures are fairly low (~93°C) and the environments are fairly benign (typically slurries mixed with water or gases such as CO_2 or N_2). Typical components include feed lines, valves, slurry pumps, etc. Candidate materials for such components include A106 low-carbon steel, Types 304 and 310 stainless steel, and Stellite 6B and tungsten carbide (as hard-facing materials).

In the second group, the materials and conditions would be characteristic of the off-gas lines, ash-removal systems, gasifier internals, cyclones, etc. The temperatures involved are much higher (~760-982°C), and the atmosphere is much more complex and active. Although refractory materials will be widely used in such applications, only metals and ceramic-coated specimens will be considered here to avoid unnecessary duplication of the work at the National Bureau of Standards. Candidate metals for such applications will include Types 304 and 310 stainless steel, Incoloy 800, Inconel 671, and Stellite and tungsten carbide hard facings. The erosive materials will be primarily coal char. In both cases, the velocities of the erosive particles will be quite low; tests are planned for velocities of 30 and 9 m/s (100 and 30 ft/s, respectively).

To check and calibrate the erosion-testing apparatus, a sequence of short-term (<24 h) tests will be carried out using aluminum oxide particles as the erosive material to obtain accelerated wear. Although the

primary purpose of this sequence of tests will be calibration of the erosion apparatus, the results will give a preliminary ranking of the candidate materials in terms of their resistance to erosive wear. After the apparatus has been calibrated, longer-term tests using coal and coal char as the erosive materials will be performed in appropriate test environments. The initial test duration will be 100 h. This will be followed by a longer-term 500-h test. The test matrix for the program is shown in Table XI. A projected schedule for the test program is shown in Table XII.

TABLE XI. Test Matrix.

(1) Calibration and Screening Test[a]

Material	Erosive Particle Al_2O_3		Particle Velocity		Temperature	
	100 μm	50 μm	30 m/s	9 m/s	982°C	93°C
A106	X	X	X	X		X
Type 304 SS	X	X	X	X	X	X
Type 310 SS	X	X	X	X	X	X
Incoloy 800	X	X	X	X	X	
Inconel 671	X	X	X	X	X	
Stellite 6B	X	X	X	X	X	X
WC	X	X	X	X	X	X

[a]Each test period is <24 h.

(2) Short-term (100-h) and Long-term (500-h) Tests

Material	Erosive Particle Temperature		Particle Velocity		Test Period	
	982°C Coal Char	93°C Coal	30 m/s	9 m/s	100 h	500 h
A106		X	X	X	X	X
Type 304 SS	X	X	X	X	X	X
Type 310 SS	X	X	X	X	X	X
Incoloy 800	X		X	X	X	X
Inconel 671	X	X	X	X	X	X
Stellite 6B	X	X	X	X	X	X
WC	X	X	X	X	X	X

TABLE XII. Projected Schedule for Test Program

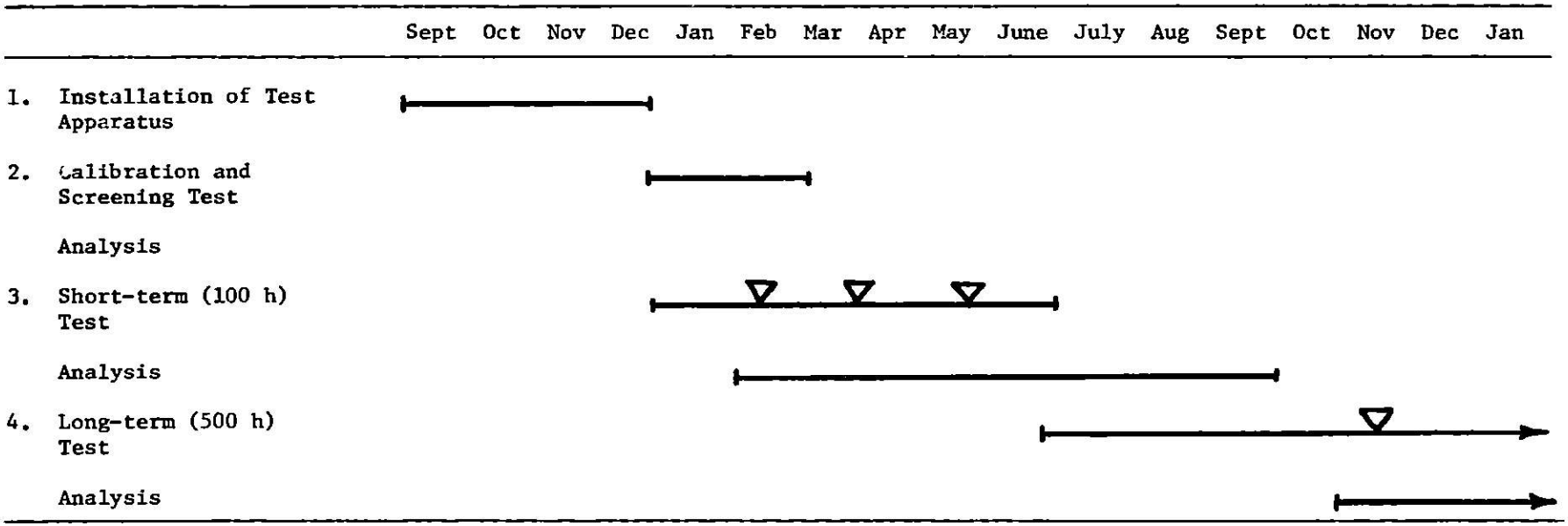

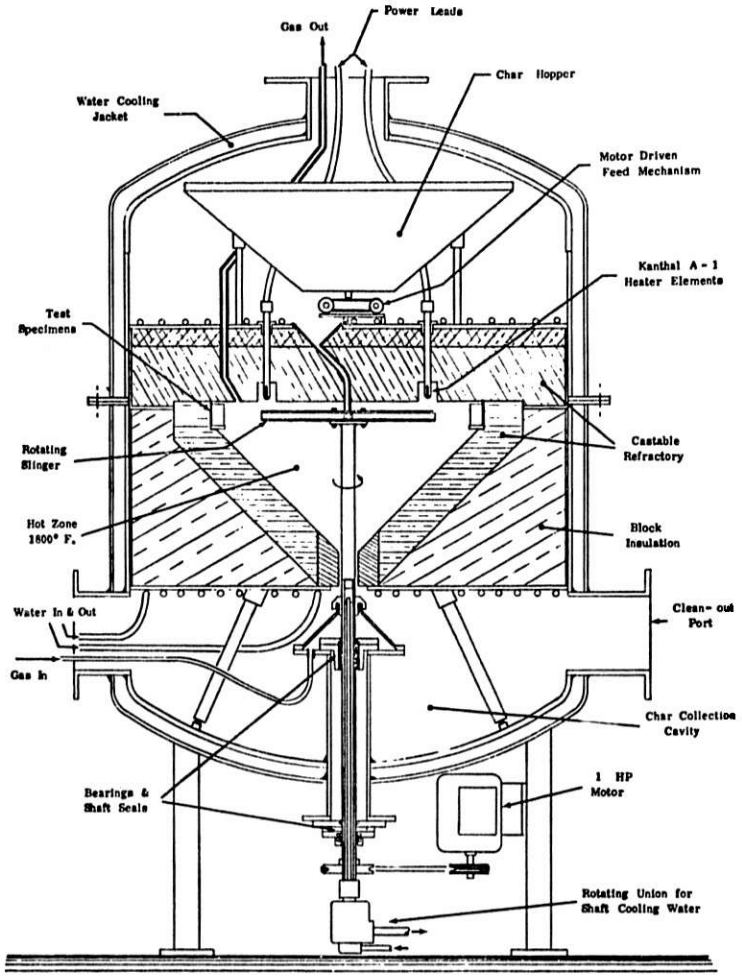

Fig. 42. Erosion-Corrosion Test Chamber for Coal-gas Environment. Neg. No. MSD-63876.

MILESTONE CHART

FY 1977

Task E -- Erosion Behavior of Materials in Coal-conversion Processes

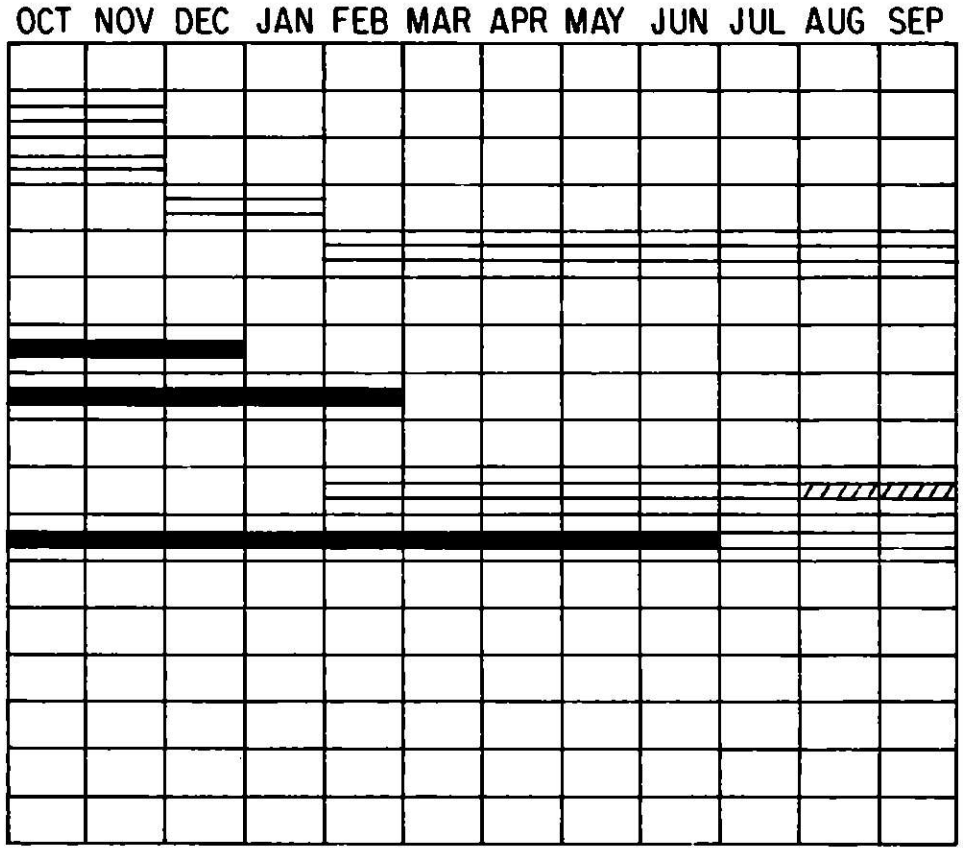

Experimental Phase*

a. Select materials for testing

b. Set up and calibrate apparatus

c. Short-term tests

d. Long-term tests

Modeling Phase

a. Literature survey of two-phase flow

b. Comparison of current analytical models with available data

c. Refinement of current analytical models

d. Development of computer analyses of two-phase flows

*No progress has been possible in this phase because of delays in obtaining the rotating slinger erosion apparatus

Scheduled

Progress

Scheduled Extension

Task F -- Component Performance and Failure Analysis *(S. Danyluk and G. M. Dragel)*

The activity during the present quarter involved the examination of four components from the Synthane plant (ballooned pipe, pump impeller shaft, thermowell and purge line) and thermowells from the Battelle Char-Burner. The status of these investigations is reported below. In addition, a field trip was made to Synthane and ERDA headquarters, Washington, D.C., to consult on cracks discovered in Incoloy 800 nozzles from the gasifier vessel. ANL laboratory investigations have not begun on the nozzles.

1. Ballooned Pipe from the Synthane Pilot Plant

Preliminary data on this failure has been reported previously.[6] The following additional data has been collected.

(a) Hardness numbers were obtained from several positions on the pipe. The average reading was ∿200 kg/mm^2 Vickers hardness, which is within the specification for this material.

(b) A comparison of the actual chemical analysis with the ASTM standard A 335-74a showed the the material is grade P21 and not P1 as specified by the plant. Grade P1 does not contain chromium. However, since the mechanical properties of both grades are similar, ballooning is not expected to be due to the difference in grade.

(c) A creep rate calculation was carried out using elevated-temperature properties of chromium-molybdenum steels,[15] and it was found that, assuming 510°C (950°F), the creep rate would be ∿2 x 10^{-10} %/s (∿8 x 10^{-7} %/h) at 68 MPa (10,000 psi). Since this is a low rate, we do not expect creep to be the dominant deformation mechanism.

(d) Tensile specimens were machined from the ballooned pipe, and a tensile test was carried out to verify the yield strength. A value of σ_y = 324 MPa (47 ksi) was obtained, which is within the specification for the material.

(e) Optical metallography showed some "porosity" through the cross section of the ballooned area. Scanning-electron microscopy confirmed the "porosity," and it was observed that the pores were correlated somewhat with the grain boundaries. The cause of the "porosity" is not known.

The cause of the ballooning has not been identified. The ballooned pipe was replaced and no problems have been encountered. The investigation of this failure is terminated.

2. Synthane Impeller-shaft Failure

A 3.17-cm (1.25-in.) impeller shaft and screwcap from pump GA-207 failed by complete separation (Fig. 43). The shaft material is 4140 steel and

the screwcap is a Type 4037 steel. The original shaft and screwcap failed after 1.8-2.9 Ms (∿500-800 h) of operation and a replacement screwcap failed after 18 ks (∿5 h) of operation. The pump circulates 1.5 x 10^{-2} m^3/s (230 gpm) Venturi scrubber recycle water containing carbon fines with a suction pressure of 4.1 MPa (600 psig) and a discharge pressure of 5.2 MPa (750 psig) at a temperature of 232°C (450°F). The pump speed is 3600 rpm.

A laboratory investigation revealed that peeling-type cracks developed in the keyway of the shaft (Fig. 44). The fracture surface had undergone considerable battering when the separation occurred. The keyway fillet has a radius of 0.025 cm (∿0.01 in.). For shafts with a diameter of <16.51 cm (<6.5 in.), the recommended radius should be r/d = 1/48, where r is the radius of the fillet, and d is the shaft diameter.[16] For a 3.17-cm (1.25-in.) diameter shaft, r should be ≈0.051 cm (0.03 in.). The fillet radius presented a stress riser at the keyway, which increased the probability that a fatigue fracture would occur. It was recommended that the fillet radius of the keyway be kept within recommended specifications.

It is suspected by the screwcap manufacturer that the screwcaps failed because of improper heat treatment, but this hypothesis has not been verified to date.

Optical metallography and scanning-electron microscopy will be carried out to verify the failure mode and to complete the analysis.

3. Battelle Char-Burner Thermowells

Two thermocouple protection tubes, Type 446 stainless steel, that were installed in the fluidized bed above the distributor in the agglomerating burner section of the gasifier were severely degraded. The end of one of the tubes was cracked. A macrophotograph of both tubes is shown in Fig. 45. The tubes are 1.9 cm (0.75 in.) in diameter at the thermocouple end and taper to 2.5 cm (1.0 in.) in approximately 50.8 cm (20 in.).

The operating time was ∿1.4 Ms (400 h), 0.9 Ms (∿250 h) of which was below 538°C (1000°F). A "Mulcoa 70" calcined bauxite material was used as the starter bed, and Rosebud coal has been burned for 0.54 Ms (∿150 h). Plant personnel estimated that the thermocouple degradation occurred when the bed was run at temperatures of 1232°C (2250°F) and possibly 1260°C (2300°F).

Optical metallography and scanning-electron microscopy suggested that excessively high temperatures, clinker-type material deposition, and corrosion of the base metal led to the failure. Erosion apparently did not contribute to the failure.

Electron-microprobe analysis showed that Al, O, Si, Mg, S, and Ca were present at the OD of the hot zone, and a depletion of Cr and Fe was also observed. These elements are also contained in the by-product of the burnt coal (clinker), and it is possible that clinker-type products were in contact with the OD of the thermowell. The grain size in the hot zone was twice that in the regions away from the hot zone. These data imply that temperatures in the range 600-1000°C (1110-1830°F) were reached. An exothermic reaction beneath the clinker-type material would increase the temperature and promote grain growth.

It was recommended that temperatures in the fluidized bed be kept below 1150°C (2100°F) to avoid excessive degradation of the mechanical properties of the thermowell. The operating conditions are at the upper limit of the materials performance.

4. Pit Formation on the Synthane Thermowells

Pits were found at the OD of a Hastelloy C-276 thermowell that is located above the distributor cone in the Synthane gasifier. A macrophotograph of the pits is shown in Fig. 46. The thermowell has a welded endcap and pits and grooves were observed in the weld region. A chemical analysis of the corrosion product showed that Al, K, Ca, Mg, Na, and Si were present. These data verified plant personnel suspicions that clinker was in contact with the OD of the thermowell.

It was also found that the endcap had different chemical etching properties than the Hastelloy C-276 tube. It is surmised that the endcap is not Hastelloy C-276. This fact may account for the severe pitting in the weld region of the endcap. It was recommended that the endcap be made of the same material as the tube in the replacement procedure.

The thermowell was recapped with a Hastelloy C-276 cap and is now ∿51 cm (∿20-in.) shorter in length than originally, which should decrease the possibility of clinker deposition.

5. BB-1 Purge Piping from the Synthane Gasifier

Pits were discovered in an Incoloy 800 purge pipe from the Synthane gasifier. The piping is 2.1 cm (0.84 in.) in diameter and carries steam at <427°C (<800°F). A schematic of the pipe, with the exposure times indicated, is shown in Fig. 47. The temperature above the coupling is 427-649°C (800-1200°F) and 649-815°C (1200-1500°F) below the coupling.

A chemical analysis of the pipe showed that the material was within the manufacturer's specifications for Incoloy 800.

An optical macrograph of the pits is shown in Fig. 48. The pits are circular and some agglomeration has occurred. They appear similar to the clinker-related pits observed on the Hastelloy C-276 thermocouple protection tube. The cause for the pitting has not been determined, but the analysis will proceed in the coming quarter to resolve this issue.

6. Synthane Gasifier Nozzle Failures

A leaking crack was discovered in an Incoloy 800 reducer nozzle located on the Synthane gasifier. This nozzle is one of approximately 30 that are welded to the gasifier vessel. As a result of this failure, a visit was made to the Synthane plant to consult with plant personnel on diagnostics of the failure and remedial action that could be taken and to ERDA headquarters in Washington D.C. to plan the strategy for replacement of the nozzles.

A metallurgical examination of the cracked nozzle, carried out by Combustion Engineering, indicated that all the nozzles were sensitized to some degree. It was decided to replace the Incoloy 800 nozzles with low-carbon steel nozzles lined with Monel.

Additional metallographic investigations, nondestructive examination, and sensitization testing will be conducted at ANL in the coming quarter on one or more of the removed nozzles.

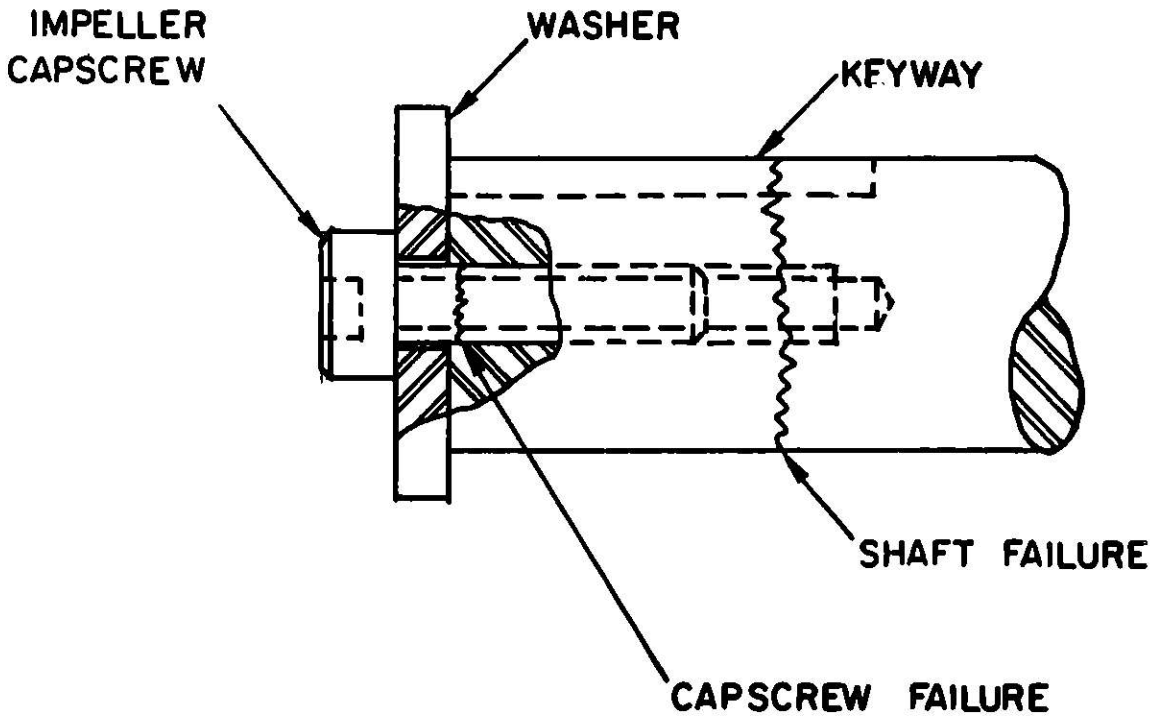

Fig. 43. Schematic of the Pump Shaft and Capscrew for the Venturi Scrubber Recycle Water Pump GA-207 from the Synthane Plant. ANL Neg. No. 306-77-406.

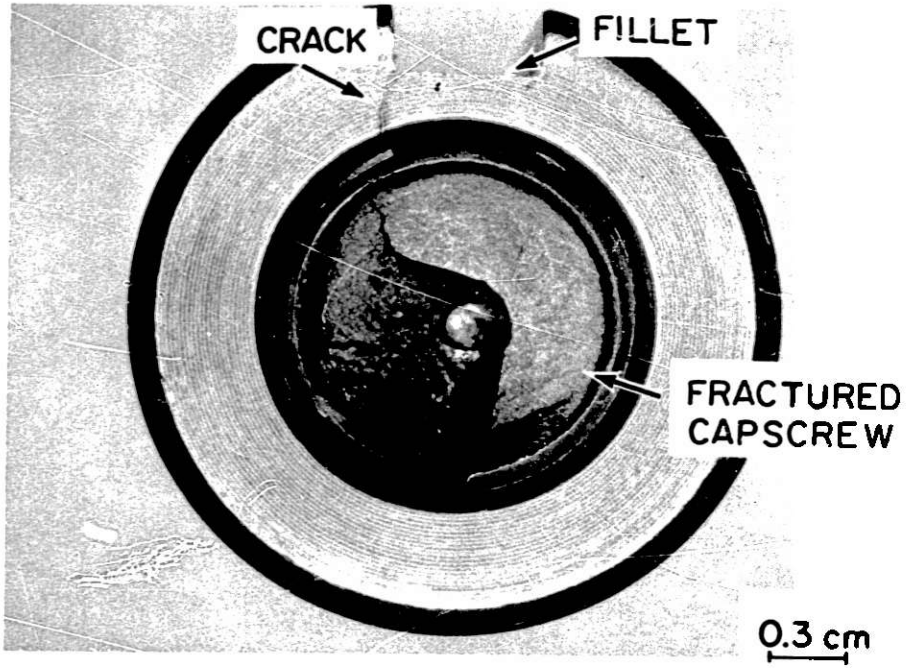

Fig. 44. Cross Section of Synthane Pump Impeller Shaft Showing the Keyway Fillet Radius, Crack, and Fractured Capscrew. ANL Neg. No. 306-77-402.

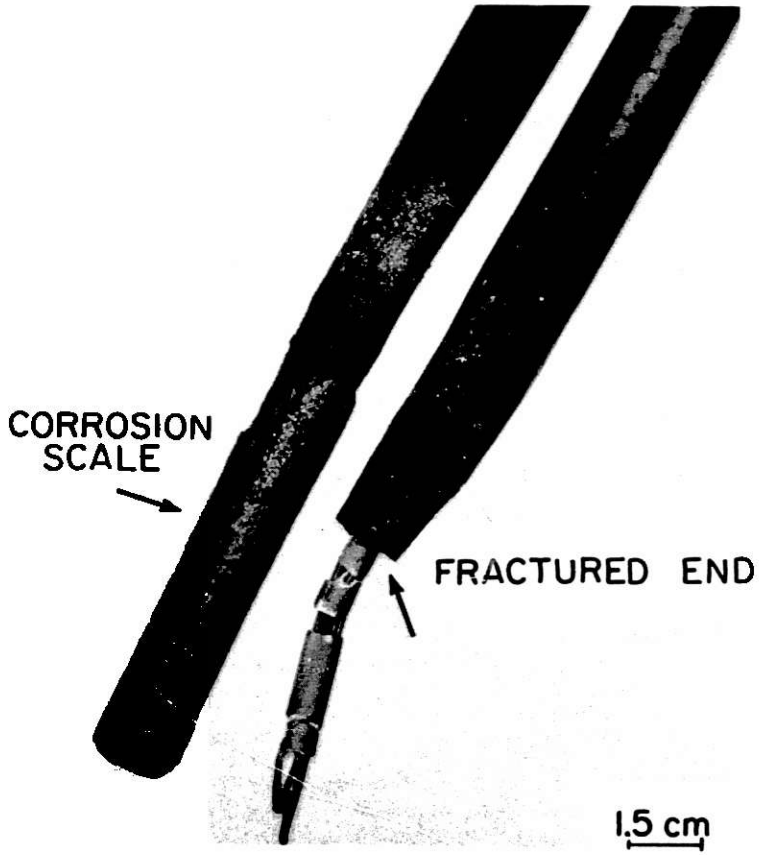

Fig. 45. Battelle Char-Burner Thermocouple Protection Tubes Showing Corrosion Scale and Fracture. ANL Neg. No. 306-77-404.

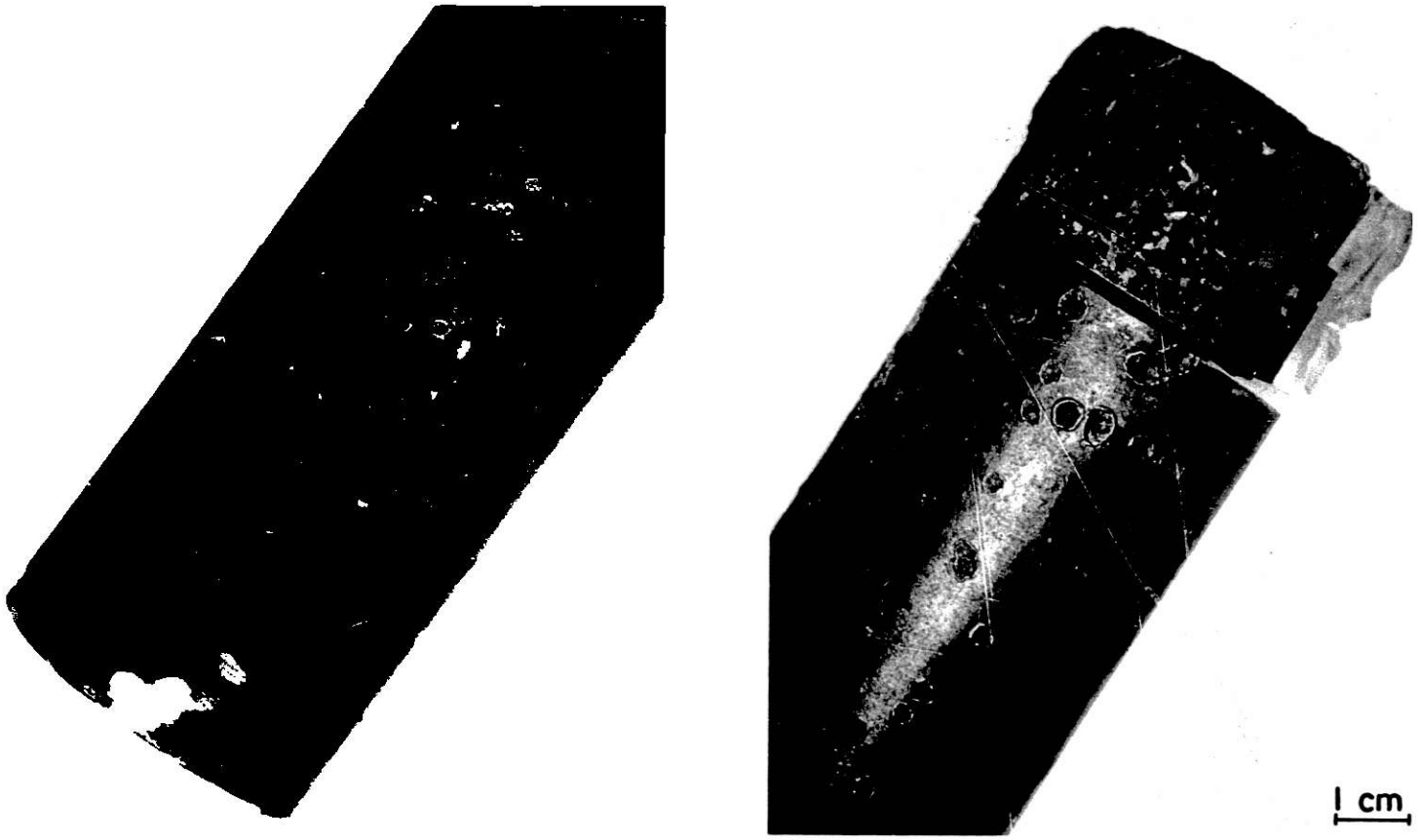

(a) (b)

Fig. 46. Pits at the OD of the Synthane Thermowell. ANL Neg. No. 306-77-405.

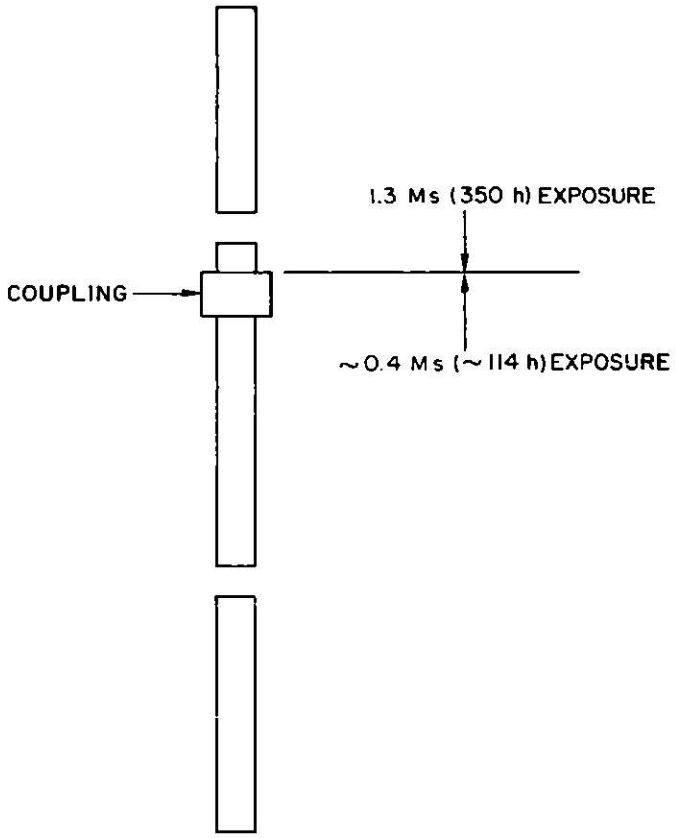

Fig. 47. Schematic of Three Sections of BB-1 Purge Piping from the Synthane Gasifier, with Exposure Times Indicated. ANL Neg. No. 306-77-412.

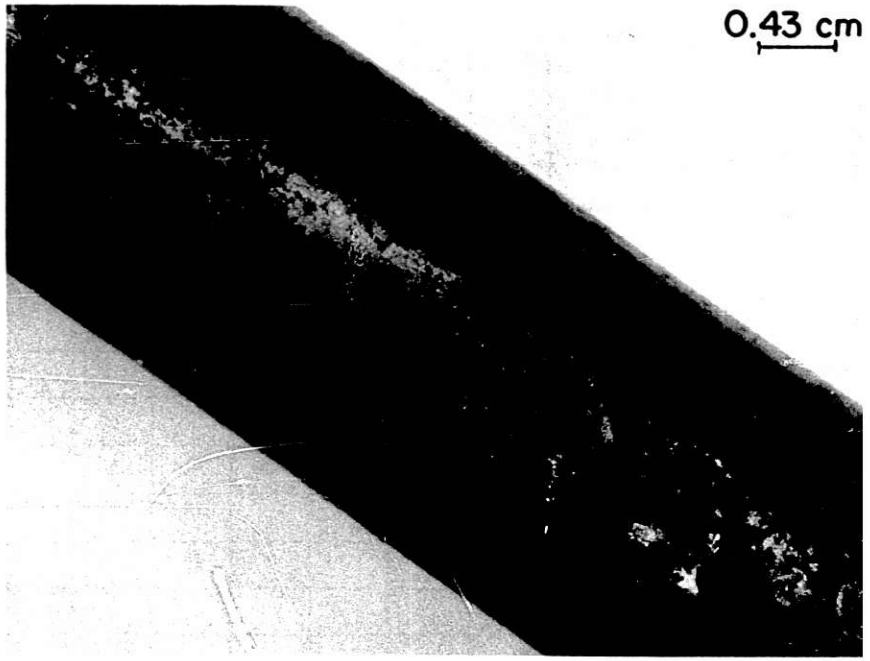

Fig. 48. Optical Macrograph of Pits at the OD of the BB-1 Purge Line from the Synthane Gasifier. ANL Neg. No. 306-77-403.

MILESTONE CHART

FY 1977

Task F -- Component Performance and Failure Analysis

a. Failure analysis

b. Component performance (coupons)

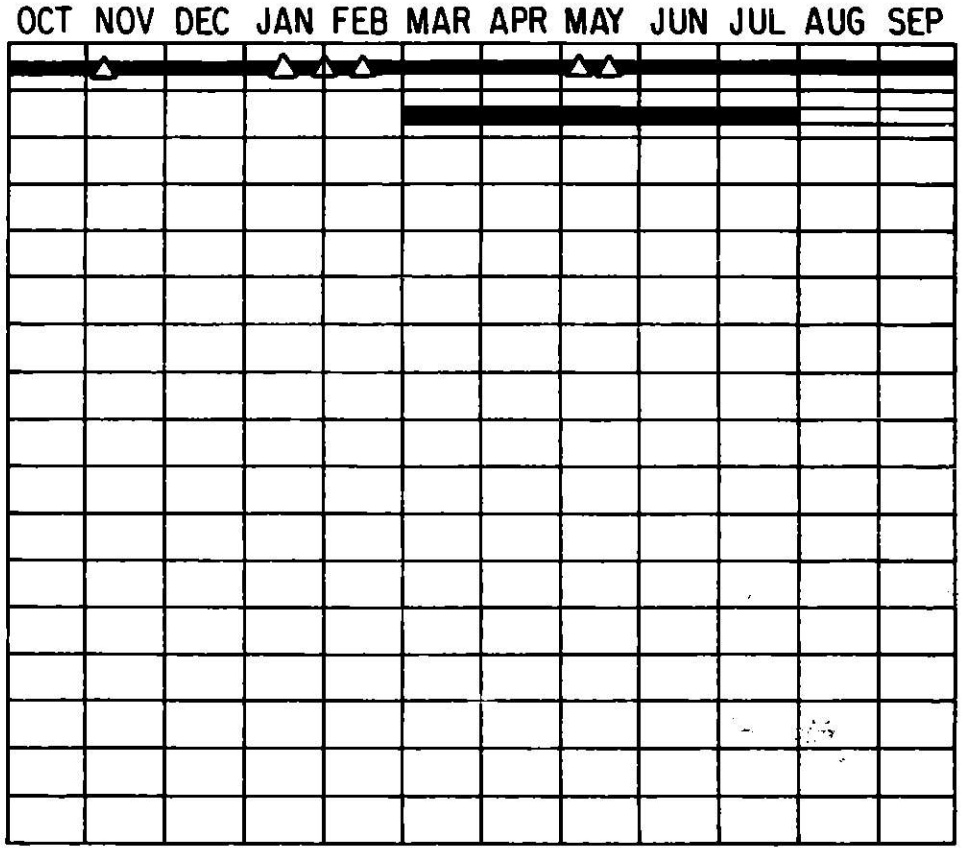

Failure Analysis Report Issued △

Scheduled ═══

Progress ▬▬

Scheduled Extension ////////

REFERENCES

1. Materials Science Division Coal Technology Fifth Quarterly Report, October-December, 1975, Argonne National Laboratory, ANL-76-22.

2. Materials Science Division Coal Technology Sixth Quarterly Report, January-March, 1976, Argonne National Laboratory, ANL-76-60.

3. Materials Science Division Coal Technology Seventh Quarterly Report, April-June, 1976, Argonne National Laboratory, ANL-76-111.

4. Materials Science Division Coal Technology Eighth Quarterly Report, July-September, 1976, Argonne National Laboratory, ANL-76-125.

5. Materials Science Division Coal Technology Ninth Quarterly Report, October-December, 1976, Argonne National Laboratory, ANL-77-5.

6. Materials Science Division Coal Technology Tenth Quarterly Report, January-March, 1977, Argonne National Laboratory, ANL-77-41.

7. M. S. Crowley and R. C. Johnson, "Guidelines for Installing and Drying Refractory Concrete Linings in Petroleum and Petrochemical Units," Amer. Ceram. Bull., 51, No. 3, 226-230 (1972).

8. G. V. Givan, et al., "Curing and Firing High Purity Calcium Aluminate-Bonded Tabular Alumina Castables," Am. Ceram. Bull., 54(8), 710-713 (1975).

9. D. Hums and P. Jax, "Determination of Incipient Crack Formation in Ceramic Materials Under Thermal Stress by the Sonic Emission Method," Science of Ceramics, 7, 279-295 (1973).

10. G. C. Robinson, C. R. Reese and E. A. La Roche, Jr., "Determination of Thermally Induced Acoustic Emissions of Ceramics," Am. Ceram. Bull., 53, 483-485 and 488 (1974).

11. J. S. Mazaryk and R. E. Farris, "High Purity Refractory Concrete: Behavior During Manufacture of Massive Shapes," Am. Ceram. Bull., 55, 996-998 (1976).

12. O. K. Chopra and K. Natesan, "Thermodynamic Equilibria of Multicomponent Gas Mixtures," Argonne National Laboratory, to be published.

13. K. Natesan, in "MFPG Conference on Prevention of Failures in Coal-conversion Systems," Eds. T. R. Shives and W. A. Willard, U. S. Department of Commerce, NBS Special Publication 468, April 1977, pp. 159-171.

14. A. J. MacNab, in Workshop on Materials Problem and Research Opportunities in Coal Conversion, Vol. II, p. 33, Ohio State University, Columbus, Ohio, 1974, p. 33.

15. "Evaluations of the Elevated Temperature Tensile and Creep-rupture Properties of C-Mo, Mn-Mo and Mn-Mo-Ni Steels," Prepared for the Metals Properties Council by G. V. Smith, ASTM Publication DS47 (1971).

16. R. E. Peterson, Stress Concentration Factors (John Wiley Publ. Co., 1974) p. 245.